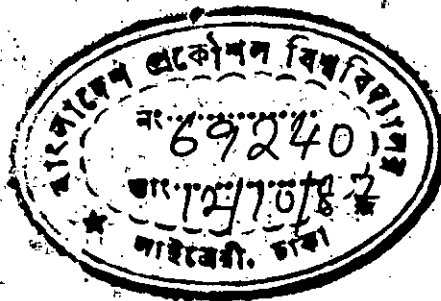


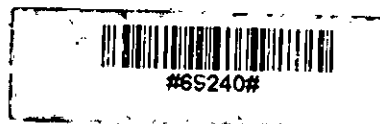
PERFORMANCE AND DESIGN OPTIMIZATION OF A
VERTICAL-AXIS STRAIGHT-BLADED DARRIEUS WIND TURBINE

BY

NIKHIL RANJAN DHAR.
B.Sc. ENGG. (MECH.)



A THESIS PRESENTED TO THE DEPARTMENT OF MECHANICAL ENGINEERING
IN PARTIAL FULFILLMENT OF THE REQUIREMENT FOR THE DEGREE OF
M.Sc. ENGG. (MECH.)



BANGLADESH UNIVERSITY OF ENGINEERING AND TECHNOLOGY, DHAKA

SEPTEMBER, 1987

THIS IS CERTIFIED THAT THIS WORK WAS DONE BY ME AND
THAT IT HAS NOT BEEN SUBMITTED ANYWHERE FOR AWARD OF
ANY DEGREE OR DIPLOMA OR FOR PUBLICATION.

C. D. ...

SIGNATURE OF THE SUPERVISOR

Nimil Rajan Dm

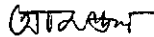
SIGNATURE OF THE CANDIDATE

PERFORMANCE AND DESIGN OPTIMIZATION OF A
VERTICAL-AXIS STRAIGHT-BLADED DARRIEUS WIND TURBINE

BY

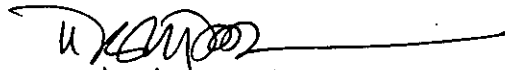
NIKHIL RANJAN DHAR

Approved as to the style and content:



DR. AMALESH CHANDRA MANDAL
Associate Professor
Mech. Engg. Dept., BUET, Dhaka.

CHAIRMAN



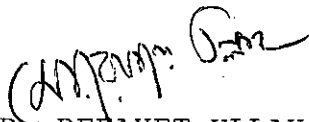
DR. DIRAK KANTI DAS
Professor & Head
Mech. Engg. Dept., BUET, Dhaka.

MEMBER



DR. MD. QUAMRUL ISLAM
Associate Professor
Mech. Engg. Dept., BUET, Dhaka.

MEMBER



DR. MD. REFAYET ULLAH
Assistant Professor
Naval Architecture & Marine Engg. Dept.
BUET, Dhaka.

MEMBER
(External)

ACKNOWLEDGEMENT

I would like to express my sincerest gratitude to Dr. Amallesh Chandra Mandal, Associate Professor, Mechanical Engineering Department, Bangladesh University of Engineering and Technology, Dhaka for his invaluable suggestions, careful supervision and constant inspiration throughout whole of my working period on my project. I am also indebted to him for providing me with necessary informations regarding my research, otherwise, this work could not be carried out properly.

I am very much grateful to Dr. Dipak Kanti Das, Professor and Head, Mechanical Engineering Department, BUET, Dhaka for his valuable suggestions and advice. Also I would like to acknowledge my profound appreciation for the trouble he has taken while reading the manuscript.

I would like to acknowledge the valuable suggestions given by Dr. Md. Quamrul Islam, Associate Professor, Mechanical Engineering Department, BUET, Dhaka and Dr. Md. Refayet Ullah, Assistant Professor, Naval Architecture and Marine Engineering Department, BUET, Dhaka.

I am thankful to the staff of the Computer Centre for their co-operation, especially to Dr. J.R. Choudhury, Director, Computer Centre, BUET, Dhaka for his sincere assistance during running programme and to Mr. Dulal Chandra Kar, Programmer, Computer Centre, BUET, Dhaka for some discussions with him and for his sincere help.

ABSTRACT

A theoretical investigation of aerodynamic performance and design is carried out for vertical-axis straight-bladed Darrieus wind turbines. Aerodynamic performance is performed with blades of cambered cross-section while design is conducted with blades of symmetric cross-section. For the aerodynamic analysis multiple streamtube theory and cascade theory are applied. In order to choose the lift and drag coefficients for the cambered blade profile, concept of thin airfoil theory has been applied.

A cascade principle (Similar to that used in turbomachines) with blades of cambered cross-section is applied for the performance prediction of a vertical-axis straight-bladed Darrieus wind turbine. By using the blades of cambered cross-section, the lift force increases in the upwind side and decreases in the downwind side in comparison to those for a turbine with symmetric blade cross-section. As a result higher power is produced in upwind side and lower power is produced in downwind side for a turbine with cambered blade cross-section in comparison to those for turbine with symmetric blade cross-section. However the net power production is positive thereby making the higher efficiency. The calculated results of cambered blade cross-section are compared with those of symmetric blade cross-section.

A design of a straight-bladed Darrieus wind turbine with blades of symmetric cross-section is performed. The design is done at variable turbine speed condition. In order to mini-

mize the blade stress and with a view to use the low cost material for blade manufacture the blade support type is considered to be overhanged type. It is observed from the design analysis that this design with overhanged support reduces the blade stress remarkably.

To My Parents

CONTENTS

	<u>Page</u>
ACKNOWLEDGEMENT	iv
ABSTRACT	v
CONTENTS	viii
LIST OF FIGURES	x
LIST OF SYMBOLS	xv
<u>CHAPTER 1 : INTRODUCTION</u>	1
1.1 Renewal Interest in Wind Power	1
1.2 Role of Aerodynamics in Wind Power	3
1.3 Aim of the <u>present</u> work	4
1.4 Scope of the Thesis	5
<u>CHAPTER 2 : LITERATURE SURVEY</u>	7
2.1 Historical Background	7
2.2 Existing Prediction Methods	10
<u>CHAPTER 3 : AERODYNAMIC THEORIES OF TURBINE</u>	16
3.1 Single Streamtube Theory	16
3.1.1 Drag Force Along Streamtube	16
3.1.2 Blade Element Angles and Velocities	18
3.1.3 Aerodynamic Forces	19
3.1.4 Velocity Ratio and Power Coefficient	20
3.2 Multiple Streamtube Theory (Wilson's Approach)	21
3.2.1 Basic Assumptions	22
3.2.2 Axial Momentum Theory	22
3.2.3 Blade Element Force Along Streamtube	25

	<u>Page</u>
3.2.4 Induced Velocity Ratio, Aerodynamic Forces and Power Coefficient	28
3.3 Vortex Theory	32
3.4 Cascade Theory	34
3.4.1 Basic Assumptions	35
3.4.2 Blade Element Angles and Velocities	36
3.4.3 Aerodynamic Forces	39
3.4.4 Velocity Contributed by Circulation and Total Power Loss Term	41
3.4.5 Velocity Ratios and Rotor Power Coefficient	44
3.4.6 Blade Pitching	48
<u>CHAPTER 4 : RESULTS AND DISCUSSIONS</u>	50
4.1 Calculated Results	50
4.2 Comparative Results	57
<u>CHAPTER 5 : DESIGN OF TURBINE</u>	64
<u>CHAPTER 6 : CONCLUSIONS AND RECOMMENDATIONS</u>	73
6.1 Conclusions	73
6.2 Recommendations for Further Researches	76
<u>REFERENCES</u>	78
<u>FIGURES</u>	85
<u>APPENDICES</u>	131
Appendix-A Flow Diagram of Computational Methods	131
Appendix-B Derivation of Moment of Inertia of Blade Airfoil Section	136
Appendix-C Derivation of Bending Moment and Bending Stress	141
Appendix-D Airfoil Characteristics	143
Appendix-E Effect of Aspect Ratio	145

LIST OF FIGURES

<u>Figures</u>	<u>Page</u>
2.1 Persian windmill of vertical axis type	86
2.2 Horizontal-axis wind turbine for pumping water	86
2.3 Restored Danish Gedser wind turbine	87
2.4 Savonius rotor	87
2.5 Vertical-axis curved-bladed Darrieus wind turbine	88
2.6 Vertical-axis straight-bladed Darrieus wind turbine	89
3.1 Streamtube consisting of the rotor showing the axial flow velocities	90
3.2 Aerodynamic forces on a blade element of a Darrieus rotor	90
3.3 Velocity diagram on the blade element of straight bladed Darrieus wind turbine	91
3.4 Aerodynamic forces acting on an airfoil	91
3.5 Cross-sectional area of an elemental streamtube of a straight-bladed Darrieus wind turbine	92
3.6 Pressures and velocities along the streamtube	93
3.7 Velocity diagram on the blade element of a straight-bladed Darrieus wind turbine	93
3.8 Force diagram on the blade element of a straight-bladed Darrieus wind turbine	94
3.9 Elemental blade forces of a straight-bladed Darrieus wind turbine	94
3.10 Vortex system for a single blade element	95
3.11 Velocity induced at a point by a vortex filament	95
3.12 Horizontal section of a straight-bladed (cambered blade cross-section) Darrieus wind turbine with flow velocities	96
3.13 Relative flow velocities on a cambered-blade airfoil	96
3.14 Development of blades into cascade configuration	97
3.15 Velocity diagram on the blade section	98

<u>Figures</u>	<u>Page</u>	
3.16	Force diagram on the blade section	98
3.17	Velocities and forces on blade airfoil with pitching in cascade configuration	99
4.1	Overall power coefficients Vs. tip speed ratios at various solidities (calculated by cascade theory)	100
4.2	Overall torque coefficients Vs. tip speed ratios at various solidities (calculated by cascade theory)	100
4.3	Overall drag coefficients Vs. tip speed ratios at various solidities (calculated by cascade theory)	101
4.4	Overall power coefficients Vs. tip speed ratios at different fixed blade pitchings (calculated by cascade theory)	101
4.5	Overall power coefficients Vs. tip speed ratios at different amplitudes of sinusoidal pitch variation (calculated by cascade theory)	102
4.6	Overall power coefficients Vs. tip speed ratios at different combined pitch (fixed + sinusoidal) variation (calculated by cascade theory)	102
4.7	Variations of instantaneous torques with azimuth for various no. of blades (calculated by cascade theory)	103
4.8	Comparisons of overall power coefficients at various solidities (calculated by cascade theory)	104
4.9	Comparisons of overall torque coefficients at various solidities (calculated by cascade theory).	104
4.10	Comparisons of overall drag coefficients at various solidities (calculated by cascade theory).	105
4.11	Comparisons of overall power coefficients with tip speed ratios at different fixed blade pitchings (calculated by cascade theory).	105
4.12	Comparisons of overall power coefficients with tip speed ratios at different amplitudes of sinusoidal pitch variation (calculated by cascade theory).	106

<u>Figures</u>	<u>Page</u>	
4.13	Comparison of overall power coefficients with tip speed ratios at different (fixed + amplitudes of sinusoidal) pitch variation (calculated by cascade theory).	106
4.14	Comparisons of induced velocity ratios by various analytical methods.	107
4.15	Comparison of local angles of attack by various analytical methods.	107
4.16	Comparisons of local Reynolds number by various analytical methods.	108
4.17	Comparisons of local non-dimensional tangential forces by various analytical methods.	108
4.18	Comparisons of local non-dimensional normal forces by various analytical methods.	109
4.19	Comparisons of induced velocities with azimuth at different tip speed ratios (calculated by cascade theory).	109
4.20	Comparisons of local angles of attack with azimuth at different tip speed ratios (calculated by cascade theory).	110
4.21	Comparisons of local Reynolds number with azimuth at different <u>tip speed ratios</u> (calculated by cascade theory).	110
4.22	Comparisons of local non-dimenssional tangential forces with azimuth at different tip speed ratios (calculated by cascade theory).	111
4.23	Comparisons of local non-dimenssional normal forces with azimuth at different tip speed ratios (calculated by cascade theory).	111
5.1	Design configurations of variable speed turbines at various solidities (calculated by cascade theory)	112
5.2	Comparisons of design configurations of variable speed turbines at various solidities (calculated by cascade theory).	113

<u>Figures</u>	<u>Page</u>	
5.3	Comparisons of design configurations of variable speed turbines at various solidities (calculated by cascade theory).	114
5.4	Comparisons of total blade length (L_B) at various solidities (calculated by cascade theory).	115
5.5	Variations of overall power coefficients with tip speed ratios at different wind speeds (calculated by cascade theory).	116
5.6	Variations of overall torques with rpm at various wind speeds (calculated by cascade theory).	116
5.7	Variations of overall power with rpm at various wind speeds (calculated by cascade theory).	117
5.8	Variations of blade mass and maximum blade stress with blade skin thickness (calculated by cascade theory).	117
5.9	Variations of normal, centrifugal and net normal forces with azimuth angle (calculated by cascade theory).	118
5.10	Variations of bending moments due to net normal forces with azimuth angle (calculated by cascade theory).	119
5.11	Variations of bending moments due to tangential forces with azimuth angle (calculated by cascade theory).	119
5.12	Variations of bending stresses due to net normal forces with azimuth angle (calculated by cascade theory).	120
5.13	Variations of bending stresses due to tangential forces with azimuth angle (calculated by cascade theory).	120
5.14	Variations of starting torques with blade pitchings.	121
5.15	Variation of starting torque with wind speed.	121

<u>Figures</u>	<u>Page</u>	
5.16	Variation of blade mass with blade skin thickness (calculated by cascade theory) (Ref. [25])	122
5.17	Variation of centroidal area moment of inertia about \bar{x} -axis with blade skin thickness (calculated by cascade theory). (Ref. [25])	122
5.18	Variation of centroidal area moment of inertia about \bar{y} -axis with blade skin thickness (calculated by cascade theory) (Ref. [25])	123
B.1	Blade airfoil cross-section.	124
B.2	Geometry of inner and outer faces of blade airfoil.	124
B.3	Geometry on blade airfoil cross-section to find skin area.	125
B.4	Geometry to obtain rib area.	125
B.5	Geometry to determine centroid and moment of inertia.	126
C.1	Schematic Diagram of Vertical-axis straight-bladed Darrieus turbine .	127
C.2	Horizontal section of a straight-bladed wind turbine showing forces on the turbine blade.	128
C.3	Bending moment diagram of a overhanged support beam.	128
D.1	Variation of lift coefficient with angle of attack at a fixed Reynolds number of 3000000 for the airfoil NACA 1412.	129
D.2	Variation of drag coefficient with angle of attack at a fixed Reynolds number of 3000000 for the airfoil NACA 1412.	129
D.3	Variation of lift coefficient with angle of attack at a fixed Reynolds number of 3000000 for the airfoil NACA 1415.	130
D.4	Variation of drag coefficient with angle of attack at a fixed Reynolds number of 3000000 for the airfoil NACA 1415.	130

LIST OF SYMBOLS

A	projected frontal area of turbine
A_b	total blade sectional area
A_r	area of blade rib
A_s	area of blade skin
AR	aspect ratio = H/C
C	blade chord
c.	chord of blade within elemental $\delta\theta$
C_d	blade drag coefficient
C_{di}	induced drag coefficient
C_{do}	zero-lift drag coefficient/section drag coefficient for infinite aspect ratio
C_D	turbine overall drag coefficient = $F_D / \frac{1}{2} \rho A V_\infty^2$
C_{DD}	rotor drag coefficient = $F_D / \frac{1}{2} \rho A V_a^2$
C_l	blade lift coefficient
C_m	blade pitching moment coefficient
C_n	normal force coefficient
C_P	turbine overall power coefficient = $P_o / \frac{1}{2} \rho A V_\infty^3$
C_Q	turbine overall torque coefficient = $Q / \frac{1}{2} \rho A V_\infty^2 R$
C_t	tangential force coefficient
D	blade drag force
\vec{e}_c	unit vector along chordal direction
F	force on blade airfoil
f	maximum camber
F_{cf}	centrifugal force
F_D	turbine drag in streamwise direction
F_n	normal force (in radial direction)

F_{net}	net normal force (in radial direction)
F_n^+	non-dimensional normal force = $C_n (W/V_\infty)^2$
F_t	tangential force
F_t^+	non-dimensional tangential force = $C_t (W/V_\infty)^2$
g	acceleration due to gravity
h_d	rotor height diameter ratio = H/D
H	height of turbine
$\vec{i} \vec{j} \vec{k}$	unit vectors, each is normal to the plane of the others
I	area moment of inertia
\bar{I}	centroidal area moment of inertia
I_r	moment of inertia of blade rib
I_s	moment of inertia of blade skin
k	factor to include real lift value
k_i	exponent in the induced velocity relation
l	length of vortex filament
L	blade lift force
L_B	total blade length
\dot{m}	mass flow rate
m_b	blade mass per unit length
M	blade pitching moment
M_{bn}	bending moment due to net normal force in N-m
M_{bt}	bending moment due to tangential force in N-m
N	number of blades
P	static pressure
P_o	overall power
P_∞	atmospheric pressure
q	dynamic pressure = $\frac{1}{2} \rho W^2$
Q	overall torque

Q_l	local torque
Q_s	starting torque
\vec{r}	unit vector
rpm	turbine speed in revolution per minute
R	turbine radius
R_e	local Reynolds number = WC/ν
R_{er}	reference Reynolds number
R_{et}	turbine speed Reynolds number = $R\omega C/\nu$
R_{ew}	wind speed Reynolds number = $V_\infty C/\nu$
S_a	<u>allowable</u> stress in Newton/sq.mm
S_{bn}	bending stress due to net normal force in Newton/sq.mm
S_{bt}	bending stress due to tangential force in Newton/sq.mm
S_m	maximum value of blade stress in each revolution N/sq.mm
t	blade spacing = $2\pi R/N$
t_c	maximum blade thickness as a fraction of chord
t_s	blade skin thickness
V	local velocity
V_a	induced velocity
V_{av}	average induced velocity
V_c	chordal velocity component
V_{cut}	cutout speed
V_e	wake velocity in upstream side
V_n	normal velocity component
V_p	induced velocity at a point p
V_w	wake velocity in downstream side
V_Γ	velocity contributed by circulation
V_∞	wind velocity
W	relative flow velocity

α	angle of attack/angle of attack for finite wing
α_{cor}	corrected angle of attack due to camberness effect
α_i	induced angle of attack
α_l	local angle of attack
α_{mod}	modified angle of attack
α_o	angle of attack for infinite wing
β	angle between relative flow velocity direction and tangent to blade flight path at blade fixing point
γ	blade pitch angle
Γ	circulation per unit length
Γ_B	bound vortex
ΔP_{ov}	total pressure loss term (total cascade loss)
ϵ	D/L
θ	azimuth angle
λ	tip speed ratio = $R\omega/V_\infty$
ν	kinematic viscosity
ρ	fluid density
ρ_b	density of blade material
σ	solidity = NC/R
T	correction factor for induced angle
ϕ_p	angle between chordal and freestream velocity direction
ω	angular velocity of turbine in rad/sec

SUBSCRIPTS

d	downstream side/design point
m	maximum value
u	upstream side
x	x-axis
y	y-axis
1	cascade inlet
2	cascade outlet

CHAPTER 1 : INTRODUCTION

Interest in wind machines recently has resulted in the re-invention and analysis of the wind power machines developed in the past. People are extracting energy from the wind in various ways for the past few centuries. One means for converting wind energy to a more useful form may be done by applying the wind mills. Recently this science is gaining more popularity due to the fuel crisis. There are various types of windmills. The most common one having the blades of airfoil shape is the horizontal-axis turbine and another type is the vertical-axis Darrieus wind turbine. The main advantage of the vertical-axis wind turbine is the simplicity of its manufacture compared to the horizontal-axis wind turbine. The present work consists of the performance analysis of a vertical-axis Darrieus wind turbine. The work also include the design of the similar type of turbine.

1.1 Renewal Interest in Wind Power.

Study of wind energy is of prime importance concerning present wind energy crisis all over the world. Conventional energy source are no longer sufficient to cover the increasing demand of energy throughout the world. For a long time people are extracting energy from the fossil fuels in almost all the countries. With the rising demand of energy and for many other reasons, prices of these fuels are increasing day by day. So people are trying to find the alternate sources of energy to exploit them at the cheapest rate. Wind energy is a kind of

energy source which will never be finished.

Since the last decade increasing and widespread interest has been taken in the potentialities of the wind as a source of energy. In several countries both private and Government sponsored organizations have been established to investigate the way of extracting energy from the wind. Some of the reasons for this interest are given as follows.

i) The rapidly increasing demand for electrical energy accompanied by the inadequacy of fuel supply or of potential hydro-electric resources in some countries;

ii) high and rising costs of power generation in stream-driven stations or in newly-constructed hydro-stations and that for the transmission of the power generated by them, are now often increased by the fact that the more easily developed sources, near to load centres, have already been exploited;

iii) difficult economic and political conditions of the post-war years tending to make countries depend upon their own resources for the generation of power rather than upon imported fuels;

iv) the realization that coal and oil resources are being used up at an increasingly high rate and that they can be put to better use than burning them as fuels;

v) the greatly increased knowledge of aerodynamics as applied to aeroplane construction, resulting from war-time

research and development. This renders the problems to be faced in constructing large windmills less formidable than they were formerly;

vi) the appreciation of the advantages of diversity in the availability of power from different sources connected to a widespread net work;

vii) the Smith-Putnam experimental aerogenerator, of 1250 KW capacity, built during the war on Granpa's Knob in central Vermont U.S.A. Although this machine was not completely successful as an practical possibility of employing large plants to generate electricity from wind power.

1.2 Role of Aerodynamics in Wind Power

The success of wind power as an alternate energy source is obviously a direct function of the economics of production of wind power machines. In this regard, the role of improved power output through the development of better aerodynamic performance offers some potential return: however, the focuss is on the cost of entire system, of which the air-to-mechanical energy is transducer is but one part. The technology and methodology used to develop present day fixed and rotating wind aircraft appears to be adequate to develop wind power.

One of the key areas associated with future development of wind power is rotor dynamics. The interaction of inertial, elastic and aerodynamic forces will have a direct bearing on the

manufacture, life and operation of wind power systems, while at the same time having a minor effect on the power output. Thus, the aerodynamics of performance prediction, quasi-static in nature, is deemed adequately developed while the subject of aeroelasticity remains to be transferred from aircraft applications to wind power applications. Since 1920, there have been numerous attempts in designing feasible WECS (wind energy conversion system) for large scale power generation in accordance with modern theories.

1.3 Aim of the Present Work.

Uptil now, on vertical-axis Darrieus wind turbine both aerodynamic and structural works have been done in many parts of the world. However, little attention has been given on the Darrieus wind turbine with blades of cambered cross-section. In this thesis the aim was to find the detail aerodynamic as well as structural analysis of Darrieus turbine with blades of cambered cross-section. It is expected that this work would contribute greatly to the knowledge of existing research work regarding the vertical axis straight-bladed Darrieus wind turbine.

The present research work is consisted of finding the performance characteristics of a vertical-axis straight-bladed Darrieus wind turbine and making necessary development of this kind of turbine. At high solidity the performance prediction of a vertical-axis Darrieus wind turbine with blades of cambered

cross-section is also done. Blade pitching is also incorporated to find the performance characteristics of a turbine with cambered blade airfoil.

It has also been noted that there is want of extensive research work on design for low as well as high solidity Darrieus wind turbines. A lot of parameters control the performance characteristics of a Darrieus wind turbine. Among them solidity, height-diameter ratio, aspect ratio, tip speed ratio, number of blades, chord-radius ratio, Reynolds number etc. may be mentioned. In the present work, it is aimed to find out an optimum design condition with overhanged beam support to choose the above parameters based on optimum design condition.

The primary object was to carry out the detail aerodynamic and structural analyses. However finally it was not possible to perform all the works. So mostly aerodynamic analysis is conducted and partially stress analysis is done.

1.4 Scope of the Thesis

In this thesis, a theoretical investigation of the aerodynamic performance is presented for the vertical-axis straight-bladed wind turbines with both symmetric and cambered blade cross-sections. In addition, a simplified design is conducted for a vertical-axis straight-bladed Darrieus wind turbine with blades of symmetric cross-section.

Chapter 1 presents the general introduction providing with the brief idea of the work which are performed and described in this thesis. In the chapter 2, the review of the literature is presented. It gives a short description of the related papers which have been published by the different authors in the different place.

In the chapter 3, different aerodynamic theories of vertical axis straight-bladed Darrieus wind turbine are described. The analytical prediction methods which are related to the present thesis are rather described elaborately. Existing cascade theory is remodelled to include the cambered blade cross-section and applied for straight-bladed Darrieus wind turbine.

Chapter 4 presents the calculated results for the vertical axis Darrieus wind turbine with blades of cambered cross-section. The effect of few parameters in the performance characteristics of a vertical-axis Darrieus wind turbine are discussed. Comparisons of the calculated results for the symmetric and cambered blade profiles are given in this chapter.

A design method for vertical-axis straight-bladed Darrieus wind turbine is given in the chapter 5. Design at variable turbine speed condition is performed. Design approach is suggested with a view to make the design optimum.

Finally in the chapter 6, general conclusions are drawn and few recommendations for the future works are presented.

CHAPTER 2 : LITERATURE SURVEY

Uptil now many theories have been developed in different parts of the world for the performance prediction of Darrieus wind turbines. Few of them are described in brief in this chapter. Brief history of the development of modern turbine has also been incorporated into this chapter.

2.1 Historical Background

To extract energy from the wind, people have been working on various classes of wind contrivances from the ancient time. Probably works on windmills have been started from 2000 B.C. The duration from the ancient time upto the end of the 19th century may be categorized as the ancient development period while that from the end of 19th century upto date may be termed as the modern development period.

Historically, wind energy conversion systems can be considered as one of man's truly basic machines. Early documents refer to use of windmills, as depicted in Figure 2.1 in Persia in 644 A.D. called Persian vertical-axis windmill which was used to grind grain. That kind of windmill had been working upto about 12th century, when simultaneously in France and England Dutch type of windmills were made whose purpose were to grind grain and pump water. These windmills were of horizontal-axis types.

At the mid-nineteenth century, more than six-million small multibladed windmills, providing power outputs of less than 1 hp each in an average wind, have been built and used in the United

States to pump water, generate electricity, and perform similar functions. It is estimated that over 150,000 turbines are currently in operation.

Water pumping windmills are used in many parts of the United States, not only for pumping water for farm and rural households, but for watering livestock on ranges in remotes area. These types of machines commonly have metal fan-blades, 12 to 16 feet in diameter, mounted on a horizontal shaft, with a tail-vane to keep rotor facing is to the wind (Figure 2.2). A 12- foot diameter rotor of this type develops about $2/3$ hp in a 15 mph wind and can pump about 10 gallons of water per minute to a height of about 100 feet.

Small wind machines, used to generate electricity, usually have two or three propeller-type blades that are connected by a shaft and gear train to a d.c. generator. They usually incorporate some type of energy storage system, often consisting of a bank of batteries. One of the classic designs of this type is the Jacobs Wind Electric Company unit with a three-blades propeller, 14 feet in swept diameter, which deliver about 1 KW in a wind of 14 mph.

At the end of 19th century, the first modern windmill of horizontal-axis type with multi-blade was built in Denmark to produce electricity. It was the beginning of the modern development period. Starting from that time people in different countries especially in rural America have been constructing a large number of multibladed wind turbines for pumping water and generating

electricity. Afterwards as a consequence of development works for several years, two or three bladed propeller type of windmills with airfoil shape blades were built in near about 1925. In Denmark, the 200 KW Gedser mill (Figure 2.3), which was the latest, was operated until 1968, when it was shut down because it was found that by that time the cost of electricity supplied by this wind-powered unit was about twice the equivalent fuel cost of the steam-powered electric utility plants that were being operated in Denmark. After the energy crunch of 1973, the 200 KW Gedser mill was refurbished, and in 1977 it was put back into service, using funding partly supplied by the United States Department of Energy.

In 1931, 100 KW Russian horizontal-axis wind turbine was constructed while in 1934, the large 1250 KW Smith-Putnam horizontal-axis wind turbine was built in the United State.

Modern development period have really begun with the development of horizontal-axis wind turbines. In 1924 Finnish Engineer S.J. Savonius constructed the first savonius rotor of vertical-axis type (Figure 2.4) and he conceived the idea from the Flettner's Rotor. In 1925 G.J.M. Darrieus of France, Proposed for United States patent a new type of wind turbine designed for the generation of power. The patent issued in 1931 as number 1,835,018 was for a "turbine having its rotating shaft transverse to the flow of the current". The Straight-bladed configuration was also covered in the original Darrieus pattern. This kind of wind machine is called Darrieus wind turbine (Figures 2.5 and 2.6) after the name of G.J.M. Darrieus.

Since the beginning of the twentieth century, researchers in the various parts of the world had been giving much effort in the development works of the wind turbines but from about the middle of this century, it began to lose its momentum for further development. In about 1970's people took renewed interest in this field. Especially in 1973 with oil embargo, people were thinking regarding the alternate sources of energy. As a result in many developed and underdeveloped countries a lot of new projects concerning the development of wind turbines have been taken.

Only during the last decade in the different countries enormous attention has been paid in the field of performance prediction method applicable to wind turbines. As an outcome, a number of analytical prediction methods have been developed. Works have also been extended to both the static and dynamic analyses of wind turbines. Different types of design methods have been worked out in many places.

2.2 Existing Prediction Methods

The main purpose of a wind turbine is to extract energy from the air flow and then convert it into mechanical energy which later may be transformed into other forms of energy. The performance calculation of wind turbines are mostly based upon a steady flow, in which the influence of the turbulence of the atmospheric boundary layer is neglected.

For the design and evaluation of wind turbines the availability of computational tools is essential. Most existing theoretical models are based on the momentum theory, cascade theory and vortex theory.

For the calculation of the performance characteristics of a straight-bladed Darrieus wind turbine the most simple prediction method is the single streamtube model. It has been introduced first by Templin [42] in 1974. In this model the whole turbine is assumed to be enclosed within the single streamtube. Dr. Templin first incorporated the concept of wind-mill actuator disc theories into the analytical model of a Darrieus wind turbine. In the actuator disc theory the induced velocity (rotor axial flow velocity) is assumed to be constant throughout the disc and is obtained by equating the streamwise drag with the change in axial momentum. In the assumption of Templin, the actuator disc is considered as the surface of the imaginary body of revolution. It is assumed that the flow velocity is constant althrough the upstream and the downstream faces of the swept volume. This theory presented by Templin is the first approach to permit numerical design calculations for a vertical-axis Darrieus wind turbine.

This model affords a great deal of simplicity and can predict the overall performance of a lightly loaded wind turbine but according to the investigation, it always predicts higher power than the experimental results. It is incapable of adequately predicting the wind velocity variations across the rotor. This variations gradually increases with the increase of blade solidity and the tip speed ratio.

An analytical method using single streamtube model is presented by Noll and Ham [31] for the performance prediction of

a vertical-axis wind turbine with straight-blades which are cyclically pitched. They added the effect of strut drag, turbulent wake state and dynamic stall to their analytical method.

Improved prediction methods for the calculation of performance characteristics of a Darrieus wind turbine is the multiple streamtube model introduced by Wilson and Lissaman [46]. In this model the swept volume of the turbine is divided into a series of adjacent, aerodynamically independent streamtubes. Blade element and momentum theories are then applied for each streamtube. In their method they consider the flow as inviscid and incompressible for the calculation of the induced velocity through the streamtube. As a result, there appears only the lift force in the calculation of induced velocity. Wilson et al considered the theoretical lift for their calculation. Atmospheric wind shear can be included in the multiple streamtube model. Multiple streamtube model is still inadequate in its description of the flow field. Wilson's model can be applied only for a fast running lightly loaded wind turbine.

Strickland [40] in his paper presents a multiple streamtube model for a vertical-axis Darrieus wind turbine. He finds the induced velocity by equating the blade element forces (induced airfoil drag) and the change in the momentum along each streamtube. The basic difference between Wilson's and Strickland's model is that Wilson used the lift force (theoretical) only in the calculation of induced velocity while Strickland added the effect of drag force as well for the similar calculation.

The effect of local Reynolds number on the lift-drag characteristics is not included. This model predicts the overall performance of a Darrieus wind turbine reasonably especially when the rotor is lightly loaded. It displays improvement over the single streamtube methods.

Streamtube models with both uniform and non-uniform velocity distributions are presented by Shankar [36]. In his uniform velocity distribution model, the axial-flow velocity in the vertical and horizontal directions of the rotor (curved-bladed) frontal area and both in the upwind and downwind sides of the rotor is assumed to be constant. Shankar's non-uniform velocity distribution model is actually the multiple streamtube model where the axial-flow velocity varies both in the vertical and horizontal directions but in each streamtube it remains constant throughout the upwind and downwind sides. In the calculation of Shankar, he applied the lift-drag characteristics independent of Reynolds number like that of Strickland.

Sharpe [37] in his report gives an elaborate description of a multiple streamtube model whose principal idea is similar to that of Strickland [40]. He incorporates the effect of Reynolds number in the calculation. Furthermore he uses analytical expression for the Troposkien shape.

Read and Sharpe [33] have carried out an improved version of multiple streamtube methods for vertical-axis Darrieus wind turbines. In their model the parallel streamtube concept is dispensed with and the expansion of the streamtube is included.

It is strictly applicable to low solidity lightly loaded wind turbines with large aspect ratio. It can predict the instantaneous aerodynamic blade forces and the induced velocities better than that by the conventional multiple streamtube model. But prediction of overall power coefficients can not be made with reasonable accuracy. It usually gives lower power than that obtained experimentally.

Migliore and Wolfe [26] have performed an elaborate study of the flow curvature effect on the performance characteristics of a straight-bladed Darrieus wind turbine. In their method they consider the curved flow consisting of concentric streamlines pattern on the turbine blade airfoils (geometric airfoils). By conformal mapping techniques the geometric airfoil is transformed into a virtual airfoil with change in camber and incidence angle appearing in the rectilinear flow. They have observed strong influence of flow curvature on the performance characteristics of a Darrieus wind turbine especially when the chord-radius ratio is high. They also noted that under most circumstances flow curvature effect has a detrimental influence on the blade aerodynamic efficiency. However, when properly considered, virtual aerodynamics may be used advantageously to enhance turbine performance. In addition they describe the effect of centrifugal forces on the flow pattern of the blade airfoils of the turbine.

Larsen [22] in his paper first presents a vortex theory. He used his vortex model for the performance prediction of a cyclogiro windmill. His model is a two dimensional one but if the vortex trailing from the rotor blade tips are considered it

may not be said strictly two-dimensional. However in his model angle of attack is assumed small, as a result stall effect is neglected.

A vortex model applicable to a curved bladed Darrieus wind turbine have been presented by Strickland, Webster and Nguyen [41] . It is simply the extension of the previous vortex models. This vortex model is a three dimensional one and aerodynamic stall is incorporated into the model.

Mandal A. C [25] in his Ph.D. Thesis presents a cascade theory model for vertical-axis Darrieus wind turbine. He has found that, cascade theory gives reasonably good performance prediction for a high solidity (above .25 approximately) as well as low solidity (below 0.25) Darrieus wind turbine. This theory can reasonably predict the local forces developed on the turbine blade. These are comparable with those calculated by the quasisteady vortex model presented by Strickland [40] .

For the prediction of overall performance of a high solidity straight-bladed Darrieus wind turbine and local forces of both low and high solidity turbines at the high tip speed ratio, application of cascade theory gives more reliable results in comparison to those by the multiple streamtube theory with flow curvature effect.

This theory does not make any convergence problem even for a high solidity turbine and at high tip speed ratio. In this model unlike in the case of momentum theory, the iterated induced velocity ratio may go below 0.50. Applying cascade theory the wake velocities can be predicted very reasonably even for a high solidity turbine and at high tip speed ratio while the momentum theory can not do so.

CHAPTER 3 : AERODYNAMIC THEORIES OF TURBINE

Many aerodynamic theories have been developed upto now to predict the performance of a vertical-axis Darrieus wind turbine. These are single streamtube theory, multiple streamtube theory, vortex theory and cascade theory.

3.1 Single Streamtube Theory

In the single streamtube theory [42], the whole rotor is assumed to be enclosed within the single streamtube. Although the rotor, the axial velocity is assumed to be constant. The forces on the blade airfoil are computed based on the uniform velocity on the rotor. The wind velocity in the streamtube at the rotor is related to the undisturbed freestream velocity by equating the streamwise drag force to the change of fluid momentum through the rotor.

3.1.1 Drag Force Along Streamtube

Based on the Glauert Actuator disc theory, the uniform velocity through the rotor (figure 3.1) is given by the following expression,

$$V_a = \frac{V_\infty + V_w}{2} \quad (3.1)$$

where, V_a is the axial flow velocity (induced velocity) through the rotor, V_∞ is the freestream velocity and V_w is the wake velocity.

Due to the rate of change of momentum, the drag force along the streamtube is,

$$F_D = \dot{m} (V_\infty - V_w) \quad (3.2)$$

where \dot{m} is the mass flow rate. Introducing $\dot{m} = \rho V_a A$,

$$F_D = \rho V_a A (V_\infty - V_w) \quad (3.3)$$

where A is the turbine projected area while ρ is the fluid density. From the equation (3.1) and (3.3), the drag force F_D can be obtained as,

$$F_D = 2\rho V_a A (V_\infty - V_a) \quad (3.4)$$

Rotor drag coefficient is defined by,

$$C_{DD} = \frac{F_D}{\frac{1}{2}\rho A V_a^2} \quad (3.5)$$

Introducing the value of F_D from equation (3.4), the expression of C_{DD} is obtained as,

$$C_{DD} = 4 \left(\frac{V_\infty - V_a}{V_a} \right) \quad (3.6)$$

Corresponding to the figure (3.2), the elemental drag force along the freestream velocity direction based on the aerodynamic forces on the elemental blade airfoil is found as,

$$\delta F_D = \delta F_n \sin\theta - \delta F_t \cos\theta \quad (3.7)$$

where θ is the azimuth angle. δF_n and δF_t are respectively the elemental normal and tangential forces on the elemental blade airfoil.

3.1.2 Blade Element Angles and Velocities

Figure 3.3 shows the air velocities relative to an airfoil element. If the blade moves with ω rad/sec in still air, the air velocity relative to the blade is $R\omega$ and acts in the opposite direction to the blade motion. From the induced velocity V_a and the tangential velocity $R\omega$, R being the radius of the turbine, one obtains the velocity in chordal direction as,

$$V_c = R\omega + V_a \cos\theta \quad (3.8)$$

and the velocity in the normal direction to the blade flight path as,

$$V_n = V_a \sin\theta \quad (3.9)$$

Now the resultant velocity W relative to the airfoil which is called the relative flow velocity becomes,

$$W^2 = V_c^2 + V_n^2 = (R\omega + V_a \cos\theta)^2 + (V_a \sin\theta)^2 \quad (3.10)$$

where the values of V_c and V_n are respectively taken from the equations (3.8) and (3.9). Now rearranging the equation (3.10), one obtains,

$$\frac{W}{V_a} = \sqrt{\left[\left(\frac{R\omega}{V_\infty} / \frac{V_a}{V_\infty} \right) + \cos\theta \right]^2 + \sin^2\theta} \quad (3.11)$$

where the term $R\omega / V_\infty$ is the tip speed ratio λ . Now the angle of attack is obtained as (figure 3.3),

$$\tan \alpha = \frac{V_n}{V_c} = \frac{V_a \sin\theta}{R\omega + V_a \cos\theta} = \frac{\sin\theta}{\frac{R\omega}{V_\infty} / \frac{V_a}{V_\infty} + \cos\theta} \quad (3.12)$$

$$\alpha = \tan^{-1} \left[\frac{\sin \theta}{\frac{R\omega}{V_\infty} / \frac{V_a}{V_\infty} + \cos \theta} \right] \quad (3.13)$$

where α is the local angle of attack.

3.1.3 Aerodynamic Forces

Figure 3.4 shows the blade airfoil cross-section with the aerodynamic forces acting on it. The elemental normal force δF_n and the tangential force δF_t are respectively perpendicular and parallel to the airfoil chord line. The elemental normal and tangential forces are defined as,

$$\delta F_n = \frac{1}{2} C_n \rho W^2 c H \quad (3.14)$$

$$\delta F_t = \frac{1}{2} C_t \rho W^2 c H \quad (3.15)$$

where C_n and C_t are respectively the normal and tangential force coefficients while c is the blade chord which occurs within the elemental angle $\delta\theta$. H is the height of the turbine. Two dimensional elemental lift and drag forces on an elemental blade airfoil are resolved into δF_n and δF_t , which may be obtained referring to the figure 3.4.

$$\delta F_n = \delta L \cos \alpha + \delta D \sin \alpha \quad (3.16)$$

$$\delta F_t = \delta L \sin \alpha - \delta D \cos \alpha \quad (3.17)$$

where the elemental lift force δL and the elemental drag force δD are defined as,

$$\delta L = \frac{1}{2} C_l \rho W^2 c H \quad (3.18)$$

$$\delta D = \frac{1}{2} C_d \rho W^2 c H \quad (3.19)$$

where C_l and C_d are respectively the lift and drag coefficients.

Now from equation (3.14) to (3.19) one may find,

$$C_n = C_l \cos\alpha + C_d \sin\alpha \quad (3.20)$$

$$C_t = C_l \sin\alpha - C_d \cos\alpha \quad (3.21)$$

3.1.4 Velocity Ratio and Power Coefficient

Introducing the values of δF_n (3.14) and δF_t (3.15) in equation (3.7), the elemental streamwise drag force can be obtained as,

$$\delta F_D = \frac{1}{2} \rho c W^2 (C_n \sin\theta - C_t \cos\theta) H \quad (3.22)$$

Now for an assumption of infinite number of blades distribution, replacing c by $NC \delta\theta/2\pi$, N being the number of blades, dynamic pressure $q = \frac{1}{2} \rho W^2$, one may obtain from the equation (3.22) in integration form,

$$F_D = \frac{NC H}{2\pi} \int_0^{2\pi} q (C_n \sin\theta - C_t \cos\theta) d\theta \quad (3.23)$$

Now from the equation (3.5) and (3.23), the drag coefficient C_{DD} may be found as,

$$C_{DD} = \frac{NC}{4\pi R} \int_0^{2\pi} \left(\frac{W}{V_a}\right)^2 (C_n \sin\theta - C_t \cos\theta) d\theta \quad (3.24)$$

Now from the equation (3.6), the velocity ratio $R\omega / V_\infty$ based on the ambient wind speed may be expressed as

$$\frac{R\omega}{V_\infty} = \frac{R\omega}{V_a} \left(\frac{1}{1 + \frac{C_{DD}}{4}} \right) \quad (3.25)$$

For a given turbine geometry, rotational speed ω and specified

rotor velocity ratio $R\omega/V_a$, the rotor drag coefficient C_{DD} can be calculated from the equation (3.24). The velocity ratio $R\omega/V_\infty$ based on the ambient wind speed can be obtained from the equation (3.25). Thus this method does not require any iterative process. The elemental torque is given by,

$$\delta Q = \delta F_t R \quad (3.26)$$

Now substituting equation (3.15) and replacing c by $NC \delta\theta/2\pi$ for an assumption of infinite number of blades distribution, one obtains the expression of overall torque Q in the integration form,

$$Q = \frac{NC}{2\pi} \cdot RH \int_0^{2\pi} C_t q d\theta \quad (3.27)$$

The overall power P_o is,

$$P_o = Q\omega = \frac{NC\omega}{2\pi} \cdot RH \cdot \int_0^{2\pi} C_t q d\theta \quad (3.28)$$

According to Glauert, the expression for the maximum power (ideal power) is,

$$P_{max} = \frac{16}{27} \cdot \frac{1}{2} \rho V_\infty^3 A \quad (3.29)$$

Templin defines the power coefficient as,

$$C_p = \frac{P_o}{P_{max}} \quad (3.30)$$

3.2 Multiple Streamtube Theory (Wilson's Approach)

In the multiple streamtube theory a series of streamtubes parallel to the freestream velocity direction are assumed to pass through the rotor. This model gives rise to a velocity

distribution through the rotor in horizontal direction.

3.2.1 Basic Assumptions

Multiple streamtube theory includes the following assumptions:

- 1) To determine the induced velocity the flow is assumed to be inviscid and incompressible. As a result the lift force is the only force which acts on the blade element and its component along the streamtube is equated to the force contributed by the rate of change of momentum along the streamtube.
- 2) The blades are infinite in number causing the swept surface to be continuous at all times but in such a way that the solidity remains finite.
- 3) Each streamtube may be considered independently with no interference of adjacent tubes and hence the momentum theorem is applied to each of the tube separately.
- 4) The streamtubes are considered to be parallel with each other. So the induced velocity remains constant along each of the streamtube.
- 5) The flow is assumed to be steady, one-dimensional, frictionless, and incompressible.

3.2.2 Axial Momentum Theory

To find the streamwise force along the streamtube, the axial momentum theory is applied. In the figure 3.5 an elemental

Streamtube is shown for a straight-bladed Darrieus wind turbine. The cross-sectional area δA of the elemental streamtube is obtained as,

$$\delta A = H R \sin\theta \delta\theta \quad (3.31)$$

The flow around the airfoil blade element is retarded in two stages. Once before and once after its passage through the blade elements on the either side of the streamtube (figure 3.6). The elemental force along the streamtube is given by,

$$\delta F_D = \delta \dot{m} (V_\infty - V_w) \quad (3.32)$$

where $\delta \dot{m}$ is the mass flow rate through the streamtube, Introducing the elemental mass flow rate $\delta \dot{m} = \rho V_a \delta A$, elemental drag force becomes,

$$\delta F_D = \rho V_a (V_\infty - V_w) \delta A \quad (3.33)$$

Applying Bernoulli's equation in the upstream and the downstream sides respectively one obtains,

$$P_\infty + \frac{1}{2} \rho V_\infty^2 = P_u + \frac{1}{2} \rho V_a^2 \quad (3.34)$$

$$P_\infty + \frac{1}{2} \rho V_w^2 = P_d + \frac{1}{2} \rho V_a^2 \quad (3.35)$$

where P_u and P_d are respectively the static pressure at the upstream end of a streamtube as it enters the swept volume and that at the downstream end of a streamtube as it leaves the swept volume. P_∞ is the atmospheric pressure. Now subtracting the above two equations,

$$P_u - P_d = \frac{1}{2} \rho (V_\infty^2 - V_w^2) \quad (3.36)$$

The elemental force along the streamtube is,

$$\delta F_D = (P_u - P_d) \delta A \quad (3.37)$$

substituting the equation (3.36) into the equation (3.37), one may obtain,

$$\delta F_D = \frac{1}{2} \rho (V_\infty^2 - V_w^2) \delta A \quad (3.38)$$

Now balancing the equations (3.33) and (3.38),

$$\rho V_a (V_\infty - V_w) \delta A = \frac{1}{2} \rho (V_\infty^2 - V_w^2) \delta A \quad (3.39)$$

The above equation finally becomes,

$$V_w = 2V_a - V_\infty \quad (3.40)$$

According to the assumptions of the theory, the induced flow velocity cannot be greater than half of the free stream velocity. Other wise, the wake velocity will either be zero or negative. In the real flow field this does not appear. The wake region is turbulent, as a result there occurs mixing of the wake with the high energy fluid layers outside the wake region.

From the equations (3.33) and (3.40), the elemental force becomes,

$$\delta F_D = 2 \rho V_a (V_\infty - V_a) \delta A \quad (3.41)$$

Introducing the value of δA , the above equation becomes,

$$\delta F_D = 2 R \rho \sin\theta V_a (V_\infty - V_a) H \delta\theta \quad (3.42)$$

Introducing a non-dimensional parameter $h = H/R$,

$$\delta F_D = 2R^2 \rho \sin\theta V_a (V_\infty - V_a) h \delta\theta \quad (3.43)$$

3.2.3 Blade Element Force Along Streamtube

Wilson and Lissaman [46] consider a theoretical lift coefficient in their calculation, which is given by,

$$C_1 = 2 \pi \sin \alpha \quad (3.44)$$

To take into account the real lift coefficient, it may be expressed as,

$$C_1 = 2 \pi k \sin \alpha \quad (3.45)$$

The value of C_1 is taken from the airfoil data corresponding to the local angle of attack while the value of the factor k is found by an iterative process.

For an inviscid and incompressible fluid, the elemental lift force, from the Kutta-Joukowski relations is given by,

$$\delta L = \rho W H \delta \Gamma \quad (3.46)$$

where $\delta \Gamma$ is the elemental circulation for unit length of the blade and W is the relative flow velocity. The elemental lift force, according to the equation (3.18) is,

$$\delta L = \frac{1}{2} C_1 \rho c W^2 H \quad (3.47)$$

From the equations (3.46) and (3.47) the expression of the elemental circulation is found as,

$$\delta \Gamma = \frac{1}{2} c C_1 W \quad (3.48)$$

Introducing the equation (3.45) for the lift coefficient C_1 one obtains,

$$\delta \Gamma = \pi k c W \sin \alpha \quad (3.49)$$

The above equation can be expressed in vector form as,

$$\delta \vec{r} = \pi k c W \sin \alpha \vec{e}_r \quad (3.50)$$

where \vec{e}_r is the unit vector in the direction of $\delta \vec{r}$

The above equation may also be written as,

$$\delta \vec{r} = \pi k c \vec{W} \times \vec{e}_c \quad (3.51)$$

where \vec{e}_c is the unit vector in the chordal direction. For an inviscid and incompressible fluid the elemental force on the blade element can be expressed in vector form as,

$$\delta \vec{F} = \rho H \vec{W} \times \delta \vec{r} \quad (3.52)$$

Now referring to the figure 3.7, the expression of the relative flow velocity \vec{W} and unit vector \vec{e}_c becomes,

$$\vec{W} = V_n \vec{i} + V_c \vec{j} = V_a \sin \theta \vec{i} + (R\omega + V_a \cos \theta) \vec{j} \quad (3.53)$$

$$\text{and } \vec{e}_c = \vec{j} \quad (3.54)$$

where the unit vectors \vec{i} and \vec{j} are considered respectively along the normal direction to the blade chord and the tangential velocity direction. The values of V_c and V_n are taken from the equations (3.8) and (3.9) respectively. Inserting the values of \vec{W} and \vec{e}_c in the equation (3.51) one obtains,

$$\delta \vec{r} = \pi k c [V_a \sin \theta \vec{i} + (R\omega + V_a \cos \theta) \vec{j}] \times \vec{j} \quad (3.55)$$

Considering the unit vector \vec{k} perpendicular to the plane of the unit vectors \vec{i} , \vec{j} ; since $\vec{i} \times \vec{j} = \vec{k}$ and $\vec{j} \times \vec{j} = 0$, the above equation becomes

$$\delta \vec{v} = \pi k c v_a \sin \theta \vec{k} \quad (3.56)$$

Introducing the values of \vec{W} (3.53) and $\delta \vec{v}$ (3.56) in the equation (3.52) one may obtain,

$$\delta \vec{F} = \rho \pi k c \left[v_a \sin \theta \vec{i} + (R\omega + v_a \cos \theta) \vec{j} \right] H \times (v_a \sin \theta \vec{k}) \quad (3.57)$$

After vector multiplication, the elemental force $\delta \vec{F}$ becomes

$$\delta \vec{F} = \rho \pi k c H \left[(R\omega v_a \sin \theta + v_a^2 \sin \theta \cos \theta) \vec{i} - v_a^2 \sin^2 \theta \vec{j} \right] \quad (3.58)$$

The equation (3.58) can be written in the following form,

$$\delta \vec{F} = \rho \pi k c H (F_1 \vec{i} + F_2 \vec{j}) \quad (3.59)$$

where $F_1 = R\omega v_a \sin \theta + v_a^2 \sin \theta \cos \theta$

and $F_2 = -v_a^2 \sin^2 \theta$

Now referring to the figure 3.8, the elemental force component on the blade element along the streamtube is,

$$\delta F_D = \rho \pi k c H (F_1 \sin \theta + F_2 \cos \theta) \quad (3.60)$$

Equation (3.60) may be obtained in the following form after introducing the values of F_1 and F_2 ,

$$\delta F_D = \rho \pi k c R\omega H v_a \sin^2 \theta \quad (3.61)$$

Now introducing a non-dimensional parameter $h = H/R$ and replacing c by $\frac{N C \delta \theta}{2\pi}$ for an assumption of infinite number of blades distribution, δF_D may be expressed as,

$$\delta F_D = \frac{1}{2} \rho k N C R^2 h \omega V_a \sin^2 \theta \delta \theta \quad (3.62)$$

Now multiplying the equation (3.62) by 2 for two blade elements in one streamtube, one finds,

$$\delta F_D = \rho k N C R^2 h \omega V_a \sin^2 \theta \delta \theta \quad (3.63)$$

3.2.4 Induced Velocity Ratio, Aerodynamic Forces and Power Coefficient.

To find the induced velocity ratio, the relative flow velocity W , the local angle of attack α and the local Reynolds number R_e are necessary. The relative flow velocity W and angle of attack α may be obtained from the equations (3.11) and (3.13), which are given below,

$$\frac{W}{V_a} = \sqrt{\left[\left(\frac{R\omega}{V_\infty} \frac{V_a}{V_\infty} \right) + \cos \theta \right]^2 + \sin^2 \theta} \quad (3.64)$$

$$\alpha = \tan^{-1} \left[\frac{\sin \theta}{\frac{R\omega}{V_\infty} \frac{V_a}{V_\infty} + \cos \theta} \right] \quad (3.65)$$

The local Reynolds number R_e for the constant wind speed condition is expressed in the form,

$$R_e = \frac{WC}{\nu} = \frac{W}{V_a} \cdot \frac{V_a}{V_\infty} \cdot \frac{V_\infty C}{\nu} = \frac{W}{V_a} \cdot \frac{V_a}{V_\infty} \cdot R_{ew} \quad (3.66)$$

and that for the constant turbine speed condition is expressed in the form,

$$R_e = \frac{WC}{\nu} = \frac{W}{V_a} \cdot \frac{V_a}{V_\infty} \cdot \left(\frac{R\omega C}{\nu} \right) / \left(\frac{R\omega}{V_\infty} \right) = \frac{W}{V_a} \cdot \frac{V_a}{V_\infty} \cdot \frac{R_{et}}{\lambda} \quad (3.67)$$

where R_{ew} ($= V_\infty C / \nu$) is the wind speed Reynolds number and R_{et} ($= \frac{R\omega C}{\nu}$) is the turbine speed Reynolds number.

Now from the equations (3.43) and (3.63), one may obtain the expression of the induced velocity ratio (rotor axial flow velocity) as,

$$\frac{V_a}{V_\infty} = 1 - \frac{k}{2} \cdot \frac{NC}{R} \cdot \frac{R\omega}{V_\infty} \sin\theta \quad (3.68)$$

The value of the induced velocity ratio is obtained by an iterative process. For known values of tip speed ratio $\lambda (= R\omega/V_\infty)$, solidity ratio $\delta (= NC/R)$, azimuth angle θ , the starting value of the induced velocity ratio is chosen as 1.0 or as that calculated for the prior streamtube. Now the relative flow velocity W and the local angle of attack α are respectively calculated from equation (3.11) and (3.13). Then the local Reynolds number R_e is calculated either from the equation (3.66) for constant wind speed condition or from the equation (3.67) for constant turbine speed condition. With the known values of R_e and α , the value of the lift coefficient is taken from the airfoil data and the factor k is calculated from the equation (3.45). Now the new value of the induced velocity ratio is calculated by using the equation (3.68). This process is continued until the induced velocity ratio is obtained with desired accuracy.

The elemental blade pitching moment is defined by,

$$\delta M = \frac{1}{2} C_m \rho W^2 c H C \quad (3.69)$$

The non-dimensional normal force F_n^+ and the non-dimensional tangential force F_t^+ are defined in the following way,

$$F_n^+ = \frac{\delta F_n}{\frac{1}{2} \rho c H V_\infty^2} \quad (3.70)$$

$$F_t^+ = \frac{\delta F_t}{\frac{1}{2} \rho c H V_\infty^2} \quad (3.71)$$

Introducing the values of δF_n (3.14) and δF_t (3.15) in the above equations (3.70) and (3.71) respectively, one obtains,

$$F_n^+ = C_n \frac{W^2}{V_\infty^2} \quad (3.72)$$

$$F_t^+ = C_t \frac{W^2}{V_\infty^2} \quad (3.73)$$

Referring to the figure 3.9, the elemental streamwise drag force is,

$$\delta F_D = 2 (\delta F_n \sin\theta - \delta F_t \cos\theta) \quad (3.74)$$

Introducing the value of δF_n (3.14) and δF_t (3.15) respectively in the above equation (3.74), one finds,

$$\delta F_D = \rho c W^2 (C_n \sin\theta - C_t \cos\theta) H \quad (3.75)$$

Replacing c by $NC \delta\theta/2\pi$ for an assumption of infinite number of blades distribution and introducing a non-dimensional parameter $h = H/R$, the equation (3.75) can be written as,

$$\delta F_D = \frac{NC}{2\pi R} \cdot \rho W^2 R^2 (C_n \sin\theta - C_t \cos\theta) h \delta\theta \quad (3.76)$$

Coefficient of overall elemental turbine drag (streamwise force) is defined as,

$$\delta C_D = \frac{\delta F_D}{\frac{1}{2} \rho A V_\infty^2} \quad (3.77)$$

where $A (= 2RH)$ being the projected frontal area of the swept volume. Now the expression of the turbine overall elemental drag coefficient can be obtained as,

$$\delta C_D = \frac{NC}{\pi R} \cdot \frac{R^2}{A} \cdot h \cdot \left(\frac{W}{V_\infty} \right)^2 (C_n \sin\theta - C_t \cos\theta) \delta\theta \quad (3.78)$$

Integrating the equation (3.78), the turbine overall drag coefficient can be obtained as,

$$C_D = \frac{NC}{2\pi R} \int_0^\pi \frac{W^2}{V_\infty^2} (C_n \sin\theta - C_t \cos\theta) d\theta \quad (3.79)$$

The blade elemental torque of the turbine is found as,

$$\delta Q = \delta F_t R + \delta M \quad (3.80)$$

From the equations (3.15), (3.69) and (3.80) one obtains,

$$\delta Q = \frac{1}{2} \rho c W^2 (RC_t + CC_m) H \quad (3.81)$$

Inserting the non-dimensional parameter is $h = H/R$ and replacing c by $NC \delta\theta/2\pi$ for an assumption of infinite number of blades distribution, δQ may be expressed as,

$$\delta Q = \frac{NC}{4\pi R} \rho R^3 W^2 (C_t + \frac{C}{R} C_m) h \delta\theta \quad (3.82)$$

The overall elemental torque coefficient is defined as,

$$\delta C_Q = \frac{\delta Q}{\frac{1}{2} \rho A V_\infty^2 R} \quad (3.83)$$

From the equation (3.82) and (3.83), the expression of δC_Q is obtained as,

$$\delta C_Q = \frac{NC}{2\pi R} \cdot \frac{R^2}{A} \cdot \frac{W^2}{V_a^2} (C_t + \frac{C}{R} C_m) \frac{V_a^2}{V_\infty^2} \cdot h \delta\theta \quad (3.84)$$

After integration, the turbine overall torque coefficient is expressed as,

$$C_Q = \frac{N C}{4\pi R} \int_0^{2\pi} \frac{W^2}{V_\infty^2} \left(C_t + \frac{C}{R} C_m \right) \frac{V_a^2}{V_\infty^2} d\theta \quad (3.85)$$

The overall power coefficient C_p (may also be called as the aerodynamic efficiency) is defined as the ratio of the power P_o produced by the turbine to the total power available in the air passing through the same swept volume of the turbine and is given by,

$$C_p = \frac{P_o}{\frac{1}{2} \rho A V_\infty^3} \quad (3.86)$$

Introducing the value of overall power $P_o = Q\omega$, one obtains,

$$C_p = \frac{Q\omega}{\frac{1}{2} \rho A V_\infty^3} = \frac{Q}{\frac{1}{2} \rho A V_\infty^2 R} \cdot \frac{R\omega}{V_\infty} = C_Q \cdot \lambda \quad (3.87)$$

Inserting the value of C_Q from the equation (3.85), the overall power coefficient C_p may be found at any particular tip speed ratio λ . The power coefficient is calculated by the numerical integration method applying Simpson's rule.

3.3 Vortex Theory

Strickland, Webster and Nguyen [9] have presented three dimensional vortex model. In this model aerodynamic stall may be encountered. The general analytical approach requires that the rotor blades be divided into a number of segments along their span. The production, convection and interaction of vortex systems springing from the individual blade elements are modeled and used to predict the "induced velocity" or "perturbation velocity" at various points in the flow field. The induced or perturbation velocity at a point is simply the velocity which is superimposed on the undisturbed wind stream by the wind machine.

Having obtained the induced velocities, the lift and drag of the blade segment can be obtained using airfoil section data.

A simple representation of the vortex system associated with a blade element is shown in the figure 3.10. The airfoil blade element is replaced by a "bound" vortex filament sometimes called "substitution" vortex filament or a lifting line. The strengths of the bound vortex and each trailing tip vortex are equal as a consequence of the Helmholtz theorems of vorticity. According to the figure 3.10, the strengths of the shed vortex systems have changed on several occasions. On each of these occasions, a spanwise vortex is shed whose strength is equal to the change in the bound vortex strength as dictated by Kelvin's theorem.

The fluid velocity at any point in the flow field is the sum of the undisturbed wind stream velocity and the velocity induced by all of the vortex filaments in the flow field. The velocity induced at a point in the flow field by a single vortex filament can be obtained from the Biot-Savart law, which relates the induced velocity to the filament strength. Referring to the case shown in the figure 3.11, for a straight vortex filament of strength Γ and length l , the induced velocity \vec{V}_p at a point p not on the filament is given by,

$$\vec{V}_p = \vec{e} \frac{\Gamma}{4\pi d} (\cos\theta_1 + \cos\theta_2) \quad (3.88)$$

Where d is the minimum distance of the point p from the vortex filament, \vec{e} is the unit vector in the direction of $\vec{r} \times \vec{l}$. \vec{r} is also the unit vector. It should be noted that if point p

should happen to lie on the vortex filament, equation (3.88) yields indeterminate results, since \vec{e} cannot be defined and the magnitude of \vec{V}_p is infinite. The velocity induced by a straight vortex filament on itself is, in fact, equal to zero.

In order to allow closure of the vortex model, a relationship between the bound vortex strength and the velocity induced at a blade segment must be obtained. A relationship between the lift L per unit span on a blade segment and the bound vortex strength Γ_B is given by the Kutta-Joukowski law. The lift can also be formulated in terms of the airfoil section lift coefficient C_l . Equating these two expressions for the lift, yields the required relationship between the bound vortex strength and the induced velocity at a particular blade segment.

$$\Gamma_B = \frac{1}{2} C_l C W \quad (3.89)$$

It should be noted that the effects of aerodynamic stall are automatically introduced into the equation (3.89) through the section lift coefficient. After determining the induced velocity distribution, it becomes straight-forward to obtain the performance characteristics of a Darrieus rotor.

3.4 Cascade Theory

In the cascade theory [25], the blade airfoils of a turbine are assumed to be positioned in a plane surface (termed as cascade) with the blade interspace equal to the turbine circumferential distance divided by the number of blades. In this model

the relationship between the wake velocity and the freestream velocity is established by using the Bernoulli's equation while the induced velocity is related to the wake velocity through a particular assumed analytical expression.

3.4.1 Basic Assumptions

In order to simplify the analysis with cascade theory for the determination of the performance characteristics of a Darrieus wind turbine the following assumptions are made:

- 1) The blades on the cylindrical surface (cylinder with height H) are assumed to be developed into a plane surface. This configuration is known as the rectilinear cascade.
- 2) As the turbine blade rotates in a circular path, the flow velocity on the blade continuously varies; as a result at any instant each of the turbine blades faces flow conditions different from those on others. In the present analysis one of the blades is considered as the reference blade and at any instant power is calculated with supposition that each of the blades sees the same flow and produces the same power as that of the reference blade. This process is continued at every station with the reference blade for one complete revolution of the turbine. Later the average power is obtained.
- 3) The wake velocity for the upstream side is supposed to act in the axial direction and behaves as the freestream velocity on the downstream blade which is positioned behind the

upstream blade. The pressure in the wake region of the upstream side is assumed to be equal to the atmospheric pressure.

- 4) During finding the wake velocity the flow is assumed to be steady, One-dimensional and incompressible.

3.4.2 Blade Element Angles and Velocities

In the present analysis the flow velocities in the upstream and the downstream sides of the turbine are not constant (Figure 3.12). From the figure 3.12, it may be observed that the flow is considered to occur in the axial direction. The expressions of the chordal velocity component V_{cu} , the normal velocity component V_{nu} for the upstream side are respectively obtained following the equation (3.8) and (3.9) in the section 3.1.2.

$$V_{cu} = R\omega + V_{au} \cos\theta \quad (3.90)$$

$$V_{nu} = V_{au} \sin\theta \quad (3.91)$$

Referring to the figure 3.12, the angle of attack α_{ou} for the upstream side may be expressed as,

$$\alpha_{ou} = \tan^{-1} \left(\frac{V_{nu}}{V_{cu}} \right) \quad (3.92)$$

Introducing the value of V_{nu} and V_{cu} and non-dimensionalizing,

$$\alpha_{ou} = \tan^{-1} \left[\frac{\sin\theta}{\left(\frac{R\omega}{V_{\infty}} / \frac{V_{au}}{V_{\infty}} \right) + \cos\theta} \right] \quad (3.93)$$

The relative flow velocity W_{ou} for the upstream side is obtained as (Figure 3.13).

$$W_{ou} = \sqrt{V_{cu}^2 + V_{nu}^2} \quad (3.94)$$

After inserting the values of V_{cu} (3.90) and V_{nu} (3.91) and non-dimensionalizing the equation (3.94) becomes,

$$\frac{W_{ou}}{V_{\infty}} = \frac{W_{ou}}{V_{au}} \cdot \frac{V_{au}}{V_{\infty}} = \frac{V_{au}}{V_{\infty}} \sqrt{\left[\left(\frac{R\omega}{V_{\infty}} \frac{V_{au}}{V_{\infty}} \right) + \cos\theta \right]^2 + \sin^2\theta} \quad (3.95)$$

Following the same procedure, similar expressions are obtained for the downstream side. Hence to determine the angle of attack α_{od} and the relative flow velocity W_{od} for the downstream side subscript u is replaced by d in equations (3.93) and (3.95).

After determination of the local relative flow velocity and the angle of attack, the straight-bladed Darrieus turbine is developed into the cascade configuration which is shown in the figure 3.14. If the blade represented by (1) at an azimuth angle θ is considered as the reference blade, the flow conditions on the other blades represented by (2) and (3), are assumed to be same to that of the reference blade. This process is continued for one complete revolution of the reference blade with a step $\delta\theta$.

In the following analysis, the general mathematical expressions are derived for the upstream and the downstream sides by omitting the subscripts u and d. These general expressions may be applied for both the upstream and downstream sides by subscripting the variable parameters (dependent of sides of turbine) with u (upstream) and d (downstream).

Figure 3.15 shows the velocity diagram on the reference blade element of the cascade configuration for a straight-bladed Darrieus turbine. To perform the analysis a control surface is

chosen as shown in this figure. This control surface consists of two parallel lines to the cascade front and two identical streamlines having interspace t . This figure also shows velocities in reference to the blade element in the cascade. Referring to the figure 3.14, the expressions of these velocities are obtained as,

$$\frac{W_y}{V_\infty} = \frac{W_o}{V_\infty} \cos \alpha_o \quad (3.96)$$

$$\frac{W_x}{V_\infty} = \frac{W_o}{V_\infty} \sin \alpha_o \quad (3.97)$$

$$\frac{W_1^2}{V_\infty^2} = \frac{W_x^2}{V_\infty^2} + \frac{(W_y - V_\Gamma)^2}{V_\infty^2} \quad (3.98)$$

$$\frac{W_2^2}{V_\infty^2} = \frac{W_x^2}{V_\infty^2} + \frac{(W_y + V_\Gamma)^2}{V_\infty^2} \quad (3.99)$$

$$\text{where } V_\Gamma = \frac{\Gamma H}{2t} = \frac{N \Gamma H}{4 \pi R} \quad (3.100)$$

W_x and W_y are the components of the velocity W_o in the x and y directions respectively where x is chosen along the perpendicular direction and y is chosen along the parallel direction of the cascade front (figure 3.14). W_1 and W_2 are the relative flow velocities respectively at the cascade inlet and outlet. Blade airfoil upstream side is termed as cascade inlet and downstream side is termed as cascade outlet. V_Γ is the velocity contributed by circulation Γ . $t (=2\pi R/N)$ is the blade spacing. The angles of attack at the cascade inlet α_1 and outlet α_2 are obtained as,

$$\alpha_1 = \tan^{-1} \left[\frac{W_x/V_\infty}{(W_y - V_\Gamma)/V_\infty} \right] \quad (3.101)$$

$$\alpha_2 = \tan^{-1} \left[\frac{W_x/V_\infty}{(W_y + V_\Gamma)/V_\infty} \right] \quad (3.102)$$

3.4.3 Aerodynamic Forces

Along the bounding streamlines (figure 3.15) the pressure forces are cancelled: Viscous forces can be neglected outside of the boundary layers. There exists only the momentum flux through the straight lines parallel to the cascade front. So the force in the tangential direction due to the rate of change of momentum,

$$F_t = \dot{m} (W_2 \cos \alpha_2 - W_1 \cos \alpha_1) \quad (3.103)$$

Applying the continuity equation the mass flow rate \dot{m} can be found as,

$$\dot{m} = \rho H t W_1 \sin \alpha_1 = \rho H t W_2 \sin \alpha_2 = \rho H t W_x \quad (3.104)$$

From the equation (3.103) and (3.104), the tangential force F_t becomes,

$$F_t = \rho H t (W_2^2 \sin \alpha_2 \cos \alpha_2 - W_1^2 \sin \alpha_1 \cos \alpha_1) \quad (3.105)$$

The force in the normal direction to the cascade may be obtained as

$$F_n = \dot{m} (W_1 \sin \alpha_1 - W_2 \sin \alpha_2) + H t (P_1 - P_2) \quad (3.106)$$

where P_1 and P_2 are respectively the pressures at the cascade inlet and outlet. Introducing the value of \dot{m} (3.104), equation (3.106) can be written as,

$$F_n = \rho H t (W_1^2 \sin^2 \alpha_1 - W_2^2 \sin^2 \alpha_2) + H t (P_1 - P_2) \quad (3.107)$$

Considering the total cascade loss by a total pressure loss term ΔP_{ov} and using Bernoulli's equation between the cascade inlet and outlet, one obtains,

$$\frac{P_1}{\rho g} + \frac{W_1^2}{2g} = \frac{P_2}{\rho g} + \frac{W_2^2}{2g} + \frac{P_{ov}}{\rho g} \quad (3.108)$$

$$\text{Rearranging, } (P_1 - P_2) = \frac{\rho}{2} (W_2^2 - W_1^2) + \Delta P_{ov} \quad (3.109)$$

Now introducing value of $(P_1 - P_2)$ in the equation (3.107) and writing $W_1 \sin \alpha_1 = W_2 \sin \alpha_2$ (for the present configuration), the normal force becomes,

$$F_n = \frac{\rho H t}{2} (W_2^2 - W_1^2) + H t \Delta P_{ov} \quad (3.110)$$

The expressions of the normal force coefficient C_n , the tangential force coefficient C_t , the non-dimensional normal force F_n^+ and the non-dimensional tangential force F_t^+ in the cascade theory are respectively obtained following the equations (3.20), (3.21), (3.72) and (3.73). These are given below (since α_o is identical to α given by the equations (3.20) and (3.21) while W_o is identical to W given by the equations (3.72) and (3.73), α and W are replaced by α_o and W_o respectively).

$$C_n = C_l \cos \alpha_o + C_d \sin \alpha_o \quad (3.111)$$

$$C_t = C_l \sin \alpha_o - C_d \cos \alpha_o \quad (3.112)$$

$$F_n^+ = C_n \frac{W_o^2}{V_\infty^2} \quad (3.113)$$

$$F_t^+ = C_t \frac{W_o^2}{V_\infty^2} \quad (3.114)$$

3.4.4 Velocity Contributed by Circulation and Total Power Loss Term

The circulation about the blade profile is defined as,

$$\Gamma = \oint_s \vec{W} \cdot d\vec{s} \quad (3.115)$$

Its contribution along the streamlines is cancelled by virtue of the opposing directions of s , while the contribution along the parallel direction of the cascade front is retained. As a result the circulation becomes,

$$\Gamma = t (W_2 \cos \alpha_2 - W_1 \cos \alpha_1) \quad (3.116)$$

From the equations (3.103), (3.104) and (3.106) one obtains,

$$F_t = \rho W_x \Gamma H \quad (3.117)$$

Referring to the figure 3.16, the lift force can be written as,

$$L = L_{id} + L_v \quad (3.118)$$

where, L_{id} and L_v are respectively the lift force appearing in frictionless flow and the lift force due to pressure loss.

According to the figure 3.16, L_{id} and L_v may be expressed as,

$$L_{id} = F_t / \sin \alpha_o \quad (3.119)$$

$$L_v = D \cot \alpha_o$$

where D is the drag force on the blade airfoil. The equations (3.118), (3.119) and (3.120) yield,

$$L = F_t / \sin \alpha_o + D \cot \alpha_o \quad (3.121)$$

Dividing both sides of the equation (3.121) by L, introducing $\epsilon = D/L$ and arranging,

$$\frac{F_t}{L \sin \alpha_o} = (1 - \epsilon \cot \alpha_o) \quad (3.122)$$

Rearranging,

$$L = \frac{F_t}{\sin \alpha_o (1 - \epsilon \cot \alpha_o)} \quad (3.123)$$

Introducing the value of F_t from the equation (3.117), the lift force L becomes,

$$L = \frac{\rho W_x H}{\sin \alpha_o} \frac{\Gamma}{(1 - \epsilon \cot \alpha_o)} \quad (3.124)$$

Referring to the figure 3.15, one may write $W_x = W_o \sin \alpha_o$, so the lift force L can be expressed as,

$$L = \rho H W_o \frac{\Gamma}{(1 - \epsilon \cot \alpha_o)} \quad (3.125)$$

The lift force is defined as,

$$L = \frac{1}{2} C_l \rho W_o^2 C H \quad (3.126)$$

From the equations (3.125) and (3.126) the expression of the circulation is obtained as,

$$\Gamma = \frac{1}{2} C_l C W_o (1 - \epsilon \cot \alpha_o) \quad (3.127)$$

Now the expression of V_{Γ} from the equations (3.100) and (3.127) are obtained as,

$$V_{\Gamma} = \frac{1}{8\pi} C_l \frac{NC}{R} W_o (1 - \epsilon \cot \alpha_o) H \quad (3.128)$$

In the non-dimensional form, the equation (3.128) becomes,

$$\frac{V_{\Gamma}}{V_{\infty}} = \frac{1}{8\pi} C_l \frac{NC}{R} \frac{W_o}{V_{\infty}} (1 - \epsilon \cot \alpha_o) H \quad (3.129)$$

Now an expression of the pressure loss term ΔP_{ov} will be derived. From the figure 3.16, the normal force can be obtained as,

$$F_n = F_{nid} + F_{nv} \quad (3.130)$$

Where F_{nid} is the force appearing in the frictionless flow and F_{nv} is the force due to pressure loss. Referring to the figure 3.16, F_{nv} may be expressed as,

$$F_{nv} = \frac{D}{\sin \alpha_o} \quad (3.131)$$

The force F_{nv} may also be expressed as,

$$F_{nv} = H t \Delta P_{ov} \quad (3.132)$$

From the equations (3.131) and (3.132) one obtains,

$$\Delta P_{ov} = \frac{D}{t H \sin \alpha_o} \quad (3.133)$$

The drag force D is defined as,

$$D = \frac{1}{2} C_{d\rho} W_o^2 C H \quad (3.134)$$

Now from the equations (3.133) and (3.134) one obtains,

$$\Delta P_{ov} = \frac{\rho}{2} \frac{C_d}{\sin \alpha_o} \frac{C}{t} W_o^2 \quad (3.135)$$

where $C/t = \frac{NC}{2\pi R} = \frac{1}{2\pi} \cdot \frac{NC}{R}$ (3.136)

In non-dimensionalized form,

$$\frac{\Delta P_{ov}}{\rho V_\infty^2} = \frac{1}{4\pi} \frac{C_d}{\sin \alpha_o} \frac{NC}{R} \frac{W_o^2}{V_\infty^2} \quad (3.137)$$

3.4.5 Velocity Ratios and Rotor Power Coefficient

The wake velocities for the upstream and the downstream sides of the turbine are obtained by applying Bernoulli's equation with absolute velocity and that with relative flow velocity.

Applying Bernoulli's equation with absolute velocity in front and behind the cascade one obtains for the upstream side,

$$\frac{V_\infty^2}{2g} + \frac{P_\infty}{\rho g} = \frac{V_{au}^2}{2g} + \frac{P_{1u}}{\rho g}$$

$$\frac{V_e^2}{2g} + \frac{P_\infty}{\rho g} = \frac{V_{au}^2}{2g} + \frac{P_{2u}}{\rho g} \quad (3.139)$$

where V_{au} and V_e are respectively the induced velocity and the wake velocity for the upstream side. P_{1u} and P_{2u} are the static pressures respectively at the cascade inlet and outlet for the upstream side. In the wake region of the upstream side with the velocity V_e , the pressure is assumed to be equal to the atmospheric

pressure (figure 3.12). ~~Subtracting~~ the above equations (3.138) and (3.139),

$$\frac{V_{\infty}^2}{2g} - \frac{V_e^2}{2g} = \frac{P_{1u}}{\rho g} - \frac{P_{2u}}{\rho g} \quad (3.140)$$

After rearranging,

$$(P_{1u} - P_{2u}) = \frac{\rho}{2} (V_{\infty}^2 - V_e^2) \quad (3.141)$$

Now subscripting the variable parameters in the equation (3.109) by u for the upstream side and balancing with the equation (3.141) one obtains,

$$\frac{\rho}{2} (V_{\infty}^2 - V_e^2) = \frac{\rho}{2} (W_{2u}^2 - W_{1u}^2) + \Delta P_{ov_u} \quad (3.142)$$

Again subscripting the variable parameters in the equation (3.137) by u for the upstream side, introducing in the equation (3.142) and dividing throughout by $\rho/2$ one may find,

$$V_{\infty}^2 - V_e^2 = (W_{2u}^2 - W_{1u}^2) + \frac{1}{2\pi} \cdot \frac{NC}{R} \cdot \frac{C_{du}}{\sin \alpha_{ou}} \cdot W_{ou}^2 \quad (3.143)$$

From the equation (3.143), the expression of the wake velocity ratio in non-dimensionalized form for the upstream side can be written as,

$$\frac{V_e}{V_{\infty}} = \sqrt{1 - \left(\frac{W_{2u}^2}{V_{\infty}^2} - \frac{W_{1u}^2}{V_{\infty}^2} \right) - \frac{1}{2\pi} \left(\frac{NC}{R} \right) \frac{C_{du}}{\sin \alpha_{ou}} \cdot \frac{W_{ou}^2}{V_{\infty}^2}} \quad (3.144)$$

Similarly the expression of the wake velocity ratio in non-dimensionalized form for the downstream side can be found as,

$$\frac{V_w}{V_e} = \sqrt{1 - \left(\frac{W_{2d}^2}{V_e^2} - \frac{W_{1d}^2}{V_e^2} \right) - \frac{1}{2\pi} \left(\frac{NC}{R} \right) \frac{C_{dd}}{\sin \alpha_{od}} \cdot \frac{W_{od}^2}{V_e^2}} \quad (3.145)$$

The wake velocity ratio for the downstream side may be related as,

$$\frac{V_w}{V_\infty} = \frac{V_w}{V_e} \cdot \frac{V_e}{V_\infty} \quad (3.146)$$

In this model, for the upstream side a relationship between the wake velocity and the induced velocity is given as,

$$\frac{V_{au}}{V_\infty} = \left(\frac{V_e}{V_\infty} \right)^{k_i} \quad (3.147)$$

and for the downstream side as,

$$\frac{V_{ad}}{V_e} = \left(\frac{V_w}{V_e} \right)^{k_i} \quad (3.148)$$

The value of the exponent k_i is found from a fit of experimental results. The induced velocity ratio for the down-stream side may also be written in the form,

$$\frac{V_{ad}}{V_\infty} = \frac{V_{ad}}{V_e} \cdot \frac{V_e}{V_\infty} = \frac{V_e}{V_\infty} \left(\frac{V_w}{V_e} \right)^{k_i} \quad (3.149)$$

Induced velocity ratio depends on many parameters such as, solidity, tip speed ratio, azimuth angle, Reynolds number, aspect ratio, blade pitching and airfoil profile. In the iterative process, the effect of every parameter except solidity is taken care of through the airfoil characteristics which control circulation. Thus the exponent k_i becomes the function of solidity only. The expression of the exponent is obtained as,

$$k_i = (.425 + .332\sigma) \quad (3.150)$$

where σ is solidity of a Darrieus wind turbine.

The expressions, for the tangential force F_t and the normal force F_n , may be used for the upstream and the downstream sides by subscripting the variable parameters with u (upstream) and d (downstream). The equations (3.105) and (3.110) are expressed in the following forms inserting $t = 2\pi R/N$.

$$F_t(\theta) = \frac{2\pi}{N} \cdot \rho H R (W_2^2 \sin \alpha_2 \cos \alpha_2 - W_1^2 \sin \alpha_1 \cos \alpha_1) \quad (3.151)$$

$$F_n(\theta) = \frac{\pi}{N} \cdot \rho H R (W_2^2 - W_1^2) + \frac{2\pi}{N} H R \Delta P_{ov} \quad (3.152)$$

Since the tangential and the normal forces represented by the equations (3.151) and (3.152) are for any azimuthal position, so from now on they are considered as a function of azimuth angle θ .

The average tangential force on each blade is expressed as,

$$F_{ta} = \frac{1}{2\pi} \int_0^{2\pi} F_t(\theta) d\theta \quad (3.153)$$

The total torque for the number of blades N is expressed as,

$$Q = N F_{ta} R \quad (3.154)$$

From the equations (3.151), (3.153) and (3.154) one obtains,

$$Q = \rho H R^2 \int_0^{2\pi} (W_2^2 \sin \alpha_2 \cos \alpha_2 - W_1^2 \sin \alpha_1 \cos \alpha_1) d\theta \quad (3.155)$$

The turbine torque coefficient is defined by,

$$C_Q = \frac{Q}{\frac{1}{2} \rho A V_\infty^2 R} \quad (3.156)$$

Introducing the value of Q from the equation (3.155), inserting $A = 2RH$, one may obtain the expression of the turbine overall torque coefficient as,

$$C_Q = \int_0^{2\pi} \left(\frac{W_2^2}{V_\infty^2} \sin \alpha_2 \cos \alpha_2 - \frac{W_1^2}{V_\infty^2} \sin \alpha_1 \cos \alpha_1 \right) d\theta \quad (3.157)$$

The turbine overall power coefficient is given by the equation

$$C_p = \lambda \cdot C_Q \quad (3.158)$$

The numerical calculation to obtain the overall power coefficient is carried out following the procedure given in the Appendix - A.

3.4.6 Blade Pitching

The same expressions as for no blade pitching condition in this theory may be applied for the blade pitching condition after alteration in the angle of incidence only.

Figure 3.17 shows the velocities and the forces acting on the blade airfoil with pitching. In this analysis pitching is considered to be positive for the blade airfoil nose rotating in the outward direction from the blade flight path. As a result for the upstream side the angle of attack becomes,

$$\alpha_u = \alpha_{ou} - \gamma_{pu} \quad (3.159)$$

and for the downstream side the angle of attack becomes,

$$\alpha_d = \alpha_{od} + \gamma_{pd} \quad (3.160)$$

where γ_{pu} and γ_{pd} are the pitch angles in the upstream and the downstream sides respectively. Now the lift and drag characteristics are taken corresponding to α_u (upstream) and α_d (downstream). The parameters shown in the figure 3.17 have not been subscripted to make them generalized. Subscripts u and d are used with the parameters for the upstream and the downstream sides respectively.

CHAPTER 4 : RESULTS AND DISCUSSIONS

In this chapter the calculated results are presented. The effects of a number of parameters such as solidity, blade pitching etc. on the performance characteristics of a straight-bladed Darrieus wind turbine are discussed. Afterwards the calculated values by cascade theory for cambered-blade cross-section are compared with those by cascade and simple multiple streamtube theories for symmetric-blade cross sections of straight-bladed Darrieus wind turbines.

Before going to discuss the theoretical results, it is necessary to mention regarding the lift-drag characteristics of the turbine blade airfoil. Two types of airfoils are included in this analysis. These are NACA 1415 and NACA 0015. The lift-drag values are taken by consulting many references. These are presented by Abott and Von Doenhoff [1] , Clancy [9] , Dommasch [13] , Durand [14] , Mandal [25] , Sharpe [37] . The lift-drag characteristics are presented in graphical forms in the Appendix-D. Aspect ratio effect is also encountered in the analysis which is described in brief in Appendix - E.

4.1 Calculated Results

The numerical results are determined for a straight-bladed Darrieus wind turbine by cascade theory for cambered-blade cross-section. These are presented in the graphical forms. The results of a straight-bladed Darrieus wind turbine are presented and both the overall and local values are included.

Few comparative results of overall values and local values are presented which are calculated by cascade theory with blades of cambered cross-section and multiple streamtube and cascade theories with blades of symmetric cross-section. If blades of cambered cross-section are applied in place of symmetric cross-section and proper blade pitching is employed, improvement in the turbine performance is achieved.

Effect of Solidity:

The effects of solidity on the overall power, torque and drag coefficients of a straight-bladed Darrieus wind turbine calculated by cascade theory with cambered cross-section are respectively shown in the figures 4.1, 4.2 and 4.3. The solidity is varied while the wind speed, blade chord, number of blades and aspect ratio are kept constant. As a result wind speed Reynolds number become fixed. Solidity is changed with the change of radius. The figure 4.1 reveals that the maximum power coefficient appears at a solidity of about .3. However if the solidity is lowered, the performance curve flattens out thereby making peak power to be delivered over a wide range of tip speed ratios. With the lower solidity power coefficient falls as well as operating range proceeds towards higher tip speed ratio side, so the turbine rotational speed increases yielding higher blade stresses. The figure 4.2 shows that with the higher solidity, the torque at low tip speed ratio increases which is good from the point of view of self-starting. But the disadvantage of using a high solidity turbine is that there is sharpe chage in power with the tip speed ratio as well

as peak power drops. It can be seen from the figure 4.3 that the turbine overall drag coefficient changes significantly with the solidity. At low solidity, the overall drag is lower. As a result, a low solidity turbine is better from the structural point of view.

According to the figure 4.1, with the increase of solidity, peak power coefficient moves towards the low tip speed ratio side. This is because of the fact that for a high solidity turbine, the induced velocities drop with tip speed ratio at a higher rate in comparison to that for a low solidity turbine. As a result, for a high solidity turbine, the local angles of attack change towards the lower values at a faster rate thus making the best angles of attack values (which give best lift values) to occur at lower tip speed ratio side. At low solidity, change of induced velocities and hence the local angles of attack with tip speed ratio happen slowly, so the optimum lift characteristics may appear over a wider range of tip speed ratio thereby making the nature of the curve flat near the peak value. While for a high solidity turbine since the change of local angles of attack with tip speed ratio occurs sharply; the best lift values appear for a very shorter range of tip speed ratio thereby making sharp change of power coefficient near the peak.

Theoretically production of power becomes maximum when the induced velocity ratio is $2/3$ (Betz limit) which may be termed as the optimum induced velocity. When at any station there occurs the coincidence of the optimum induced velocity with the lift close the stalling angle (optimum lift), it gives optimum

power. Actually the induced velocity is varying with azimuth angle, so the optimum condition is not satisfied at every station. However the solidity for which, in most of the stations the induced velocity and the angle of attack become either equal or near to the optimum induced velocity and optimum lift respectively, the peak power coefficient appears to be the highest. As the figure 4.1 reveals, it probably happens at solidity of about .3.

With the increase of solidity, the variation of the torque coefficient near the peak and the shifting of the peak torque coefficient towards the low tip speed ratio side (figure 4.2) may be explained in the same manner as in the case of power coefficients in the figure 4.1. For a high solidity turbine, solid blockage is higher (in other words the product of number of blades and chord is higher), as a result the tangential forces are higher which are the reasons of higher torque coefficients at low tip speed ratio. At low tip speed ratio the induced velocities and the local angles of attack distribution with azimuth angle remain almost unchanged with solidity, so they have very negligible effects on the variations of the torque coefficients with solidity at low tip speed ratio side.

Drag on a turbine is the axial force which may be considered to be equal to the rate of change of momentum in the axial direction. Thus for any particular turbine, this force is the function of induced velocity and the change of velocity (i.e. the difference of wind and wake velocities). With the rise of tip speed ratio, induced velocity drops and the change of velocity increases. But the product of induced velocity and change of velocity begin to

increase with tip speed ratio. As a result the drag and hence the drag coefficient increases with tip speed ratio and approaches unity when the wake velocity approaches zero. For a high solidity turbine fall of induced velocity as well as change of velocity occurs with tip speed ratio at a higher rate in comparison to that for a low solidity turbine. As a result drag coefficient for a high solidity turbine approaches to unity with tip speed ratio prior to that for a low solidity turbine.

Effect of Blade Pitching:

Performance characteristics of a straight-bladed Darrieus wind turbine with blade pitching have been presented in the figures 4.4, 4.5 and 4.6. In the present analysis pitching is said to be positive for the blade nose rotating in outward direction from the blade flight path. From the figure 4.4 it is observed that with the application of fixed pitching, the rotor power coefficient decreases especially after the peak value. The higher is the pitching, the lower is the power coefficient.

Incorporating fixed blade pitching (here it is positive), the angle of attack decreases in the upstream and increases in the downstream sides. So the blade airfoil lift coefficient drops in the upstream side and rises in the downstream side which are the outcome of the lower tangential force coefficients in the upstream side and higher tangential force coefficients in the downstream sides in general. But the increased angles of attack in the downstream side sometimes go beyond stalling angle which again are the

causes of reduced tangential force coefficients. However the net effect always reduces the power coefficients.

In the figure 4.5, the results are given for sinusoidal pitch variation. This figure shows that amplitude of angular pitch variation (sinusoidal) has significant effects on the performance curves. The figure 4.5 reveals that as the amplitude of sinusoidal pitch variation increases power rises with lower amplitude at the low tip speed ratio side. From the figure 4.4, it is seen that with the change of magnitude of fixed pitching, peak power remains in the higher tip speed ratio side while the figure 4.5 shows that with the change of amplitude of sinusoidal pitching, it gradually proceeds towards the lower tip speed ratio side.

As the sinusoidal pitching is incorporated into the turbine blade, the local angles of attack decreases in the upstream as well as in the downstream side in general. In the higher tip speed ratio range, these angles remain below the stalling angle. As a result with lower angles of attack, the lift coefficients become lower which are the results of lower tangential force coefficients. So the power coefficients fall with the rise of amplitude of sinusoidal blade pitching. With the rise of amplitude of sinusoidal pitching, the values of local angles of attack fall with tip speed ratio at a relatively higher rate which is the reason of shifting the peak power coefficient towards the lower tip speed ratio side. According to the figure 4.5, at low tip speed ratio range, the power coefficient increases with rise of amplitude of pitching. It is because, at zero pitching, angles of attack in many stations

are above stalling angle but employing sinusoidal pitching, (as a result of reduction of angle of attack) relatively lower number of stations occur in the stalling region. Incorporating the blade pitching, there appears relatively favourable local angles of attack distribution which makes favourable local tangential forces, as a result torque coefficients at the low tip speed ratio side increases with sinusoidal pitching.

From the figure 4.6 it is observed that the combination of fixed pitching and the sinusoidal pitching has remarkable effects on the performance curves. This figure reveals that as the combined pitching increases power rises with lower combined pitching at very low tip speed ratio side. From the figures 4.5 and 4.6; it is observed that of the high tip speed ratio side the power coefficients drop more for the combined blade pitching condition than those for the sinusoidal blade pitching condition. It is because of the fact that as the combined pitching is employed, the local angles of attack at the high tip speed ratio decreases more in the upstream side and increases more in the downstream side in comparison to those for sinusoidal pitching condition. For the combined pitching condition, lift values drops more in upstream side and exceeds stalling angle more rapidly than those for the sinusoidal blade pitching condition.

Effect of Number of Blades:

Figure 4.7 presents the variations of instantaneous torque with azimuth angle for various number of blades. The values are shown for one complete revolution of the rotor at an optimum tip

speed ratio. It is observed from this figure that number of blades has strong influence on the instantaneous torque of the rotor. The uniformity of the rotor speed depends on the amplitude of instantaneous torque variation or in other words, on the fluctuation of energy in one complete revolution. For one-bladed and two-bladed turbines these fluctuations are high, as a result in each revolution the turbine will rotate with relatively nonuniform speed. The fluctuations of energy for a three-bladed and a four-bladed turbine are low and since the rotor has self-inertia, so it will cause negligible variation in rotor speed. The torque variations of a two-bladed, a three-bladed and a four-bladed rotors can be obtained by superimposing respectively two torque curves; three torque curves and four torque curves for single blades. For a two-bladed, a three-bladed and a four-bladed turbines each curve is displaced by 180° , 120° and 90° respectively.

4.2 Comparative Results:

In the figures 4.8, 4.9 and 4.10 respectively, comparisons of the calculated values of overall power coefficients, torque coefficients and drag coefficients by the cascade theory both for the blades of cambered cross-section and symmetric cross-section are shown. From these figures, it is seen that the performance characteristics of the turbine with cambered blade cross-section improves negligibly in comparison to those of a turbine with symmetric blade cross-section. The figures 4.11, 4.12 and 4.13 shows the similar comparisons as the figures 4.8, 4.9 and 4.10 but it incorporates blade pitching. It is observed from these figures

that employing blade pitching there occurs small improvement of power coefficient in each of the cases.

In general for the blade airfoil of cambered cross-section, lift values increases in the upstream side and drop in the downstream side. As a result there occur higher torque in upstream side and lower torque in downstream side in comparison to those for the blade airfoil of symmetric cross-section. The net effect for the upstream and downstream sides change negligibly for the case with no blade pitching and for those with fixed, sinusoidal and combined blade pitching conditions.

In the figures 4.14 to 4.18 respectively, comparisons of the calculated values of the induced velocity ratios, local angles of attack, local Reynolds number, local non-dimensional tangential and normal forces by cascade theory with blades of cambered cross-section and symmetric cross-section, simple multiple streamtube theory are shown. The values are determined at tip speed ratio, 4.5. From the figure 4.14 it is seen that the induced velocity ratios by the cascade theory differ significantly from those by simple multiple streamtube theory. In the simple multiple streamtube theory it is assumed that the induced velocities in the upstream and the downstream sides of the rotor are constant. But in the cascade theory for the upstream and the downstream sides these are calculated separately. In the cascade theory, the drop of axial flow velocity occurs twice, one in the upstream side and

another in the downstream side. The wake velocity in the upstream side acts as the inlet velocity in the downstream side. As a result the induced velocities in the upstream side are higher than those in the downstream side which are depicted in the figure 5.14. From this figure it is also observed that the induced velocity ratios calculated by cascade theory for the blades of cambered cross-section varies negligibly in comparison with those calculated by cascade theory for the blades of symmetric cross-section. In the upstream side for blade airfoil of cambered cross-section the lift value increases, making the higher blade element drag force which is to be balanced by the higher drag produced due to the change of momentum occurs with the lower value of induced velocity while for the downstream side the opposite effect appears.

It may be observed from the figure 4.15 that the local angles of attack values by the cascade theory differ appreciably from those by simple multiple streamtube theory. But the local angles of attack values by the cascade theory for the blades of cambered cross-section differ in small amount from those by the cascade theory for the blades of symmetric cross-section. Figure 4.14 reveals that induced velocities in the upstream side fall for the cascade theory with blades of cambered cross-section than those for the cascade theory with blades of symmetric cross-section, which is the reason of relatively lower angles of attack in upstream side. Similarly angles of attack for downstream side may be explained.

The comparative curves of Reynolds number in the figure 4.16 show that there are negligible differences in Reynolds number by the cascade theory with blades of cambered cross-section and symmetric cross-section and simple multiple streamtube theory. For any particular turbine, Reynolds number is the function of the local relative flow velocity which is the vector sum of the tangential velocity and induced velocity. At high tip speed ratio, relative flow velocity is dominated mostly by the tangential velocity than the induced velocity. Since for the present case the tangential velocity is constant and the tip speed ratio is higher, so the only variations of the induced velocities (according to the figure 4.14) cannot make prominent change in Reynolds number by the theories mentioned above.

Referring to the figures 4.17 and 4.18 for the comparative curves of non-dimensional tangential and normal forces, one may observe that by cascade theory with blades of cambered cross-section and symmetric cross-section, the forces in the upstream side are higher than those in the downstream side while by the simple multiple streamtube theory, these forces are equal in both upstream and downstream sides. Figure 4.17 reveals that higher forces are produced in the upstream side than those in the downstream side. This can be explained easily following the figure 4.15 showing angle of attack distribution. These angles are below the stall point. So far higher angle there is higher lift, hence higher tangential force. Cascade theory with blades of cambered cross-section give more relatively higher blade lift value which is the

outcome of relatively higher local tangential force in the upstream side. Figure 4.18 having normal force distributions may be explained in the same manner as for the case of tangential force distribution in the figure 4.17.

Effect of Tip Speed Ratios:

Comparisons of the induced velocity ratios, local angles of attack, local Reynolds number, local non-dimensional tangential and normal forces at three tip speed ratios are shown in the figures 4.19 to 4.23 respectively. The local values are calculated by the cascade theory with blades of cambered cross-section and symmetric cross-section. Referring to the figure 4.19, it is observed that as the tip speed ratio increases induced velocity ratio decreases. With the rise of tip speed ratio, more and more air passes outside the rotor, hence the induced velocity begin to drop with tip speed ratio. At very high tip speed ratio almost all the air passes around the rotor thereby making the induced velocity very small. From this figure it is also seen that the induced velocity ratios calculated by cascade theory for blades of cambered cross-section varies negligibly in comparison with the induced velocity ratios for blades of symmetric cross-section. Figure 4.20 shows that at low tip speed ratio side there appear stalling angles in many stations. As the tip speed ratio increases the local angles of attack in all stations go below stalling point. With further rise of tip speed ratio local angles of attack fall more. This phenomenon can be explained from the induced velocity

distribution of the figure 4.19. Keeping the tangential velocity constant as the induced velocity decreases, values of local angles of attack decreases.

Figure 4.21 depicts that there is remarkable effect of tip speed ratio on the local Reynolds number. At constant turbine speed, tangential velocity is fixed, the wind velocity varies with tip speed ratio. At low tip speed ratio induced velocities are higher than those at high tip speed ratio (figure 4.19). As it is mentioned before for a particular turbine, local Reynolds number is the function of local relative flow velocity which is the vector sum of the tangential velocity and the induced velocity. At high tip speed ratio, Reynolds number is dominated mostly by tangential velocity and since this quantity is fixed there is relatively small variation of local Reynolds number with azimuth angle whereas at low tip speed ratio this variation is relatively higher because of higher influence of induced velocity in comparison to that at high tip speed ratio side. With blades of cambered cross-section the distribution of local Reynolds number varies negligibly from that with blades of symmetric cross-section.

It is seen from the figure 4.22 that at low tip speed ratio the local tangential forces drop in some range of azimuth angle which is due to the stalling effect as the figure 4.20 reveals. As the tip speed ratio rises stalling disappears. With very high tip speed ratio tangential forces decrease more because of lower local angles of attack. In the upstream side, local tangential forces calculated by the cascade theory for cambered blade cross-

section are slightly higher than those calculated by the cascade theory for symmetric blade cross-section. It occurs due to the fact that the local lift force in upstream side higher by cascade theory with cambered blade cross-section than those for symmetric blade cross-section. Similarly the figure 4.23 showing the non-dimensional local normal forces at different tip speed ratios can be explained.

CHAPTER 5 : DESIGN OF TURBINES

In this chapter simplified form of design method is presented for vertical-axis straight-bladed Darrieus wind turbine. The design is performed at variable turbine speed condition. A number of parameters such as solidity, design power, design wind speed, cutout speed, blade stress (in other words blade material), number of blades, airfoil shape, blade supporting type (simple/overhanged/cantilever) etc. control the design of turbines. Considering all the above mentioned variable parameters, the present design approach gives guidelines to have optimum turbine configurations at variable turbine speed.

Design of a vertical-axis Darrieus wind turbine at variable turbine speed condition is generally done with a view to serve the following purposes: (a) It may be applied to perform water pumping for irrigation (b) It may also be used in the DC generator/regulator/storage battery combination for generation of electricity in the remote areas. During designing the vertical-axis Darrieus wind turbine at variable turbine speed, there appear many variable parameters. Among them few parameters are considered to be fixed before conducting the design analysis. These are number of blades, blade material, blade supporting type and cutout speed. The flow diagram of the variable speed design approach has been given in the appendix-A. In this design, the blade pitching is considered as zero. Fixed blade pitching (either positive or negative) always gives reduced power. On the other hand, variable blade pitching may give improved power but control

of variable pitching is difficult especially at high turbine speeds. Number of blades is chosen as three but the other number may be taken as well. A turbine with three blades is better concerning smooth running because of lower fluctuations of energy in each revolution. In this design the blade material is chosen as aluminium alloy (where allowable stress is 100 N/sq. mm) and the cutout speed is considered as 14 m/sec. The blades are assumed to be supported like that of the overhanged type which is shown in figure 5.1.

In the present design analysis, the variable speed design is carried out at constant tip speed ratio. In other words, the load characteristic curve is assumed in such a way that the tip speed ratio remains constant. The constant tip speed ratio design may approximately follow the load characteristic curve of either a positive displacement pump or a centrifugal pump. However to make the accuracy of the design, actual pump characteristic curve is necessary to be encountered. In the present design method, emphasis is given on finding a general design approach of a variable speed turbine rather than to study a particular problem.

Design configurations of a variable speed turbine at various solidities are shown in the figure 5.1. The design wind speed is chosen as 8 m/ sec. while the design power is 10 Kw. It can be seen from this figure 5.1 that with the increase of solidity, the height and chord of the turbine increase appreciably while the turbine diameter decreases which is remarkable in the low solidity range only. It is also observed from this figure that with the rise of solidity, starting torque increases adequately. Starting

torque is important for the design of a variable speed wind turbine coupled with a pump. These starting torques are calculated at a wind speed of 4 m/sec. Obviously high solidity turbine is good in consideration of higher starting torque and lower diameter, on the other hand, low solidity turbine is good in consideration of lower height and chord. It has also been explained that a turbine with large diameter is not good because of additional losses due to additional drag produced by the blade supporting struts which are higher for a large diameter turbine. Blade skin thickness remains constant with solidity. Also the aspect ratio does not change much. The design power coefficients are higher in the middle range of solidity. The total length of struts and blades is minimum around solidity 0.500. At variable turbine speed condition, the design rpm should be as high as possible to reduce transmission losses. The figure 5.1 reveals that the peak values of rpm occur from solidity .300 to .600 but the variation of rpm with solidity is not much.

With the same number of blades, as the solidity (NC/R) of a turbine increases, the chord-radius ratio (C/R) increases which may be satisfied by reduced diameter and increased chord. The diameter is inversely proportional to the square root of the solidity of a turbine if the projected area and the aspect ratio remain constant. In this design these quantities do not vary considerably with solidity. Since the design power coefficient with solidity does not change much, for the production of the same power at the same wind speed, the projected area ($A = H.D$) of the turbine does not vary appreciably. As a result,

as the diameter decreases with solidity, the height increases. Since both height and chord increases with solidity, the aspect ratio (H/C) does not change much. For any fixed aspect ratio peak power coefficient is low at low solidity. It increases with the increase of solidity. With the further increases of solidity it decreases. Since in this design, the aspect ratio which has the influence on power coefficient, does not change much; the design power coefficient remain higher in the middle range of solidity. In this design torque is directly proportional to the diameter of the turbine and the planform area of the turbine blade. With the rise of turbine solidity, turbine diameter decreases while the planform area increases for the increase of blade chord and height. The combined effects increase the starting torque with rise of solidity.

Figures 5.2, 5.3 and 5.4 shows the comparisons of design configurations at various solidities for two types of blade supports: simple and overhanged type figure C.1. One may observe from the figure 5.2 that applying overhanged blade support in place of simple blade support, the diameter of the turbine and chord of the blade profile decrease remarkably while the height of the turbine only increases but at lower rate in comparison to diameter and chord. It may also be seen from the figure 5.2 that the aspect ratio for the overhanged blade support is more than double to that for the simple blade support. For overhanged blade support, aspect ratio is higher because of higher height of the turbine and lower chord of blade profile. From figure 5.3, it is observed that for the overhanged blade support, the design rpm and design power

coefficient increase appreciably from the corresponding value for simple blade support. It may also be seen from this figure that for the overhanged blade support the design tip speed ratio increases while the starting torque decreases in comparison to those for the simple blade support. Due to the higher aspect ratio for the overhanged blade support, the design power coefficient increases. For the overhanged blade support starting torque values decrease because of lower diameter of the turbine. Since the design tip speed ratio increases and diameter of the turbine decreases, hence for the same wind speed, design rpm for the overhanged blade support increases remarkably.

In this design the blade supporting struts is considered as of airfoil cross-section. It is observed that the struts having airfoil cross-section creates negligible drag i.e. the power loss due to supporting struts of airfoil cross-section become very negligible. The design is conducted based on supporting struts of airfoil cross-section. Total blade length L_B is the length of blade supporting struts and the turbine blades. From the figure 5.4 it may be seen that the total blade length in the case of overhanged blade support is lower in comparison to that for simple blade support. It is because of the fact that for the overhanged blade support, the diameter of the turbine decreases at higher rate while the height of the turbine increase at lower rate. It is obvious that the cost of production concerning blade supporting struts and turbine blades become lower in case of overhanged blade support in comparison to that for simple

blade support. Here from the economic point of view, the design for overhanged blade support is obviously better than that for the simple blade support.

Figure 5.5 shows the power coefficient distribution with tip speed ratio while figures 5.6 and 5.7 give respectively the distribution of overall torque and power with rpm of turbine at various wind speeds. The solidity is kept fixed at 0.500 while design power is 10 Kw. One may observe from the figure 5.5 that the design power coefficient has been chosen in the higher tip speed ratio side from that corresponding to the peak power coefficient. With a view to make the operation stable and smooth, design point is selected in such a way. In the reference [10], Blackwell et al also suggest to consider the design point accordingly for variable speed operation. In the figure 5.5 before the peak value of power coefficient, there are some differences in the power coefficients at various wind speeds. These are due to the Reynolds number effects. After the peak power coefficient these differences are small because the Reynolds numbers become very high in this region and in the higher range of Reynolds number the effects of them are small. In the figures 5.6 and 5.7, system load characteristic curves are shown. These figures also show that with the change of wind speed, both the torque and power of turbine change adequately. One can observe from these figures 5.6 and 5.7 that the maximum rpm corresponding to the cutout speed is remarkably higher than the design rpm. The figures 5.6 and 5.7 show that the torque and power increases remarkably with

the wind speed. For the same turbine configuration and constant design tip speed ratio, having power coefficients nearly same (which is clear from figure 5.5), the torque and power are respectively proportional to the square and cube of wind speed.

The variations of blade mass and the maximum blade stress with blade skin thickness are shown in the figure 5.8. One may observe from this figure that with the increase of blade skin thickness blade mass increases almost linearly while the maximum blade stress decreases in the lower range of skin thickness and increase in the higher range. It happens because of the fact that with the increase of blade skin thickness, the area moment of inertia improves in comparison to blade mass in the lower range of skin thickness while in the higher range the reverse effect occurs. The skin thickness which corresponds to the lowest value of maximum blade stresses, is the best thickness and is chosen as the design skin thickness of the blade airfoil.

Figure 5.9 presents the distributions of normal, centrifugal and net normal forces with azimuth angle. The forces corresponding to the design and cutout speeds have been shown in this figure. The net normal forces corresponding to the cutout speed are remarkably higher in comparison to those at the design wind speed. This happens mainly for the high rpm corresponding to the cutout speed and it creates tremendous centrifugal force. This figure also shows that the normal forces (aerodynamic) are almost negligible in comparison to the centrifugal forces.

At the design and the cutout speeds, the variations of bending moments with azimuth angle are presented in the figures 5.10 and 5.11 while variations of bending stresses with azimuth angle are given in the figures 5.12 and 5.13. The figure 5.10 shows the bending moments due to the net normal forces while the figure 5.11 shows the bending moments due to the tangential forces. It is seen from these figures that the bending moments at the cutout speed are remarkably higher than those at the design wind speed. These are because of higher net normal forces corresponding to the cutout speed. It can also be observed from these figures that the bending moments due to tangential forces are almost negligible compared to those due to the net normal forces. The figures 5.12 and 5.13 can be explained in the same way as in the case of bending moments. The figures 5.12 and 5.13 show that bending stresses due to the tangential forces are negligible in comparison to those due to the net normal forces. As a result the design stress analysis is performed based on the stresses due to the net normal forces only. The derivation techniques of bending moment and bending stresses are given in the appendix-C.

There appears the starting problem for the variable speed design where the wind turbine is directly coupled with a pump. The starting can be done in many ways. One possible way of starting may be achieved by employing variable pitching. The figure 5.14 shows that with the variable pitching the starting torque increases significantly. Fixed pitching makes very negligible

change in the starting torque. Application of variable pitching in the low tip speed ratio range of operation can also provide with nearly constant torque; so employing variable pitching, once starting occurs, there appears no problem of stalling with the rise of tip speed ratio. Figures 5.15 shows that the starting torque can be increased remarkably by increasing wind speed. It indicates that the region having high wind speeds has relatively less starting problem. For any particular turbine starting torque is proportional to the square of the wind velocity.

Figures 5.16, 5.17 and 5.18 respectively show the variations of blade mass, centroidal area moment of inertia about \bar{x} -axis and that about \bar{y} -axis with blade skin thickness. It is observed from the figures 5.16 and 5.17 that with the increase of skin thickness in the lower range, the area moment of inertia improves in comparison to the blade mass while in the higher range it gives the reverse effect. It may be noted here that for the same blade skin thickness, with the rise of blade chord, area moment of inertia increases in proportion to C^4 while blade mass increases in proportion to C^2 . It indicates that increasing blade chord, blade structure can be improved remarkably. The form of blade airfoil cross-section applied in the present design is shown in the appendix-B. This appendix also presents the derivation techniques of the blade cross-sectional area and area moment of inertia.

CHAPTER 6 : CONCLUSIONS AND RECOMMENDATIONS

In this chapter general conclusions are drawn regarding the performance with cascade theory applying blades of cambered cross-section and the design method of a straight-bladed Darrieus wind turbine with blade support of overhanged type. Few recommendations are also given for the future works.

6.1 Conclusions:

Cascade Theory:

- 1) The performance of a vertical-axis straight-bladed Darrieus wind turbine with cambered blade cross-section improves negligibly in comparison to that of a Darrieus wind turbine with symmetric blade cross-section.
- 2) Due to the non-availability of experimental results for the vertical-axis straight-bladed Darrieus wind turbine with cambered blade cross-section, correlation could not be made. It is expected that the calculated results by cascade theory with cambered blade cross-section would give reasonable correlation with experimental results.
- 3) Performance analysis has been done with cascade theory mainly because the momentum theory cannot give reasonable performance prediction at higher tip speed ratios and at higher solidities.

4) Employing the cambered blade profile in place of symmetric blade profile, the local values of power increase in the upstream and decrease in the downstream sides in general.

Design of Turbines:

- 1) Employing cambered blade profile in place of symmetric blade profile there appears negligible improvement of performance of a Darrieus turbine in addition application of blade with cambered section incurs higher cost of production, as a result design is performed with blade of symmetric cross-section.
- 2) In the present design method, design point is chosen in the higher tip-speed ratio side from that corresponding to the peak power coefficient. Because the region after the peak power coefficient is relatively stable and suitable for smooth operation. For a high solidity turbine, the power coefficient curve near the peak is not flat, as a result design with peak power coefficient is not good because with a slight shifting of tip speed ratio towards the lower value, there may appear stalling in some of the stations. For normal running it is avoided.
- 3) The variable speed turbine design is carried out at constant tip speed ratio. The constant tip speed ratio design may approximately follow the load characteristics curve of either a positive displacement pump or a centrifugal pump. However to make the accuracy of the design, actual pump characteristic curve is necessary to be encountered. The present design analysis gives a general design approach rather than to find a solution for a particular problem.

4) In the present design, the blade pitching is considered as zero for normal running. Fixed blade pitching (either positive or negative) always gives reduced power. On the other hand, variable blade pitching may give higher power but control of variable pitching is difficult especially at high turbine speeds.

5) The design is done at the cutout speed of 14 m/sec. obviously higher cutout speed makes higher blade stress. For the overhanged blade support cutout speed may be increased, still it does not create much problem concerning the blade stress like that which appear for the simple blade support.

6) Aspect ratio of a straight-bladed Darrieus wind turbine plays vital role in the design analysis. It controls the blade maximum stress. If the stress developed on the turbine blade is more than the allowable stress, aspect ratio is lowered in order to reduce the blade stress. With the change of aspect ratio, the turbine design configurations are also changed.

7) Blade skin thickness is also important in the design analysis. Increasing skin thickness the blade moment of inertia increases, on the other hand the centrifugal force rises due to higher blade mass, as a result a compromise is made to obtain the optimum skin thickness.

8) In the present design few parameters are assumed to be fixed for the analysis. These are blade material, number of blades, cutout speed. The design configurations will be changed with the variations of these parameters.

9) For a Darrieus turbine with one or two blades, the amplitude of instantaneous torque variation or fluctuations of energy in one revolution are relatively higher than those for a turbine with three or four blades which give relatively more uniformity in rotor speed. So the present design is carried out with three blades.

6.2 Recommendations for Further Researches:

Concerning the research work few recommendations are presented in this section.

- 1) Performance prediction with blades of cambered cross-section employing proper blade pitching has not been studied in detail in the present analysis. It is believed that if the blades of cambered cross-section with proper blade pitching are incorporated the turbine performance may improve appreciably.
- 2) Blade pitching moment has not been considered in the calculation. At high tip speed ratio there is no such effect while at low tip speed ratio it may not be neglected. Pitching moment may be applied in the calculation to see the effect on the performance characteristics.
- 3) During designing the turbine with straight-blade, the blades are assumed to be supported like that of overhanged type. It may be repeated with other type of support like cantilever for comparative study.

4) Design of a straight-bladed Darrieus turbine has been done with the aluminium blade. The same design may be performed for the overhanged blade support applying wood with skins of aluminium as a blade material which is available in our country.

5) Natural frequency of wind turbine rotation has not been determined in the present work. However it is important, it can be taken into account as well.

6) In the present design work, airfoil NACA 0015 is chosen for the turbine blade. It may be carried out with other types of airfoil such as NACA 0012 and NACA 0018 for the comparative study. In the design the number of blades is considered as three. The design may be conducted with other number as well for the comparative study.

7) In the design the blade stress analysis is done corresponding to the cutout speed of 14.0 m/sec. This design may also be repeated at higher value of cutout speed for comparative study.

REFERENCES

- [1] ABBOTT, I.H. and VON DOENHOFF, A.E., "Theory of Wing Sections", Dover publications, Inc., New York 1959.
- [2] AMOS, G.W. and BRAGG, G.M., "A Comparison of Analytical Prediction Methods for Vertical Axis Wind Turbines", Proceedings of the 1st European Wind Energy Conference, Hamburg, Oct. 22-26, 1984, pp. G5 - 394 - 399.
- [3] ASHLEY, H., "Some Contribution to Aerodynamic Theory for Vertical Axis Wind Turbine", Proceedings of the Twelfth Intersociety Energy Conversion Engineering Conference, Washington, D.C., August 28-Sept. 2, 1977, pp. 1624-1632.
- [4] BANNISTER, W.S., "Aerodynamic Studies of a Straight-Bladed Vertical-Axis Wind Turbine", Proceedings of the 1st British Wind Energy Association Workshop, April 1979, pp. 88 - 101.
- [5] BEURSKENS, H.J.M, HAGEMAN, A.J.F.K., HOSPERS, G.D., KRAGTEN, A. and LYSEN, E.H., " Low Speed Water Pumping Windmills : Rotor Tests and Overall performance", Proceedings of the Third International Symposium on Wind Energy Systems, Denmark, August 26 - 29, 1980, pp. K2 - 501 - 520.
- [6] BLACKWELL, B.F. and REIS, G.E., "Blade Shape for a Troposkien Type of a Vertical Axis Wind Turbine", Sandia Laboratories Report, SLA74-0154, April 1974.

- [7] BRAASCH, R.H., "Vertical - Axis Wind Turbine Program", Proceedings of the Vertical - Axis Wind Turbine Technology Workshop, Sandia Laboratories, SAND76 - 5586, May 17-20, 1976, pp. I-33-34.
- [8] BRAASCH, R.H., "The Design, Construction, Testing and Manufacturing of Vertical - Axis Wind Turbines", Proceedings of the Second International Symposium on Wind Energy Systems, Oct. 3-6, 1978, pp. E3-23-88. †
- [9] CLANCY, J., "Aerodynamics", A Pitman International Text, 2nd Edition, 1978.
- [10] CLARK, R.N., NELSON, V. and BARIEAU, R.E., "Wind Turbines for Irrigation Pumping", AIAA/SERT Wind Energy Conference, Colorado, April 9 - 11, 1980, pp. 163 - 169.
- [11] CURRIE, I.G., "Fundamental Mechanics of Fluids", McGraw Hill, 1974.
- [12] DEWILDE, L., HIRSCH, Ch., Six, D. and AERSCHOT, D.V., "Assessment of Wind Energy Potential in Belgium and Luxemburg", Dienst Stromings mechanica, Vrije Universiteit Brussel, October, 1984.
- [13] DOMMASCH, D.O., "Airplane Aerodynamics", Pitman Aeronautical Publications, 3rd Edition, 1961.
- [14] DURAND, W.F., "Aerodynamic Theory", Peter Smith, 1976.
- [15] FANUCCI, J.B. and WALTERS, R.E., "Innovative Wind Machines: The Theoretical Performance of a Vertical Axis Wind Turbine", Proceeding of the Vertical - Axis Wind Turbine Technology Workshops, Sandia Laboratories, SAND76-55, May 1976, pp. III-61-95.

- [16] GOEZINNE, F. and EILERING, F., "Water Pumping Windmills with Electrical Transmission", Wind Engineering, Vol. 8, No. 3, 1984, pp. 152 - 159.
- [17] GOLDING, E.W., "The Generation of Electricity by Wind Power", E. & F. N. Spon Ltd., London, 1955.
- [18] GRYLIS, W., DALE, B. and SARRE, P.E., " A Theoretical and Experimental Investigation into the Variable Pitch Vertical Axis Wind Turbine", Proceedings of the Second International Symposium on Wind Energy Systems, Amsterdam, Oct. 3 - 6, 1978, pp. E9 - 101 - 118.
- [19] HAGEN, L.J. and SHARIF, M., " Design and Field Testing of a Variable - Speed VAWT System for Low-Lift Irrigation Pumping", Proceedings of the Wind Energy Application in Agriculture, Iowa, May 15-17, 1979, pp. 87-103.
- [20] HOLME, O., " A Contribution to the Aerodynamic Theory of the Vertical Axis Wind Turbine", Proceedings of the International Symposium on Wind Energy Systems, Cambridge, September 1976, pp. C4-55-72.
- [21] HUNT, V.D., "Wind Power", Van Nostrand Reinhold Company, New York, 1981.
- [22] LARSEN, H.C., " Summary of a Vortex Theory for the Cyclogiro", Proceedings of the Second U.S. National Conferences on Wind Engineering Research, Colorado State University, June 1975, pp. V-8-1-3.
- [23] LYSEN, E.H., " Introduction to Wind Energy", SWD Publication, Netherlands, May 1983.

- [24] MAYS, I.D., MUSGROVE, P.J., "Performance of the Variable Geometry Vertical Axis Wind Turbine at High and Low Solidities", Proceedings of the 1st Wind Energy Association Workshop, April 1979, pp. 48-56.
- [25] MANDAL, A.C. "Aerodynamics and Design Analysis of Vertical Axis Darrieus Wind Turbines" Ph. D. Thesis, Jan. 1986.
- [26] MIGLIORE, P.G. and WOLFE, W.P., "The Effects of Flow Curvature on the Aerodynamics of Darrieus Wind Turbines", Dept. of Aerospace Engineering, WVU, Morgantown, July 1980.
- [27] MILNE THOMSON, L.M., "Theoretical Aerodynamics", Dover Publications, Inc., New York, 4th Edition, 1973.
- [28] MUSGROVE, P.J., "The Variable Geometry Vertical - Axis Windmill", Proceedings of the International Symposium on Wind Energy System, Cambridge, Sept. 7-9, 1976, pp. C7-87-100.
- [29] MUSGROVE, P.J. and MAYS, I.D., "Development of the Variable Geometry Vertical ∞ Axis Windmill", Proceedings of the Second International Symposium on Wind Energy System, Amsterdam, October, 3-6, 1978, pp. E4-39-60.
- [30] NATTUVETTY, V. and GUNKEL, W.W., "Theoretical Performance of a Straight ∞ Bladed Cycloturbine Under Four Different Operating Conditions", Wind Engineering, Vol.6, No. 3, 1982, pp. 110-130.
- [31] NOLL, R.B. and HAM, N.D., "Analytical Evaluation of the Aerodynamic Performance of a High-Reliability Vertical-Axis Wind Turbine", Proceedings of AWEA National Conference, 1980.

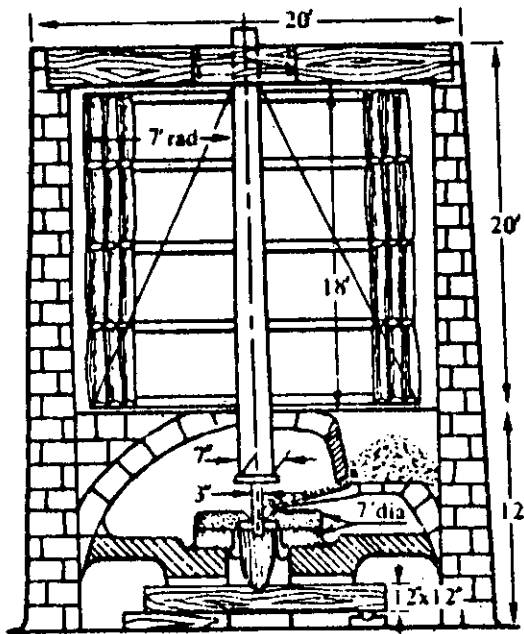
- [32] RANGI, R.S., SOUTH, P. and TEMPLIN, R.J., " Wind Power and the Vertical-Axis Wind Turbine Developed at the National Research Council of Canada", National Aeronautical Establishment/National Research Council of Canada, Reprint of Article from DOE/NAE Quarterly Bulletin No. 1974(2).
- [33] READ, S. and SHARPE, D.J., "An Extended Multiple Streamtube Theory for Vertical Axis Wind Turbines", Proceedings of the Second British Wind Energy Association Workshop, Cranfield, April 1980.
- [34] RIEGELS, F.W., " Airfoil Sections", Butterworths, 1961.
- [35] SEKI, K., SHIMIZU, Y. and MATSUMOTO, T., " A Study of Straight Blade VAWT and its Application", Proceedings of the 1st European Wind Energy Conference, Hamburg, Oct. 22-26, 1984, pp. G14-436-442.
- [36] SHANKAR, P.N., " On the Aerodynamic Performance of a Class of Vertical Shaft Windmills", Proceedings of the Royal Society of London, Series A, Vol. 349, 1976, pp. 35 - 51.
- [37] SHARPE, D.J., " A Theoretical and Experimental Study of the Darrieus Vertical Axis Wind Turbines", School of Mechanical, Aeronautical & Production Engineering, Kingston Polytechnic, Research Report, Oct. 1977.
- [38] SHARPE, D.J., " A Vortex Flow Model for the Vertical Axis Wind Turbine", Proceedings of the 1st British Wind Energy Association Workshop, April 1979, pp. 125-133.
- [39] SIMHAN, K., " A Review of Calculation Methods for the Determination of Performance Characteristics of Vertical

Axis Wind Energy Converters with Special Reference to the Influence of Solidity and Starting Characteristics", Proceedings of the 1st European Wind Energy Conference, Hamburg, Oct. 22-26, 1984, pp. E14 - 324 - 332.

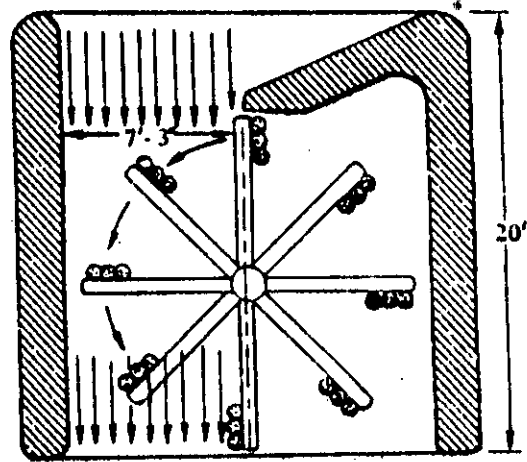
- [40] STRICKLAND, J.H., " The Darrieus Turbine : A Performance Prediction Model Using Multiple Streamtubes", Sandia Laboratories Report, SAND75-0431, Oct. 1975.
- [41] STRICKLAND, J.H., WEBSTER, B.T. and NGUYEN, T., " A Vortex Model of the Darrieus Turbine : An Analytical and Experimental Study", Journal of Fluids Engineering, Vol. 101, No. 4, Dec. 1979, pp. 500 - 505.
- [42] TEMPLIN, R.J., " Aerodynamic Performance Theory for the NRC Vertical-Axis Wind Turbine", National Research Council of Canada, Report LTR -LA-160, June 1974.
- [43] WALTERS, R.E., FANUCCI, J.B., HILL, P.W. and MIGLIORE, P.G., " Vertical Axis Wind Turbine Development", Dept. of Aerospace Engineering, WVU, Morgantown, July 1979.
- [44] WALTERS, R.E., MIGLIORE, P.G. and WOLFE, W.P., " Vertical Axis Wind Turbine Research at West Virginia University", SERI Second Wind Energy Innovative Systems Conference, Colorado, Dec. 3-5, 1980, pp. 159-178.
- [45] WILSON, R.E., " Aerodynamics of the Darrieus Rotor", Proceedings of the Vertical-Axis Wind Turbine Technology Workshop, Sandia Laboratories, May 17-20, 1976, pp. III-1-22.
- [46] WILSON, R.E. and LISSAMAN, P.B.S., " Applied Aerodynamics of Wind Power Machines", Oregon State University, May 1974.

- [47] ZERVOS, A., DESSIPRIS, S. and ATHANASSIADIS, N. " Optimization of the Performance of the Variable Pitch Vertical Axis Wind Turbine", Proceedings of the 1st European Wind Energy Conference, Humburg, Oct., 22 - 26, 1984, pp. G8-411 - 416.,

FIGURES



view on vertical section



view on horizontal section

Figure 2.1 : Persian windmill of vertical-axis type.



Figure 2.2: Horizontal axis wind turbine for pumping water.

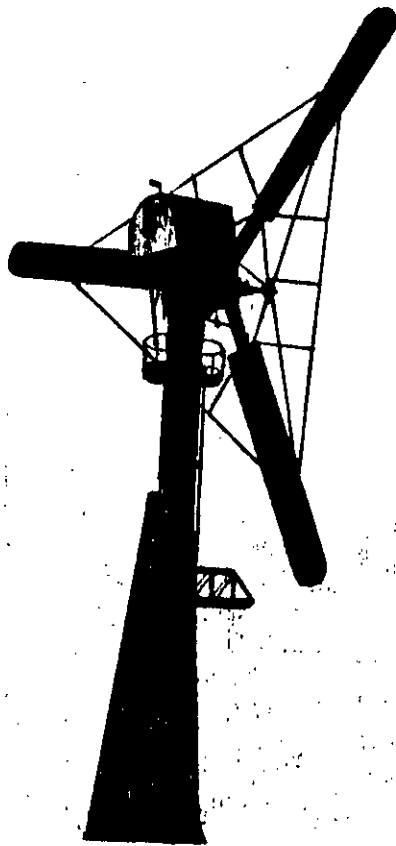


Figure 2.3: Restored Danish Gedser wind turbine.

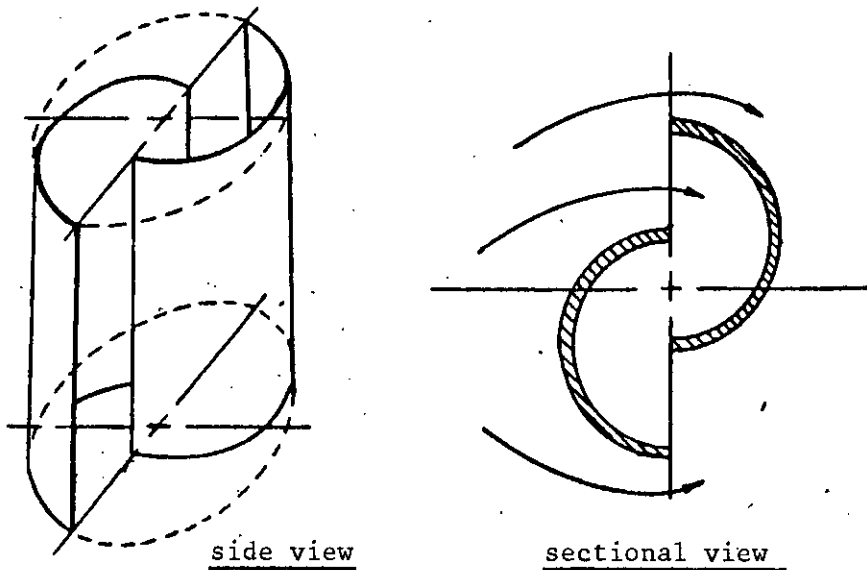


Figure 2.4 : Savonius rotor.

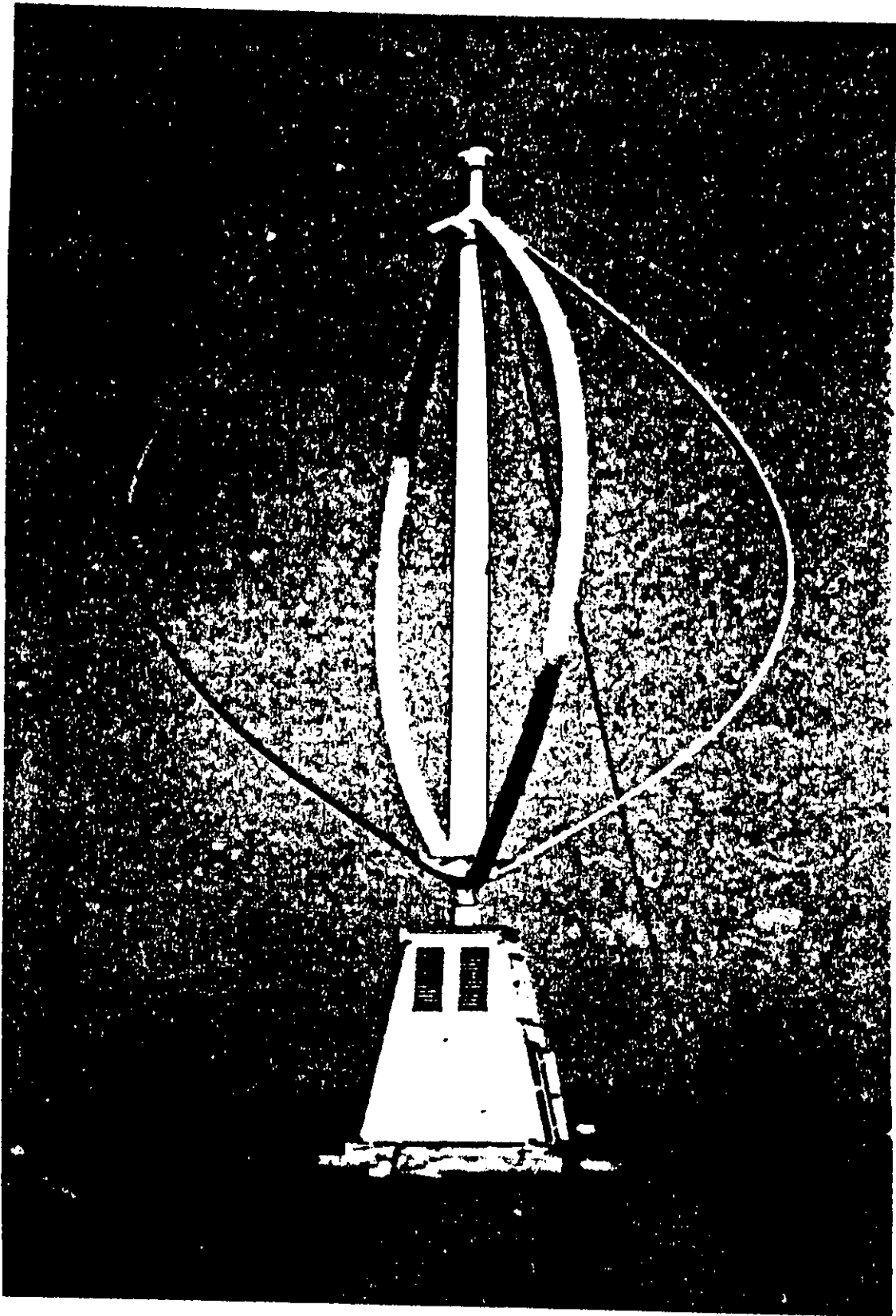


Figure 2.5 : Vertical-axis curved-bladed Darrieus wind turbine.

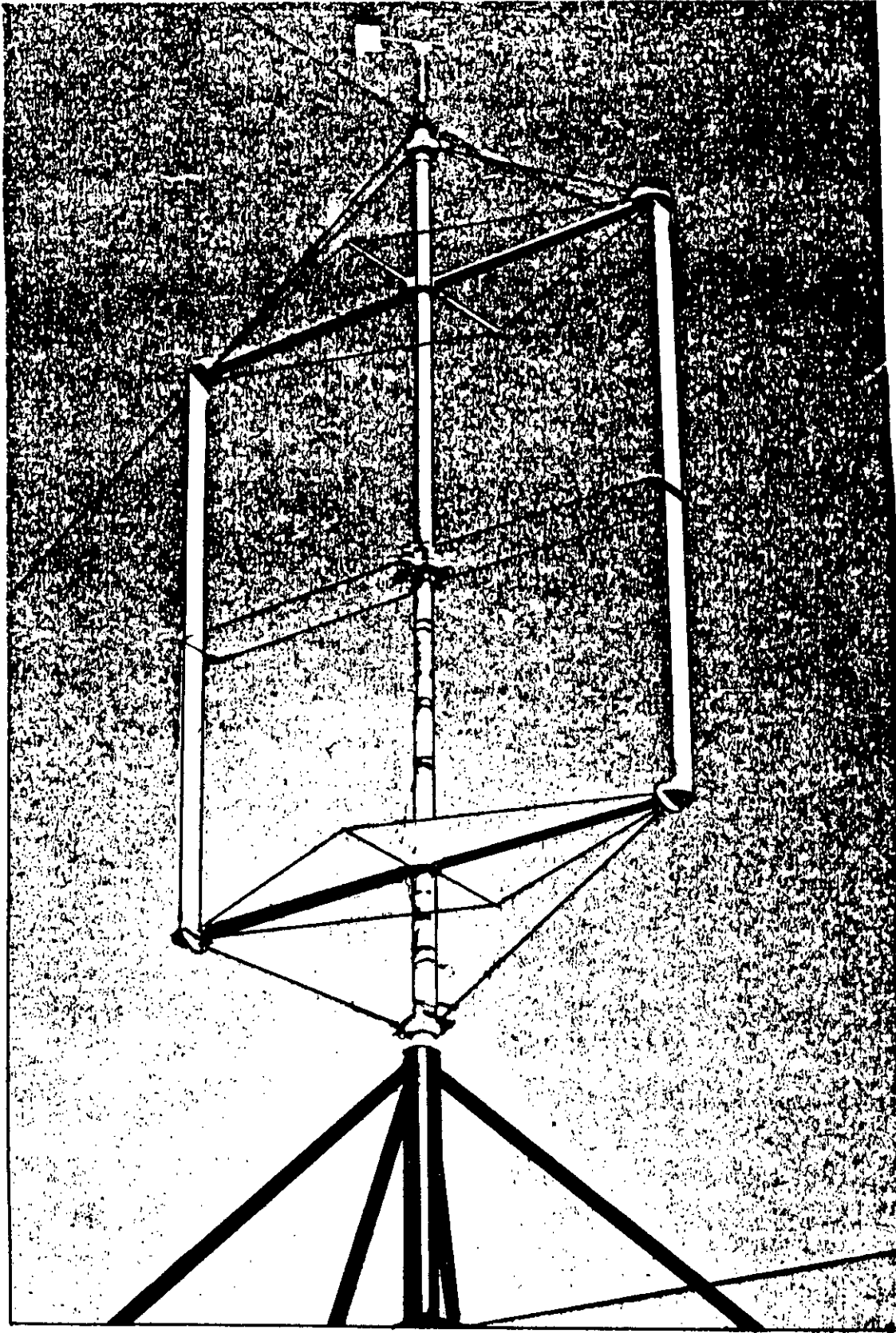


Figure 2.6 : Vertical-axis straight-bladed Darrieus wind turbine.

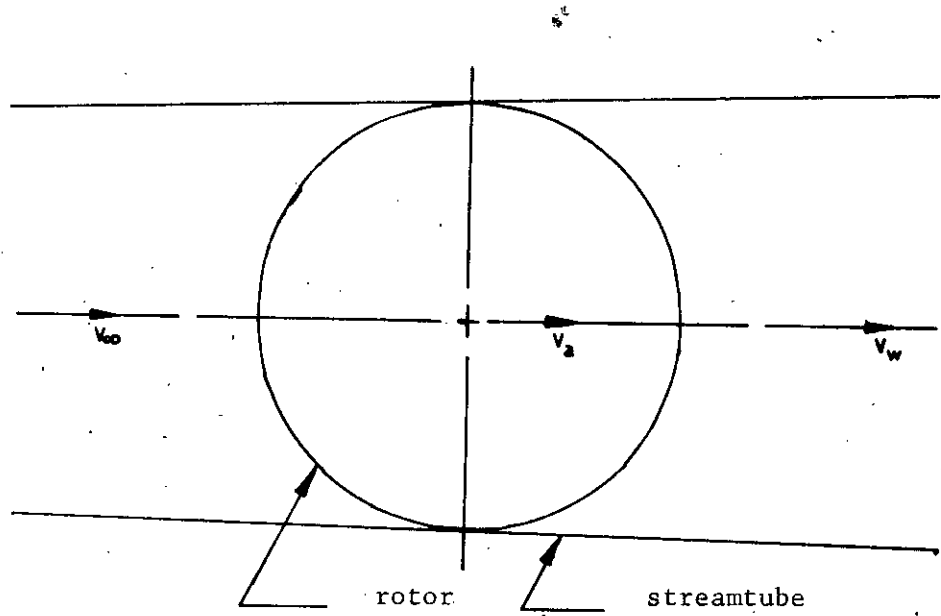


Figure 3.1 : Streamtube consisting of the rotor showing the axial flow velocities.

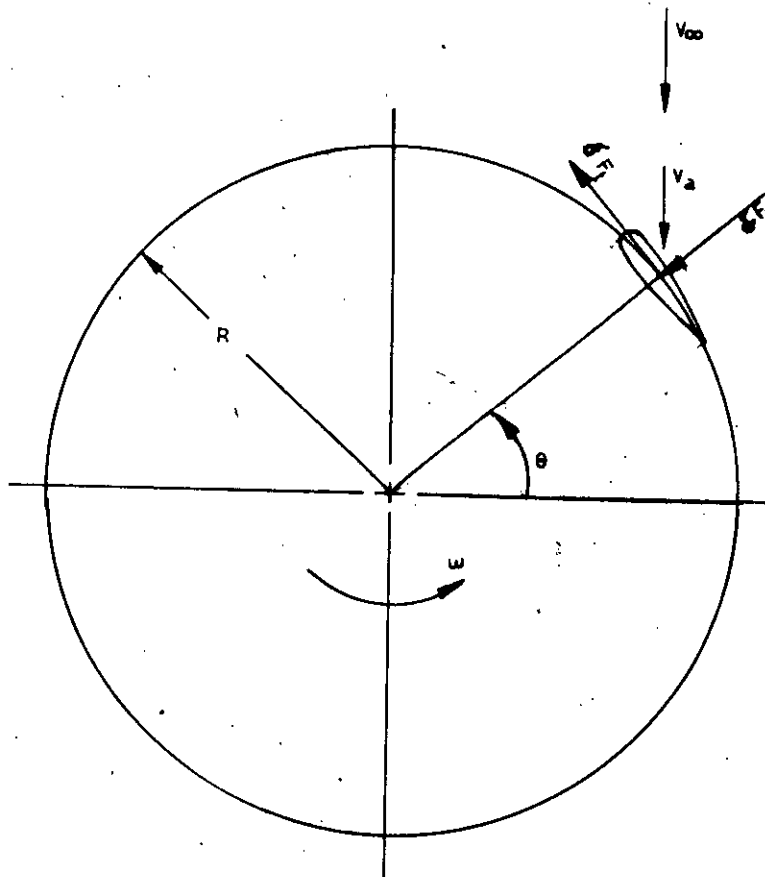


Figure 3.2: Aerodynamic forces on a blade element of a Darrieus rotor.

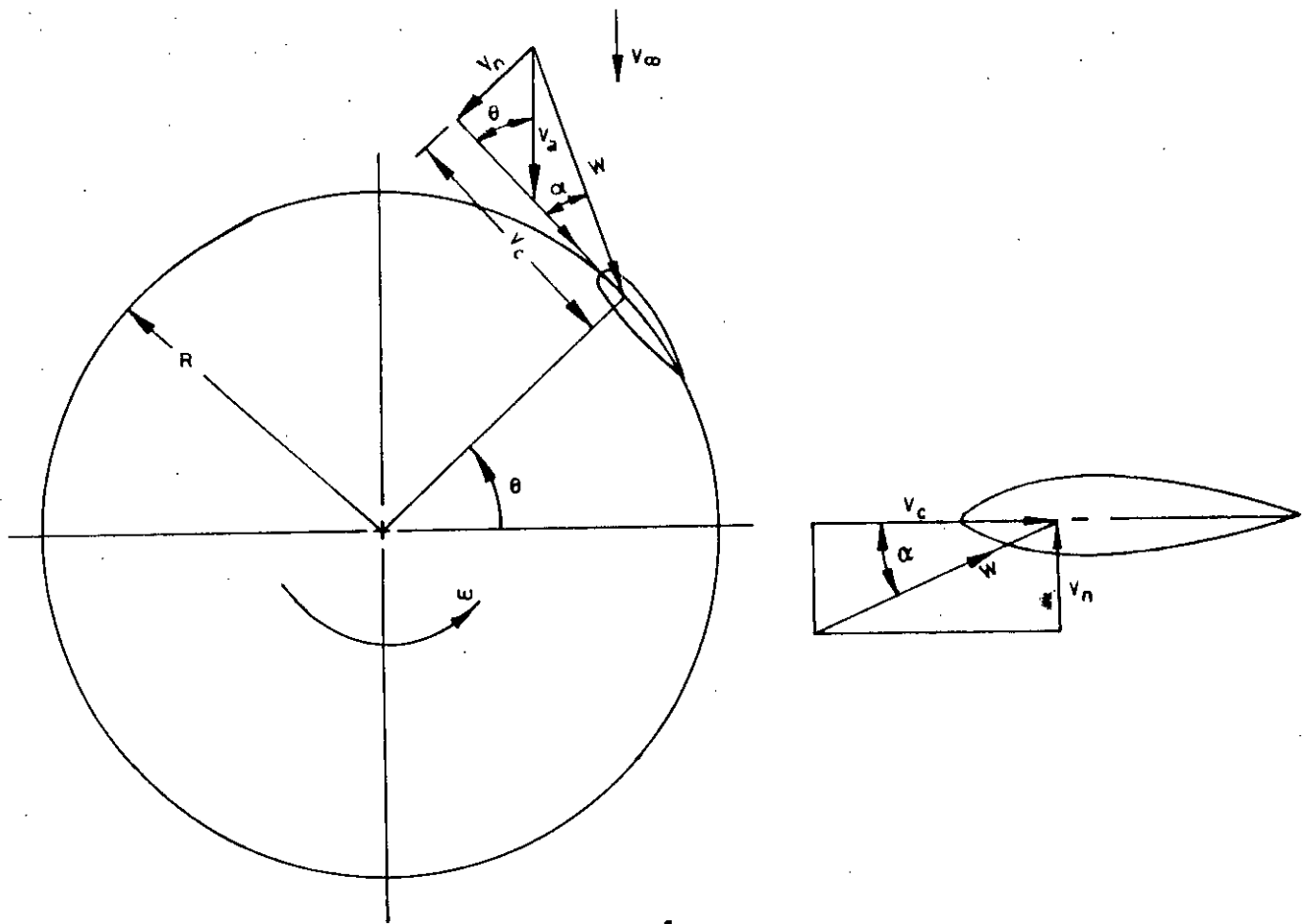


Figure 3.3: Velocity diagram on the blade element of straight-bladed Darrieus wind turbine.

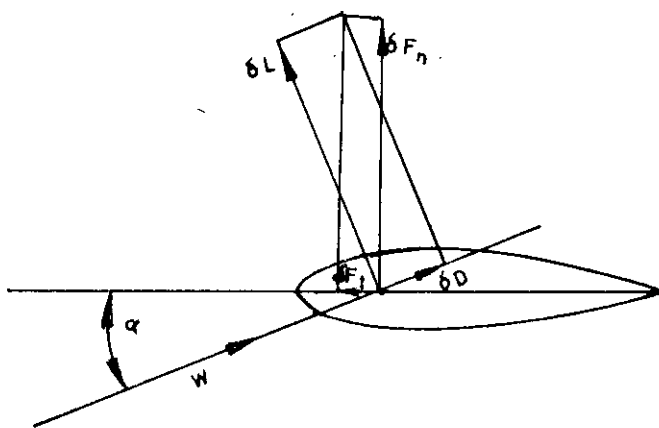


Figure 3.4: Aerodynamic forces acting on an airfoil.

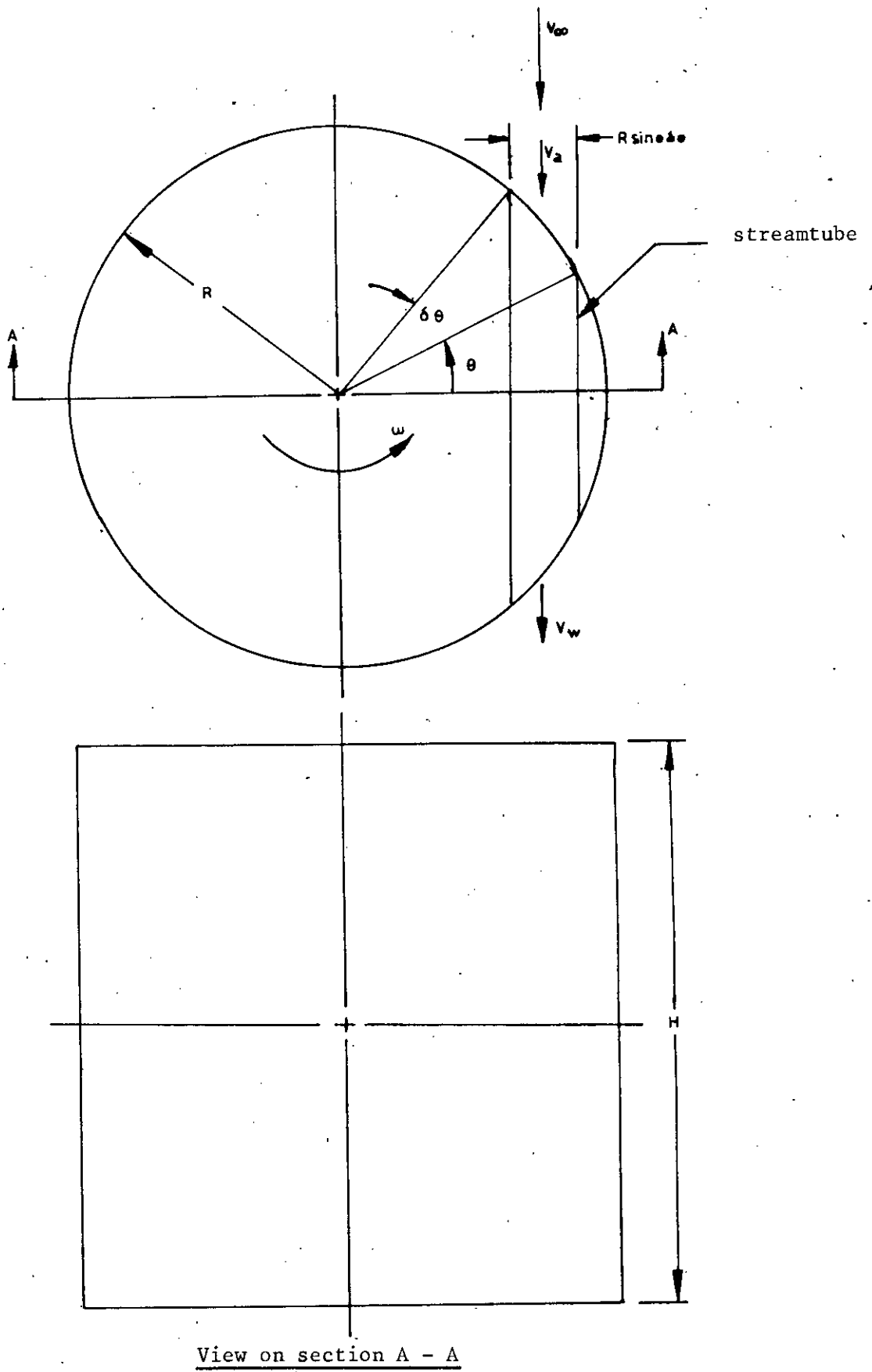


Figure 3.5 : Cross-sectional area of an elemental streamtube of a straight-bladed Darrieus wind turbine.

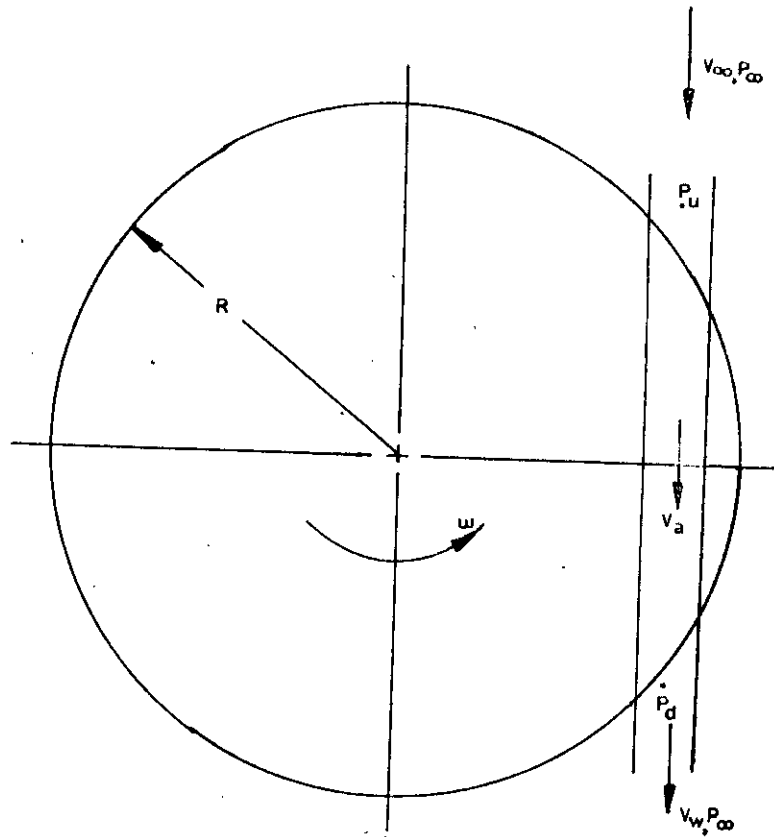


Figure 3.6: Pressures and velocities along the streamtube

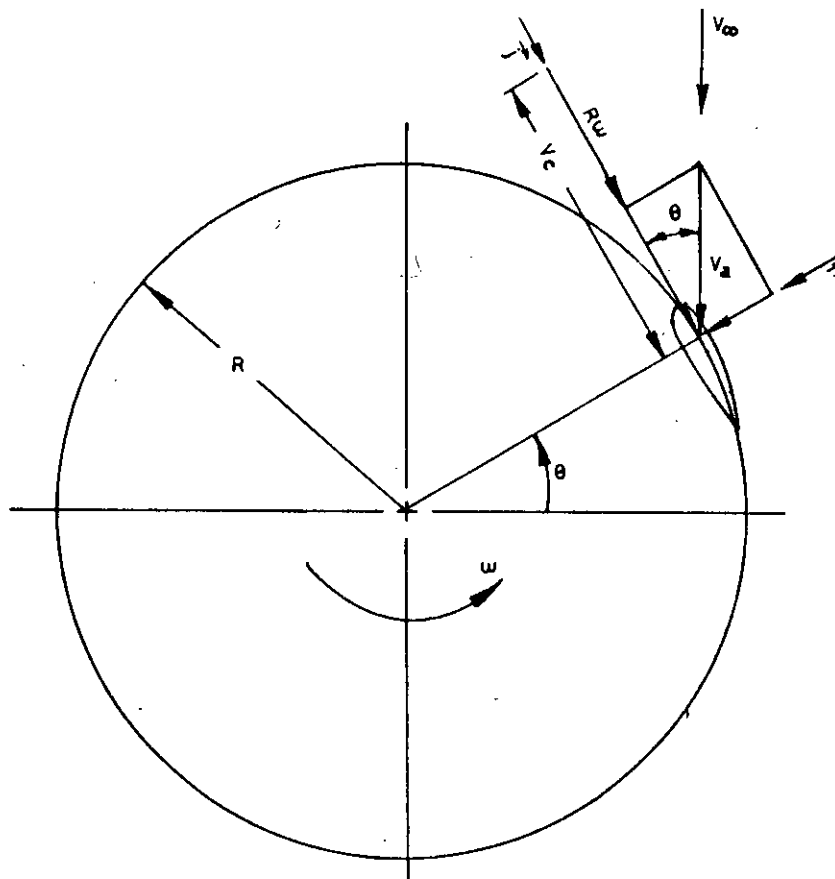


Figure 3.7: Velocity diagram on the blade element of a straight-bladed Darrieus wind turbine.

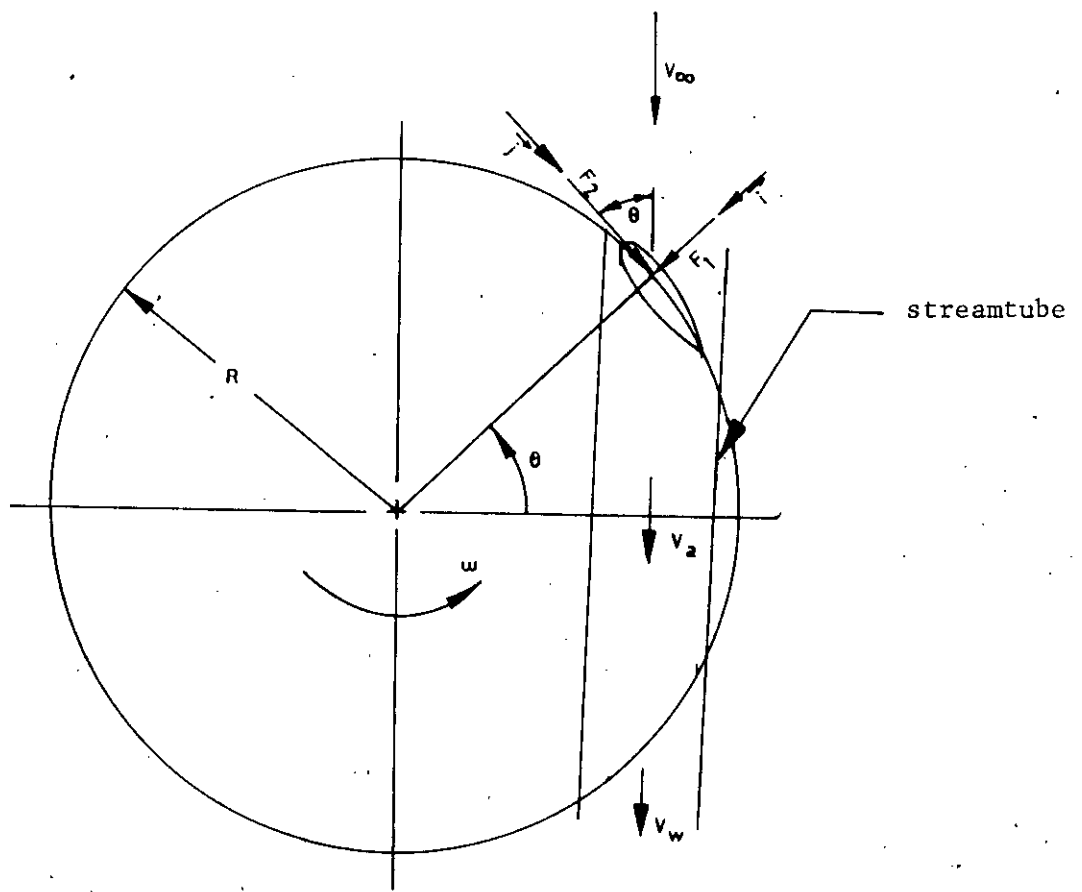


Figure 3.8 : Force diagram on the blade element of a straight-bladed Darrieus wind turbine.

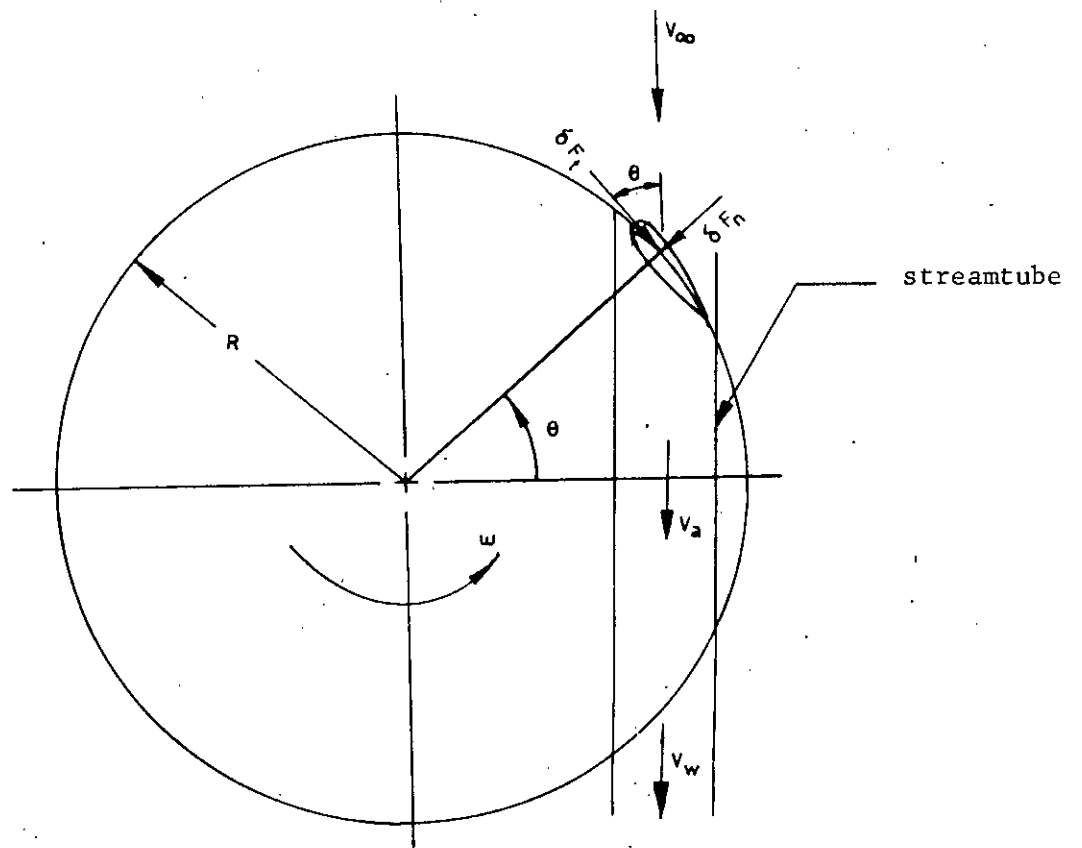


Figure 3.9 : Elemental blade forces of a straight-bladed Darrieus wind turbine.

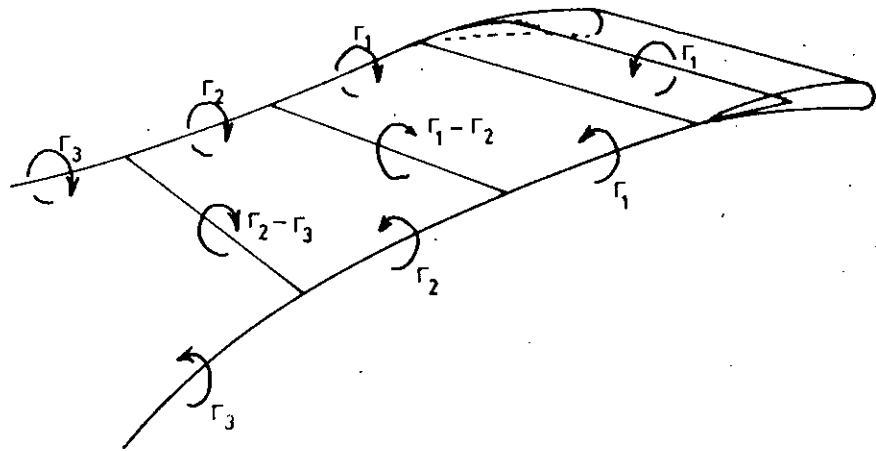


Figure 3.10 : Vortex system for a single blade element.

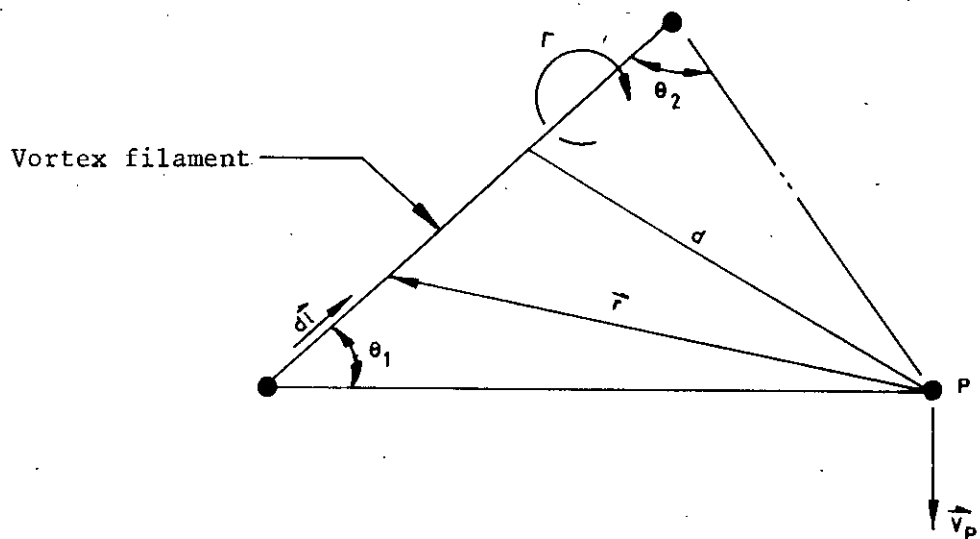


Figure 3.11 : Velocity induced at a point by a vortex filament.

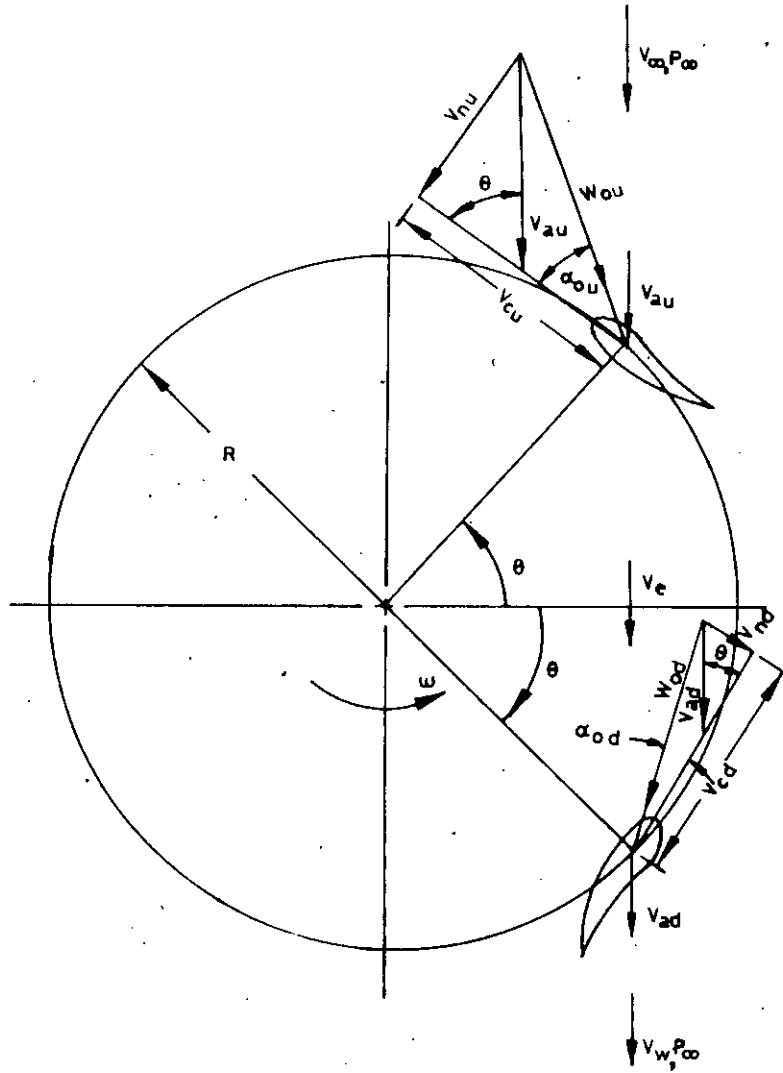


Figure 3.12 : Horizontal section of a straight-bladed (cambered-bladed cross-section) Darrieus wind turbine with flow velocities.

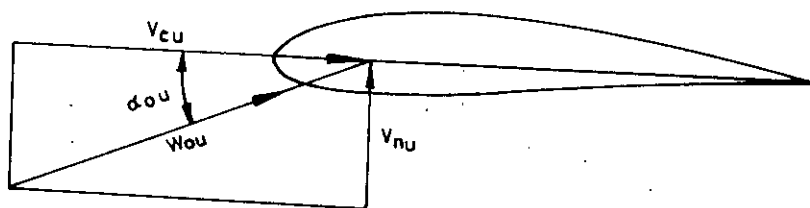


Figure 3.13 : Relative flow velocities on a cambered-blade airfoil.

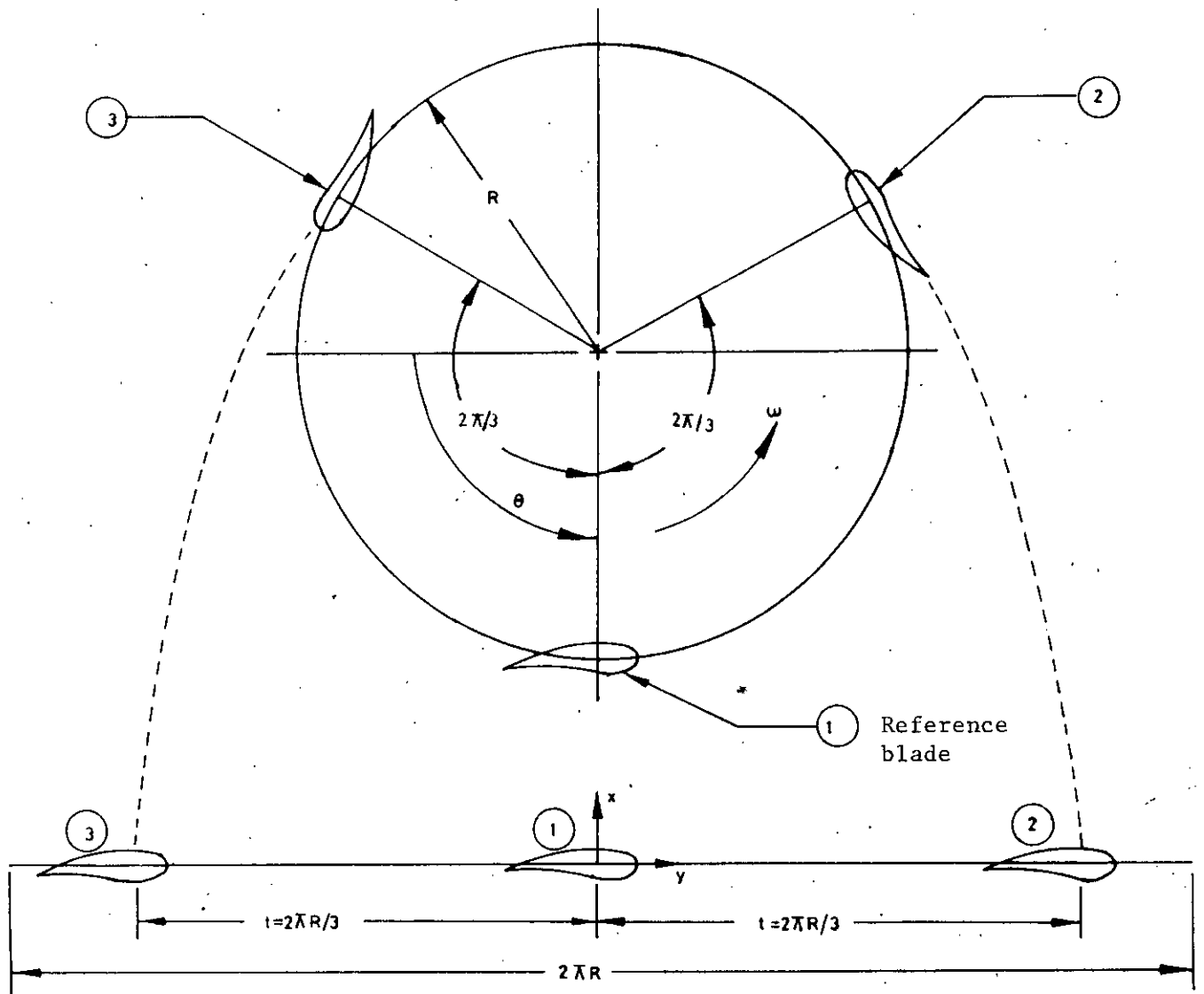


Figure 3.14 : Development of blades into cascade configuration.

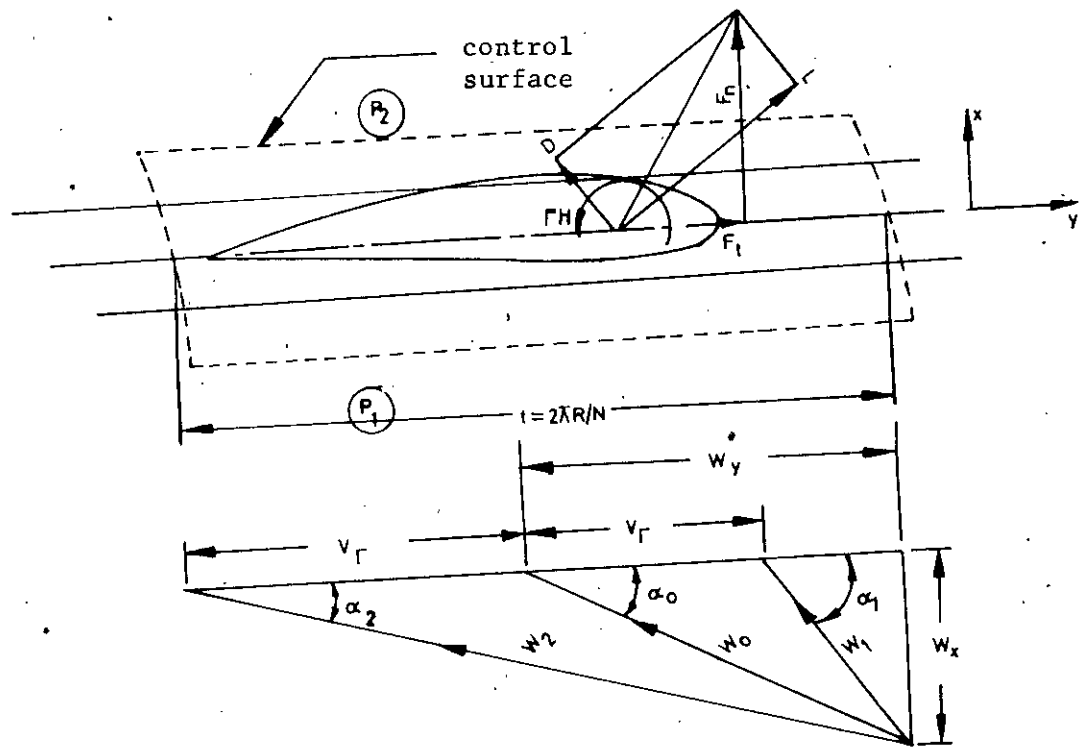


Figure 3.15 : Velocity diagram on the blade section.

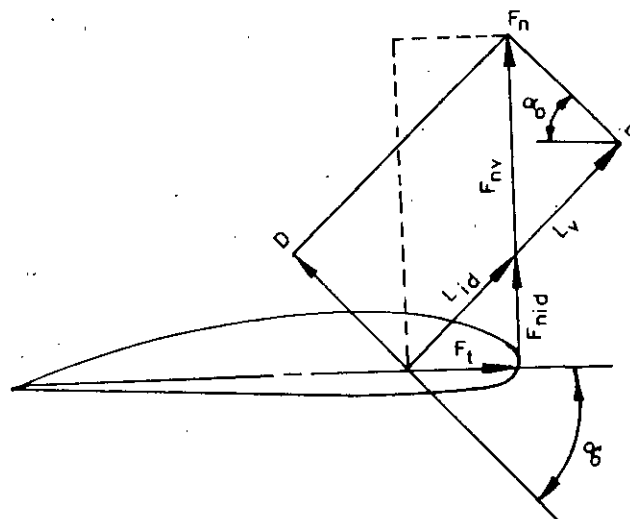


Figure 3.16 : Force diagram on the blade section.

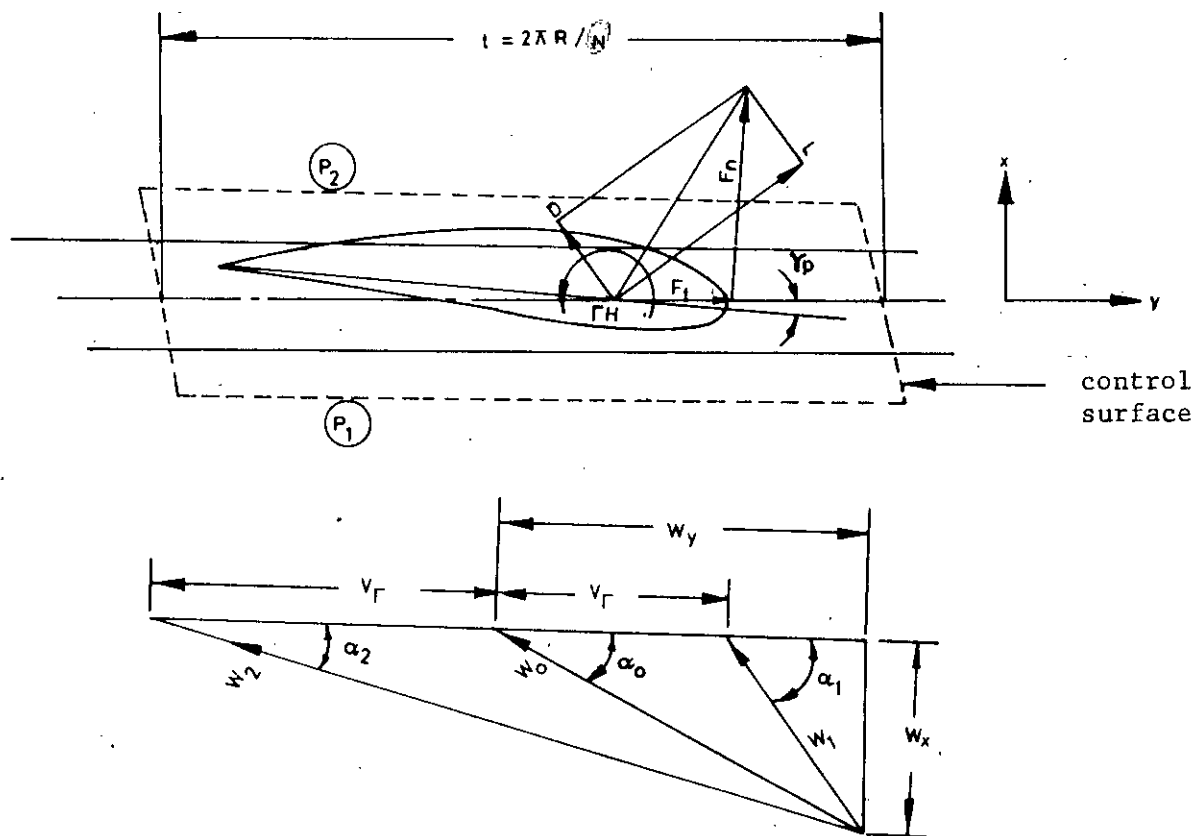


Figure 3.17 : Velocities and forces on blade airfoil with pitching in cascade configuration.

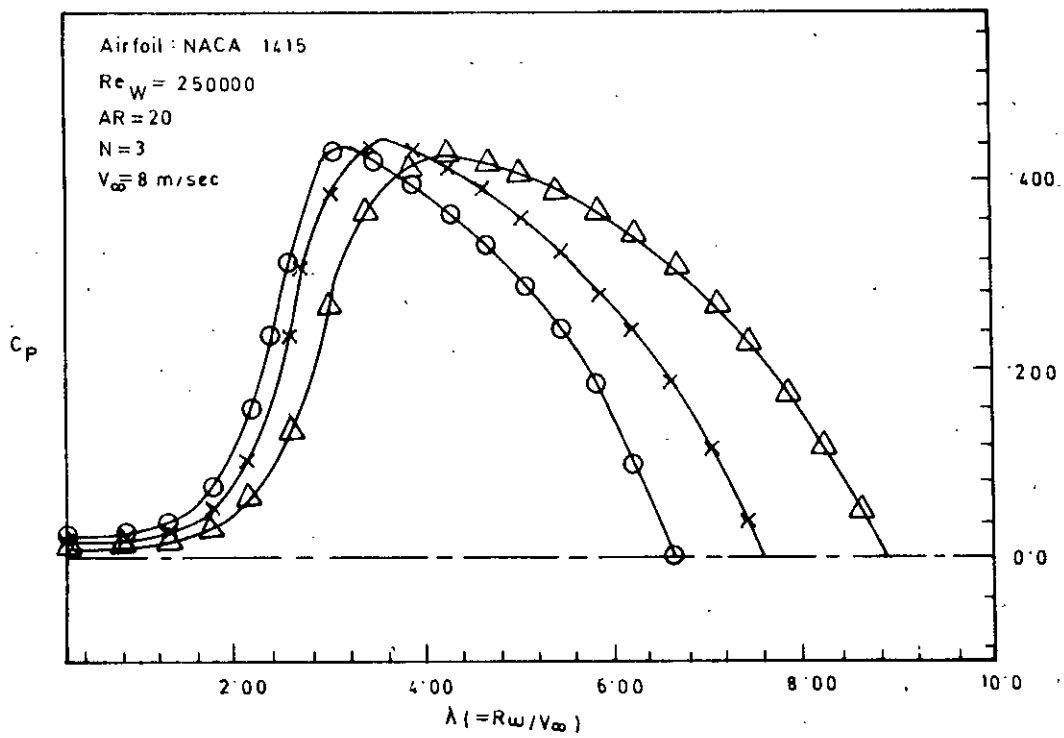


Figure 4.1 : Overall power coefficients vs. tip speed ratios at various solidities (calculated by cascade theory)

Symbol :	Δ	\times	\circ
σ :	.200	.300	.400

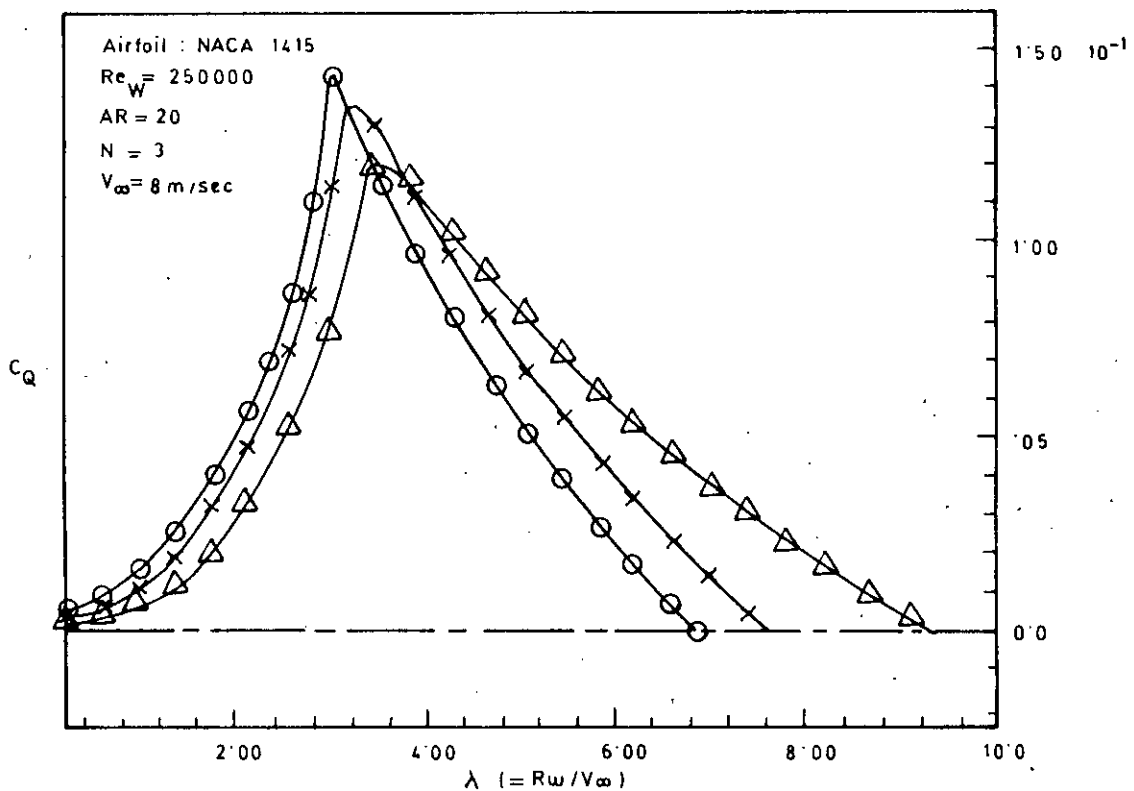


Figure 4.2 : Overall torque coefficients vs. tip speed ratios at various solidities (calculated by cascade theory).

Sybol :	Δ	\times	\circ
σ :	.200	.300	.400

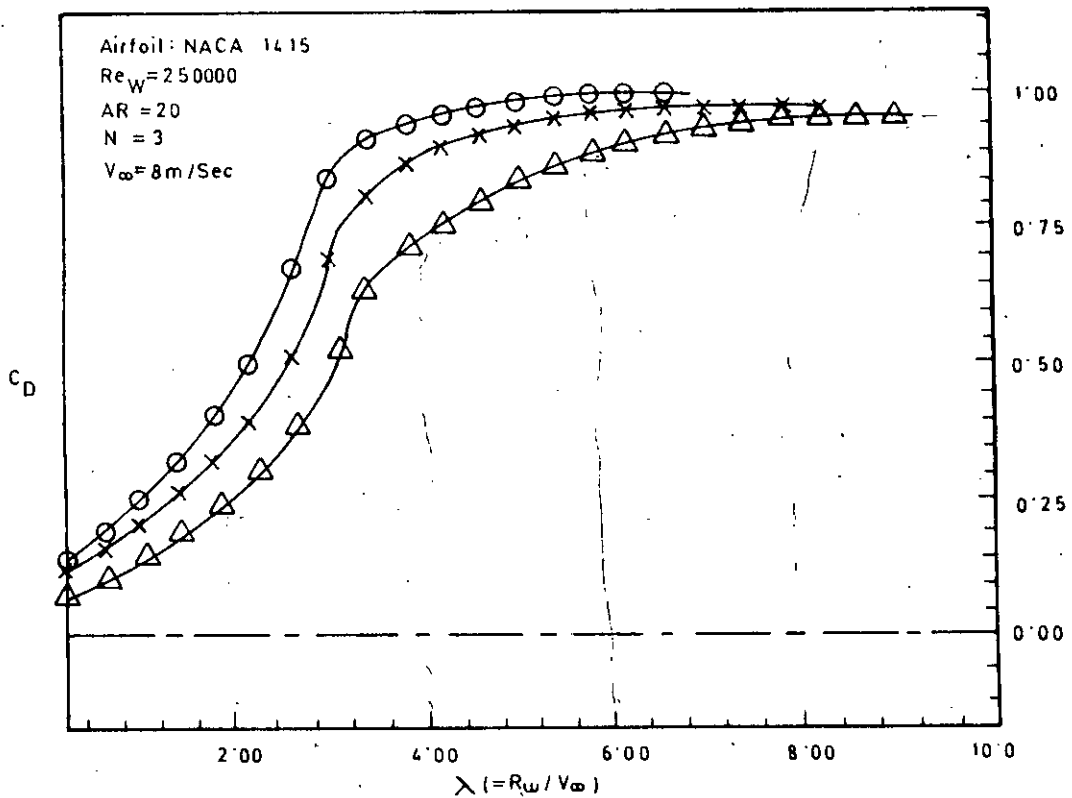


Figure 4.3 : Overall drag coefficients vs. tip speed ratios at various solidities (calculated by cascade theory).

Symbol : Δ \times \circ
 σ : .200 .300 .400

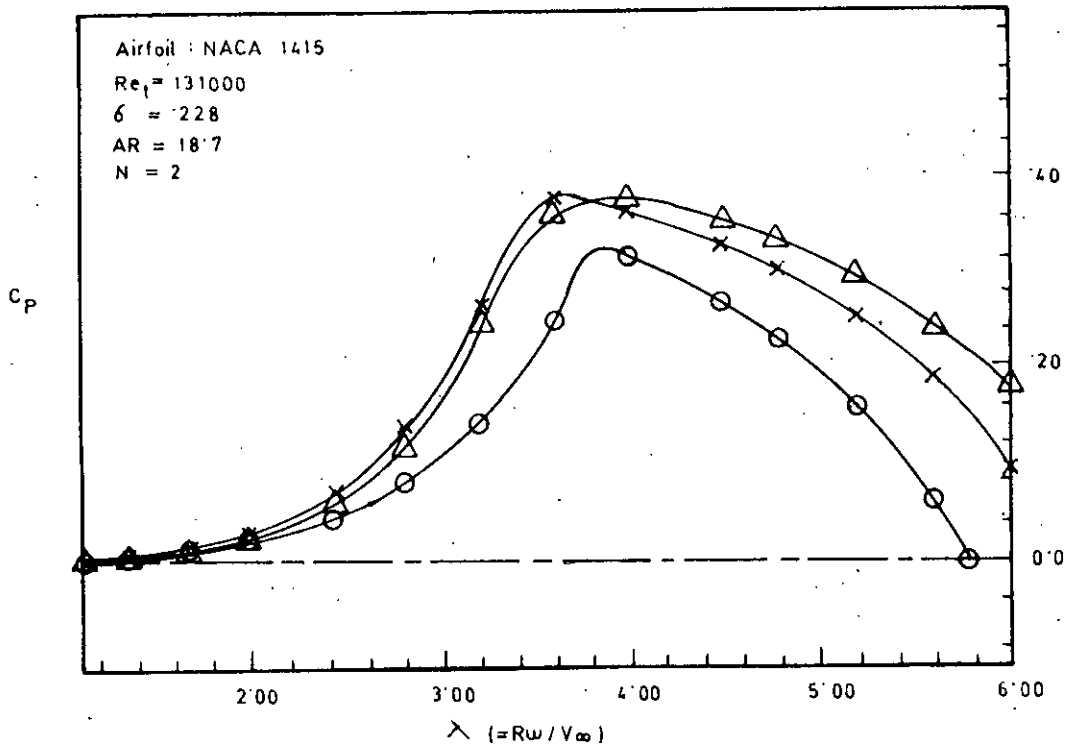


Figure 4.4 Overall power coefficients vs. tip speed ratios at different fixed blade pitchings (calculated by cascade theory).

Symbol : Δ \times \circ
(Fixed : 3.0 3.75 4.5
pitch)

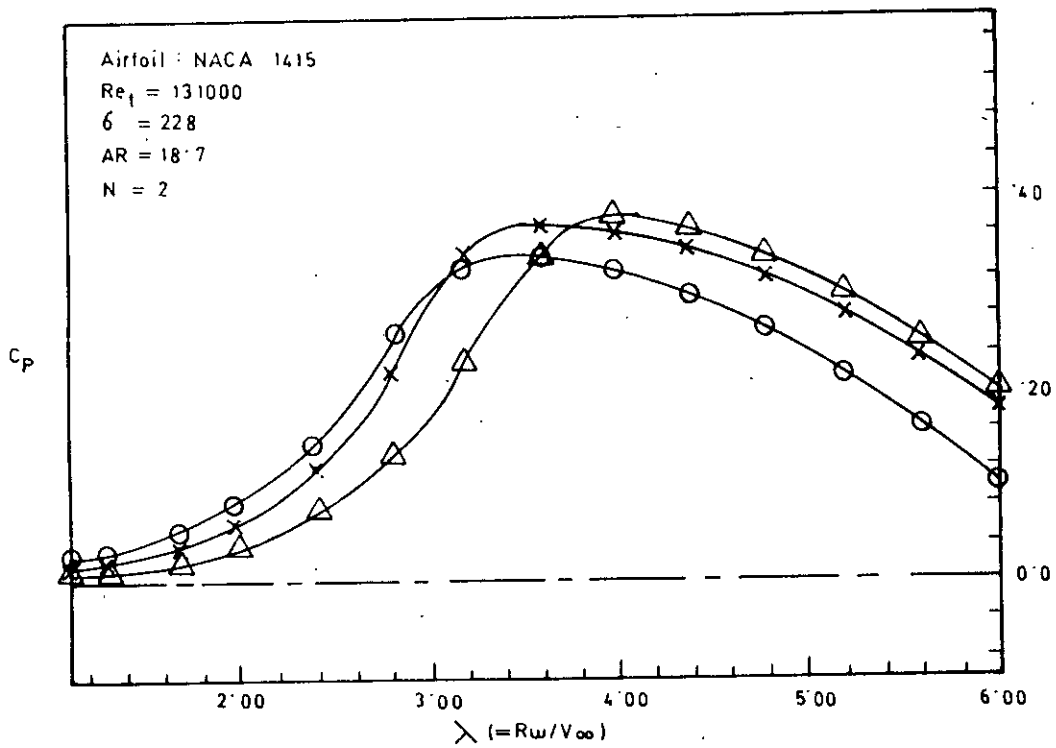


Figure 4.5 : Overall power coefficients vs. tip speed ratios at different amplitudes of sinusoidal pitch variation (calculated by cascade theory)

Symbol : Δ \times \circ
 γ_p (deg.) : 0, $3 \sin \theta$, $6 \sin \theta$

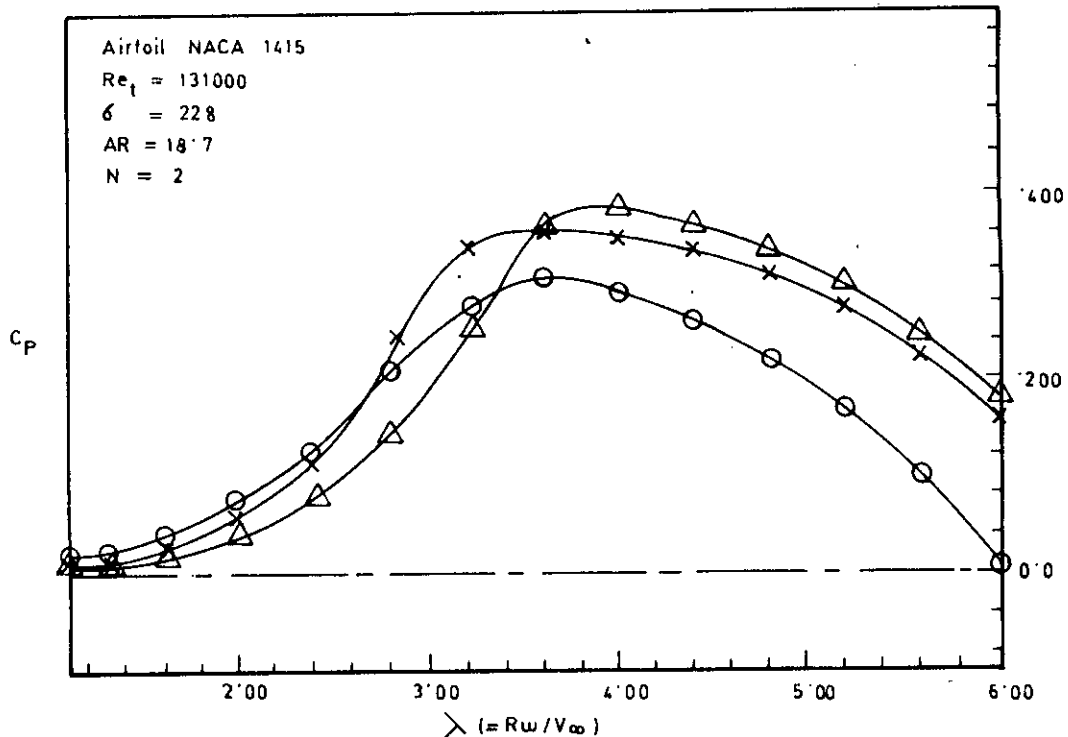


Figure 4.6: Overall power coefficients vs. tip speed ratios at different combined pitch (fixed + sinusoidal) variation (calculated by cascade theory).

Symbol : Δ \times \circ
(Fixed pitch + γ_p) : 0, $(3 + 3 \sin \theta)$, $(6 + 6 \sin \theta)$
 γ_p (deg.)

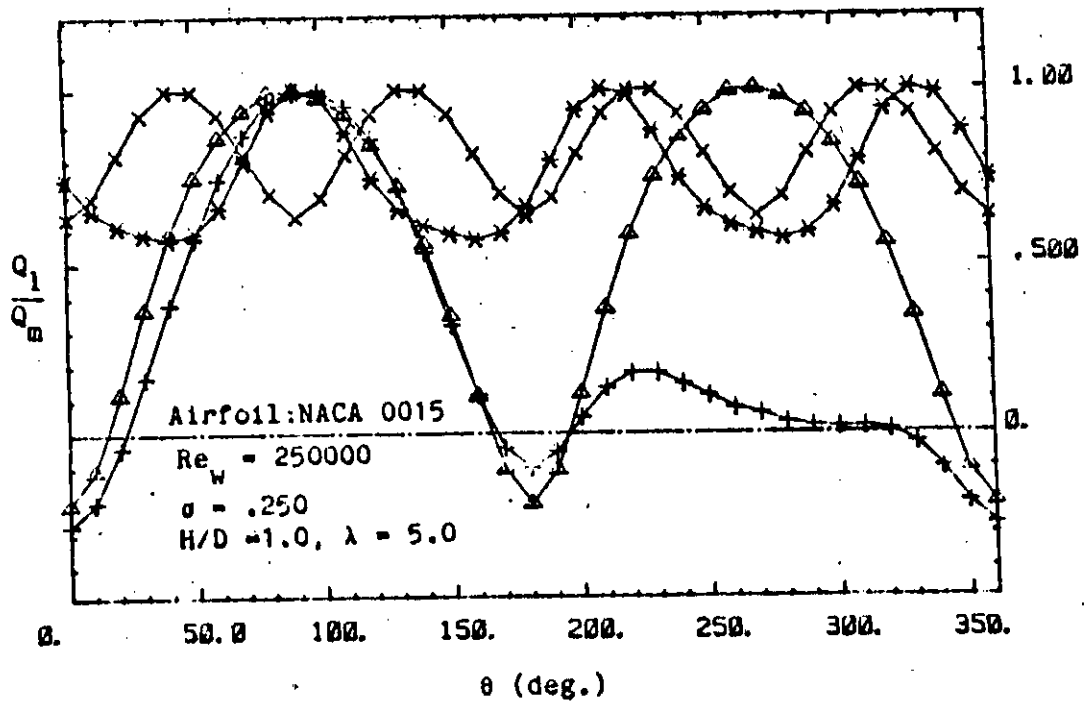


Figure 4.7 : Variations of instantaneous torques with azimuth for various no.of blades (calculated by cascade theory) (Ref.25)

Symbol :	+	Δ	*	x
N :	1	2	3	4

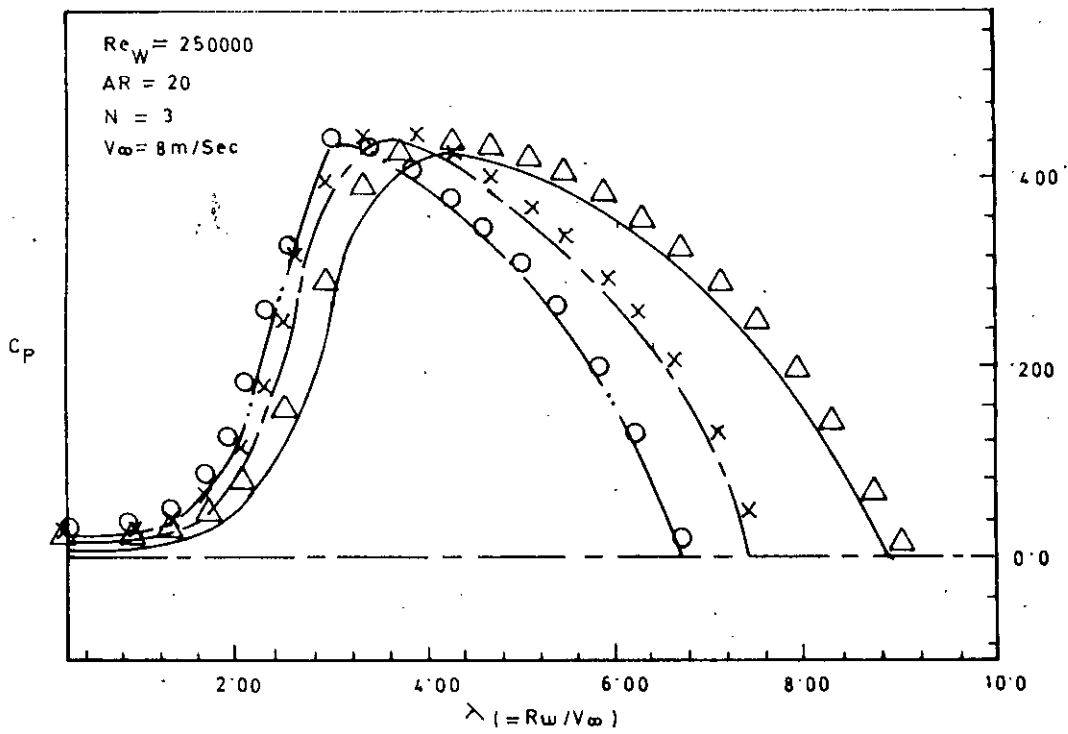


Figure 4.8: Comparisons of overall power coefficients at various solidities (calculated by cascade theory).

Symmetric (NACA : 0015) :	—	—	—
Cambered (NACA:1415) :	Δ	x	○
σ :	.200	.300	.400

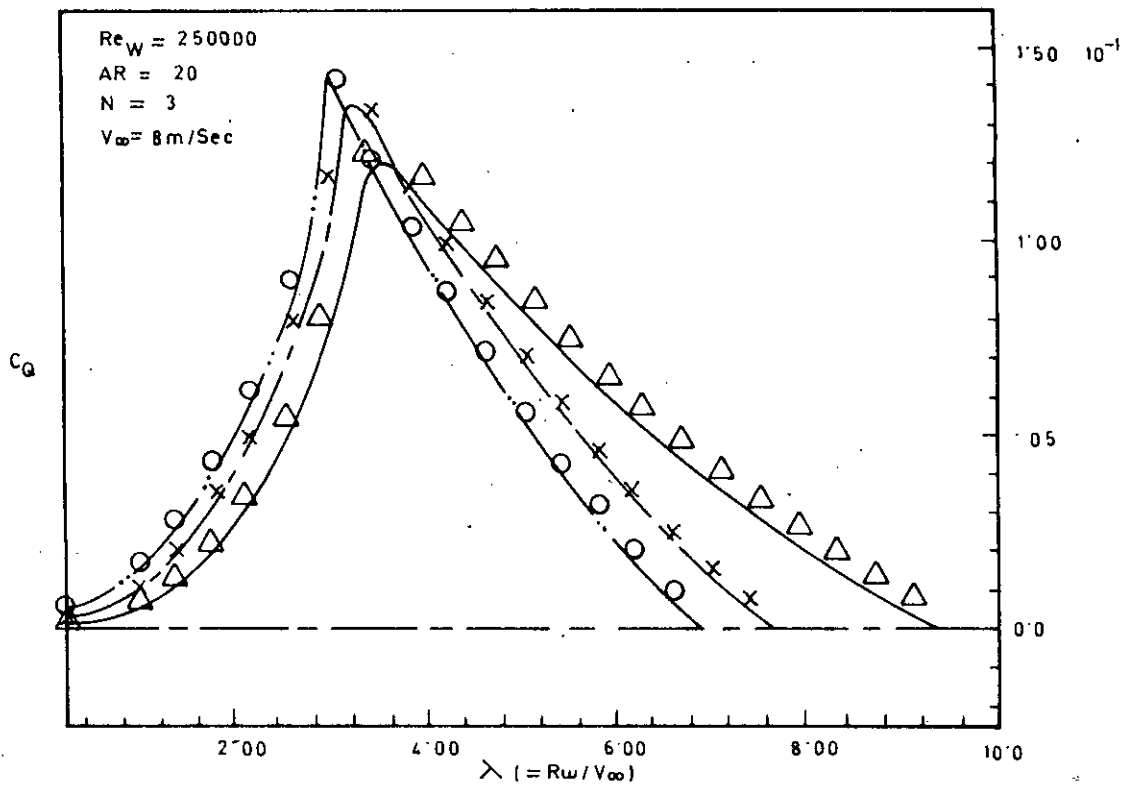


Figure 4.9 : Comparisons of overall torque coefficients at various solidities (calculated by cascade theory)

Symmetric (NACA : 0015) :	—	—	—
Cambered (NACA : 1415) :	Δ	x	○
σ :	.200	.300	.400

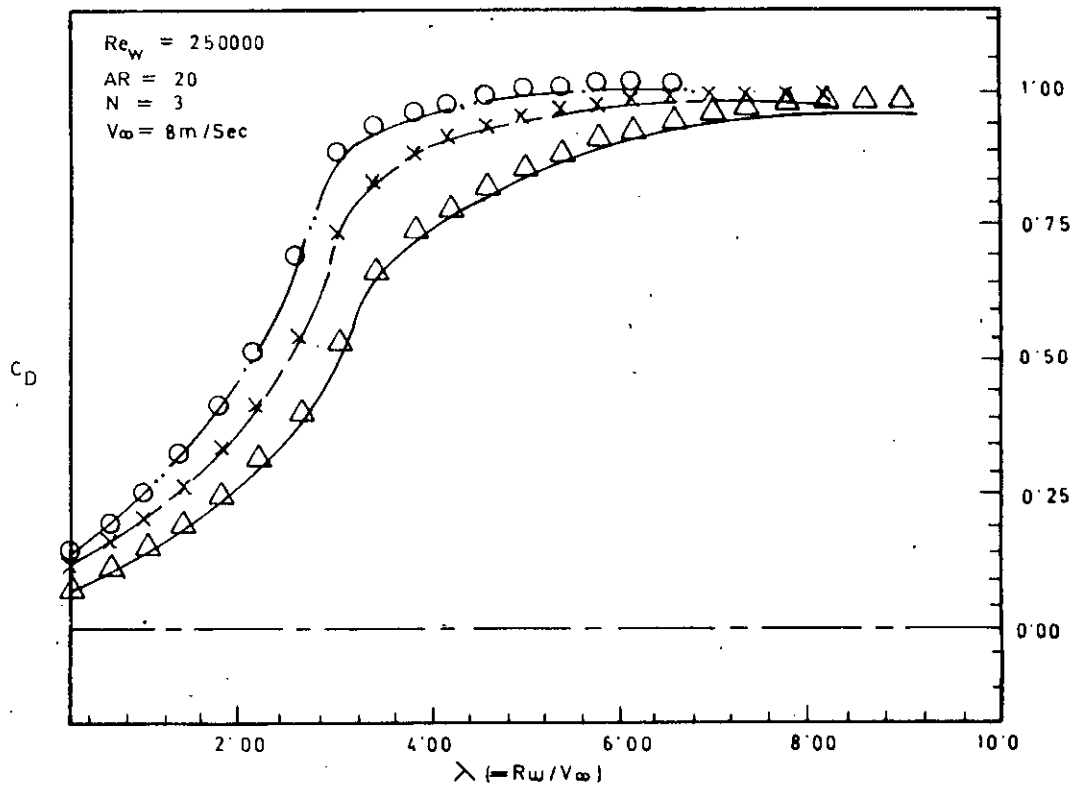


Figure 4.10 : Comparisons of overall drag coefficients at various solidities (calculated by cascade theory).

Symmetric (NACA : 0015) : ————
 Cambered (NACA : 1415) : Δ \times \circ
 σ : .200 .300 .400

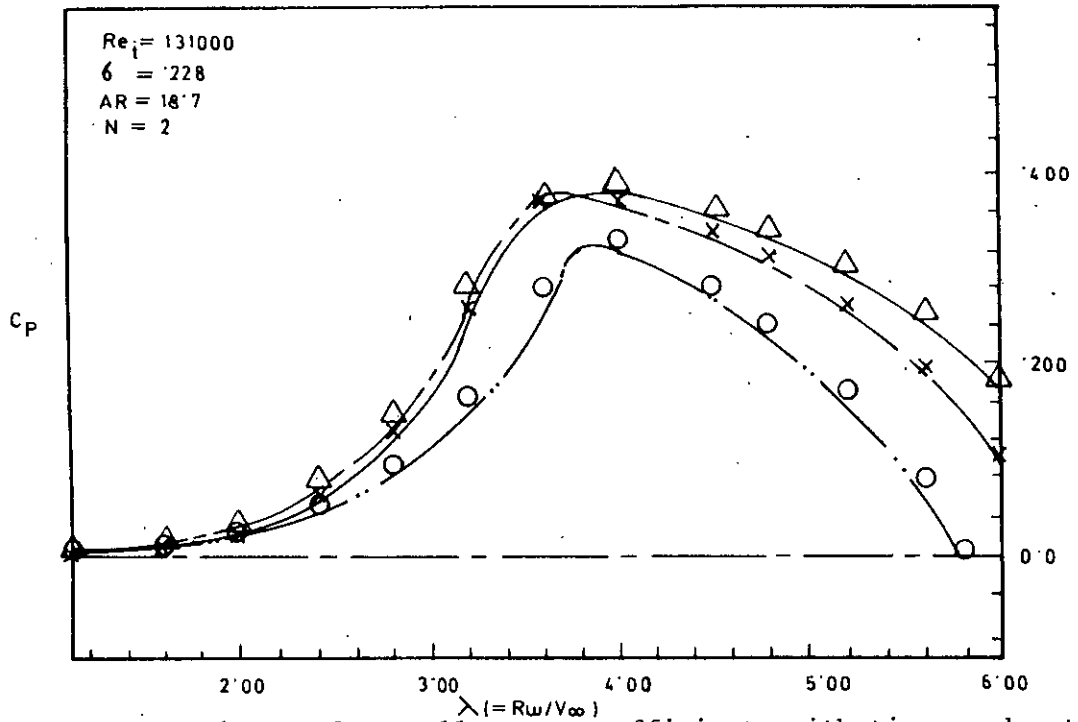


Figure 4.11 : Comparisons of overall power coefficients with tip speed ratios at different fixed blade pitchings (calculated by cascade theory).

Symmetric (NACA : 0015) : ————
 Cambered (NACA : 1415) : Δ \times \circ
 Fixed pitch (deg) : 0 3 6

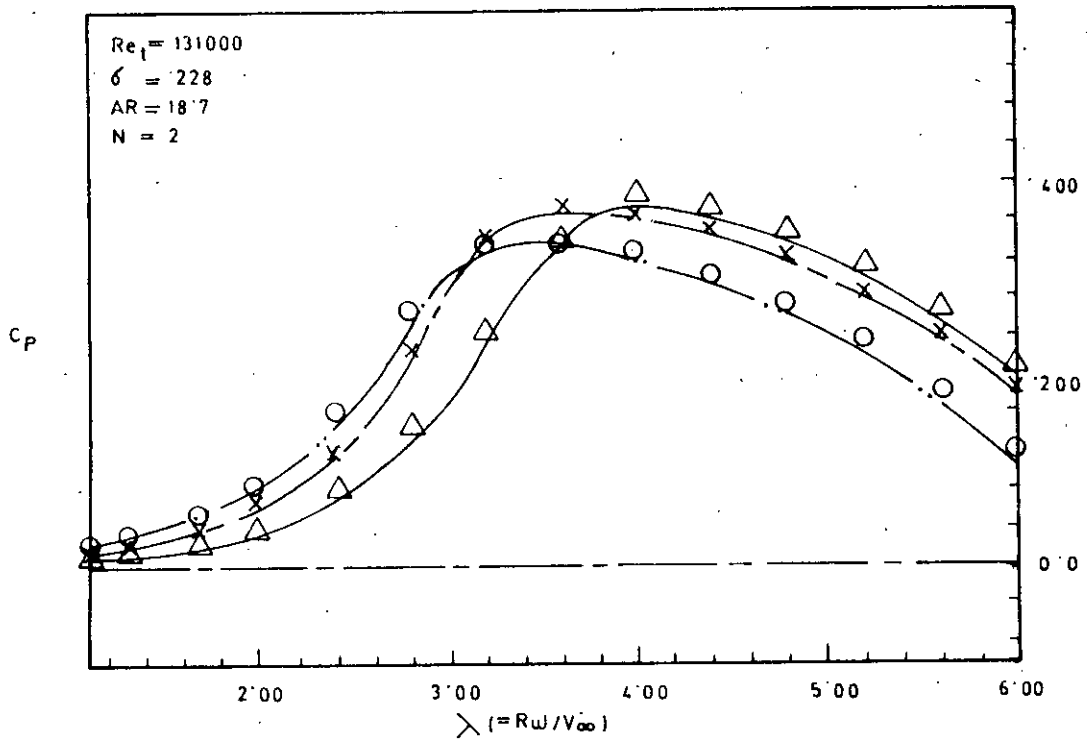


Figure 4.12: Comparisons of overall power coefficients with tip speed ratios at different amplitudes of sinusoidal pitch variation (calculated by cascade theory).

Symmetric (NACA:0015) : ————
 Cambered (NACA:1415) : Δ \times \circ
 γ_p (deg.) : 0 3 sin 6 sin

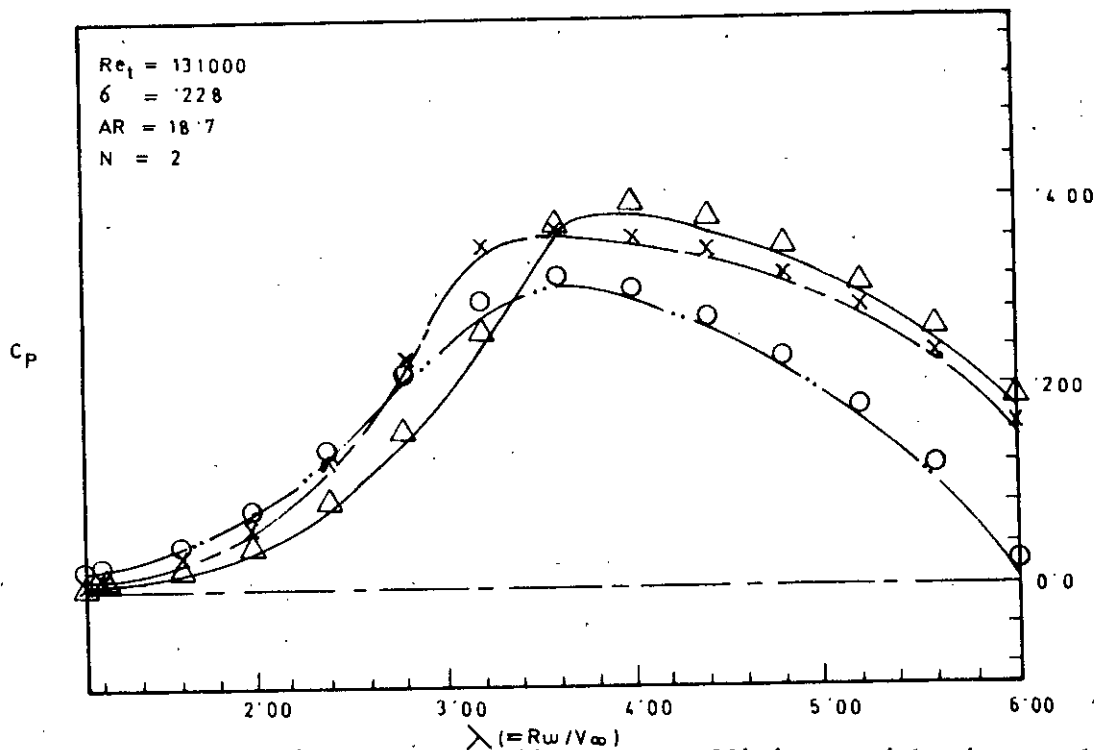


Figure 4.13: Comparisons of overall power coefficients with tip speed ratios at different (fixed + amplitudes of sinusoidal) pitch variation (calculated by cascade theory).

Symmetric (NACA: 0015) : ————
 Cambered (NACA: 1415) : Δ \times \circ
 (Fixed pitch + γ_p) : \circ (3+3sin θ) (6+6sin θ)
 deg.

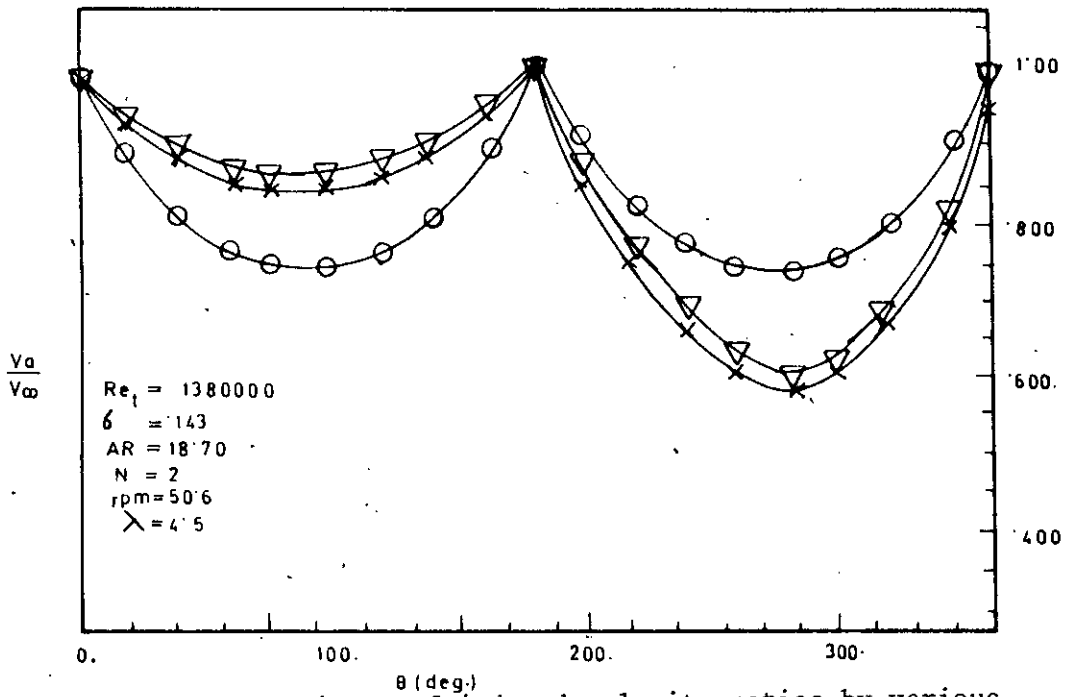


Figure 4.14 : Comparisons of induced velocity ratios by various analytical methods.

- △ calc. (cascade theory ; NACA : 0015)
- x calc. (cascade theory ; NACA : 1415)
- calc. (simple multiple streamtube theory; NACA: 0015)

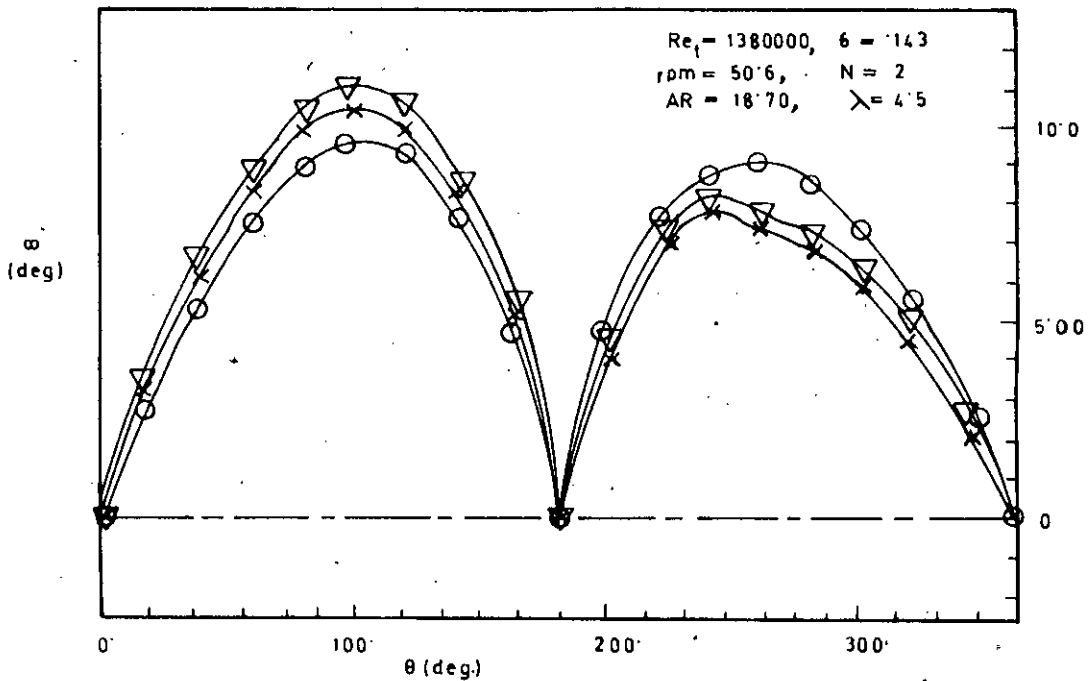


Figure 4.15: Comparison of local angles of attack by various analytical methods.

- △ calc. (cascade theory; NACA : 0015)
- x calc. (cascade theory; NACA : 1415)
- calc. (simple multiple streamtube theory; NACA 0015)

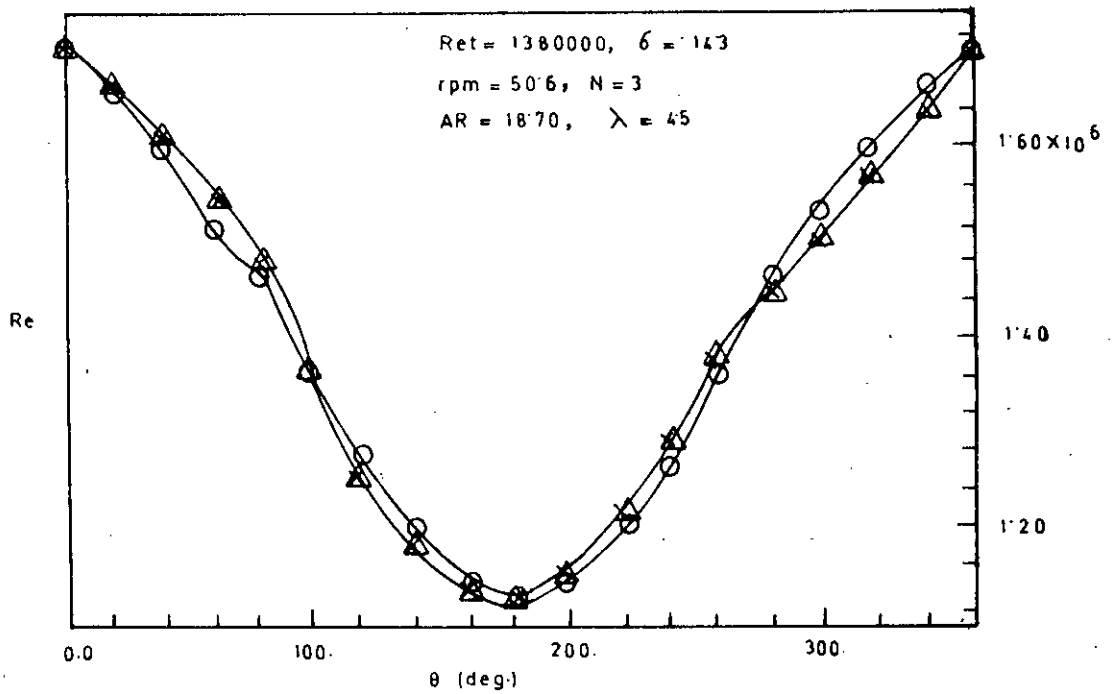


Figure 4.16: Comparisons of local Reynolds number by various analytical methods.

- Δ calc. (cascade theory; NACA : 0015)
- \times calc. (cascade theory; NACA : 1415)
- \circ calc. (simple multiple streamtube theory; NACA: 0015)

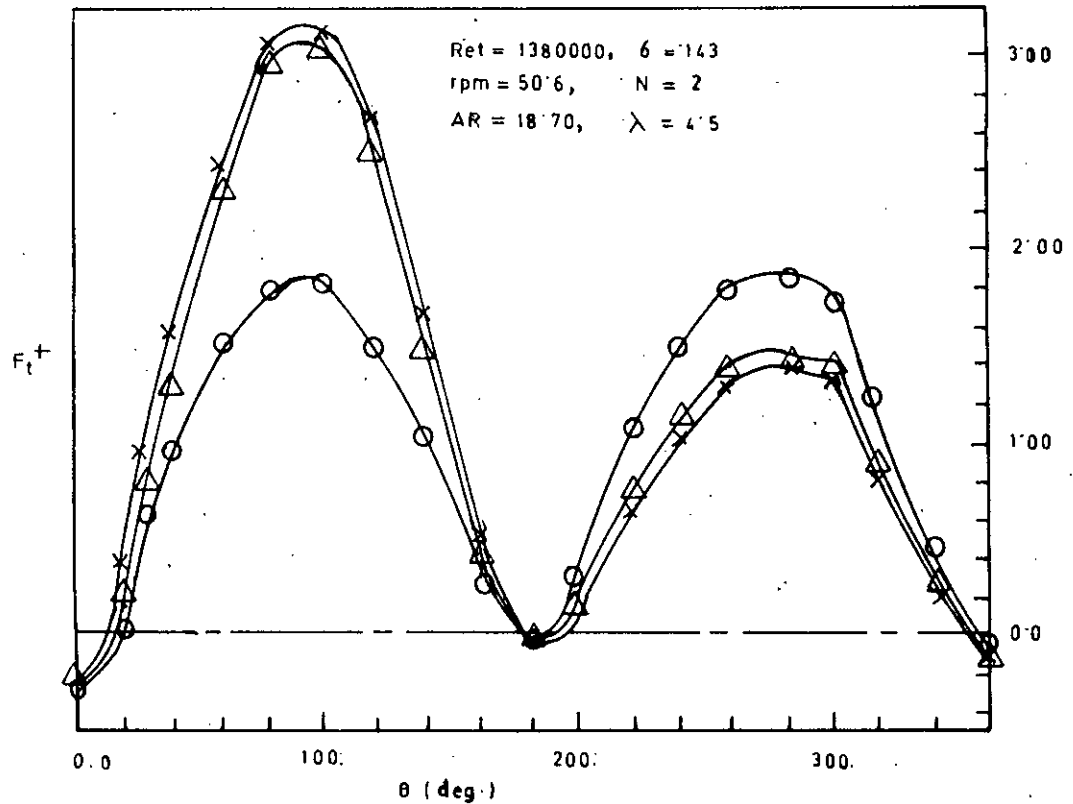


Figure 4.17: Comparison of local non-dimensional tangential forces by various analytical methods.

- Δ calc. (cascade theory; NACA : 0015)
- \times calc. (cascade theory; NACA : 1415)
- \circ calc. (simple multiple streamtube theory; NACA:0015)

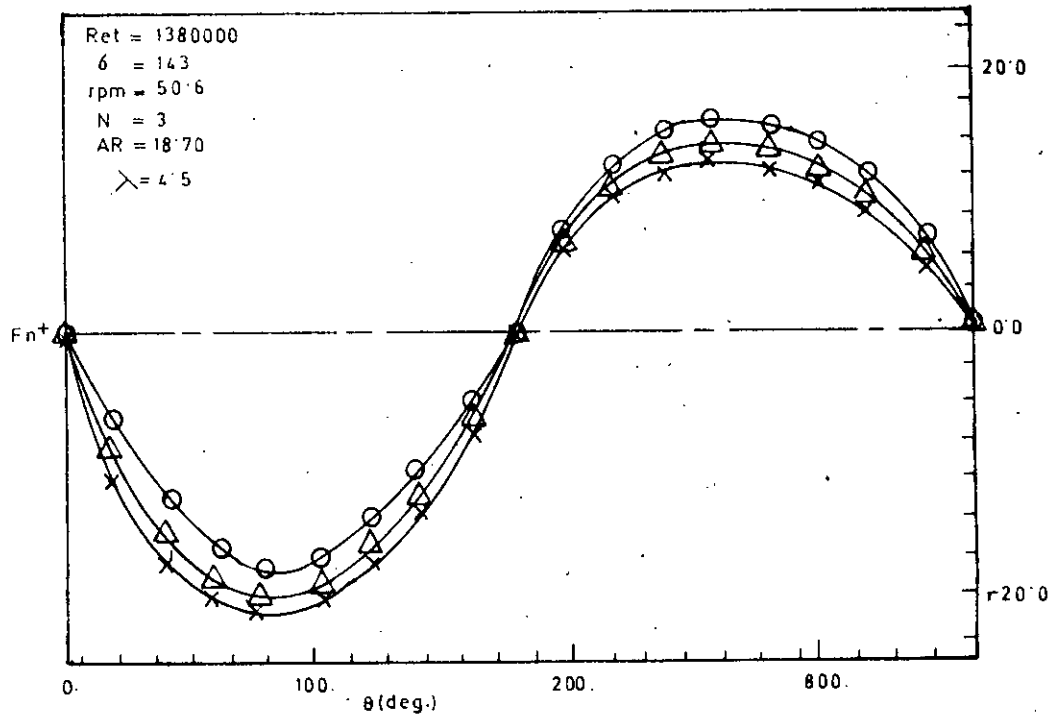


Figure 4.18: Comparisons of local non-dimensional normal forces by various analytical methods.

- Δ calc. (cascade theory; NACA : 0015)
- \times calc. (cascade theory; NACA : 1415)
- \circ calc. (simple multiple streamtube theory; NACA: 0015)

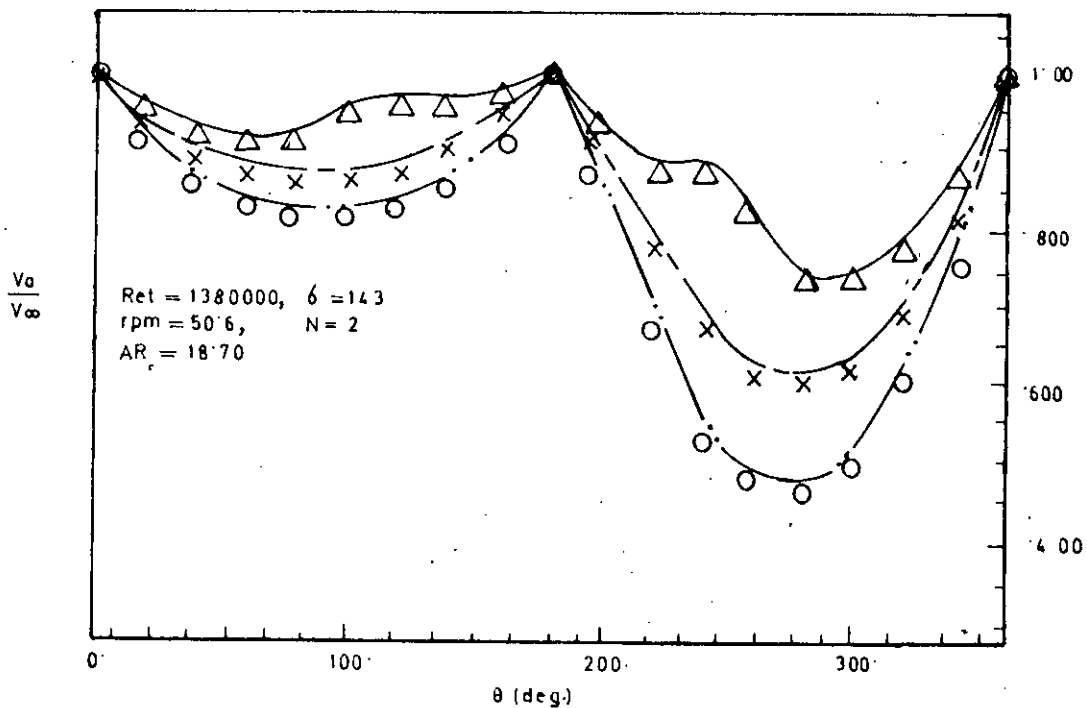


Figure 4.19: Comparisons of induced velocities with azimuth at different tip speed ratios (calculated by cascade theory).

- | | | | |
|-----------------------|------------|----------|------------|
| Symmetric (NACA:0015) | : ———— | — | — |
| Cambered (NACA :1415) | : Δ | \times | \circ |
| λ | : | 3.00 | 4.00 .6.00 |

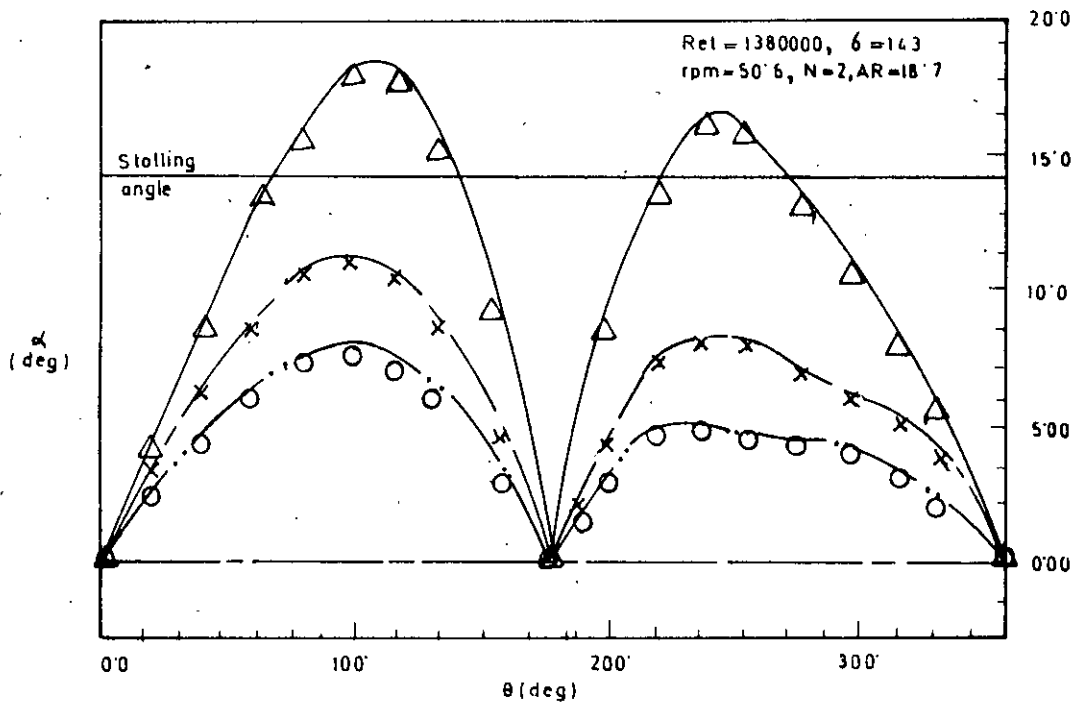


Figure 4.20: Comparisons of local angles of attack with azimuth at different tip speed ratios (calculated by cascade theory).

Symmetric (NACA:0015) : ————
 Cambered (NACA:1415) : Δ x \circ
 λ : 3.00 4.00 6.00

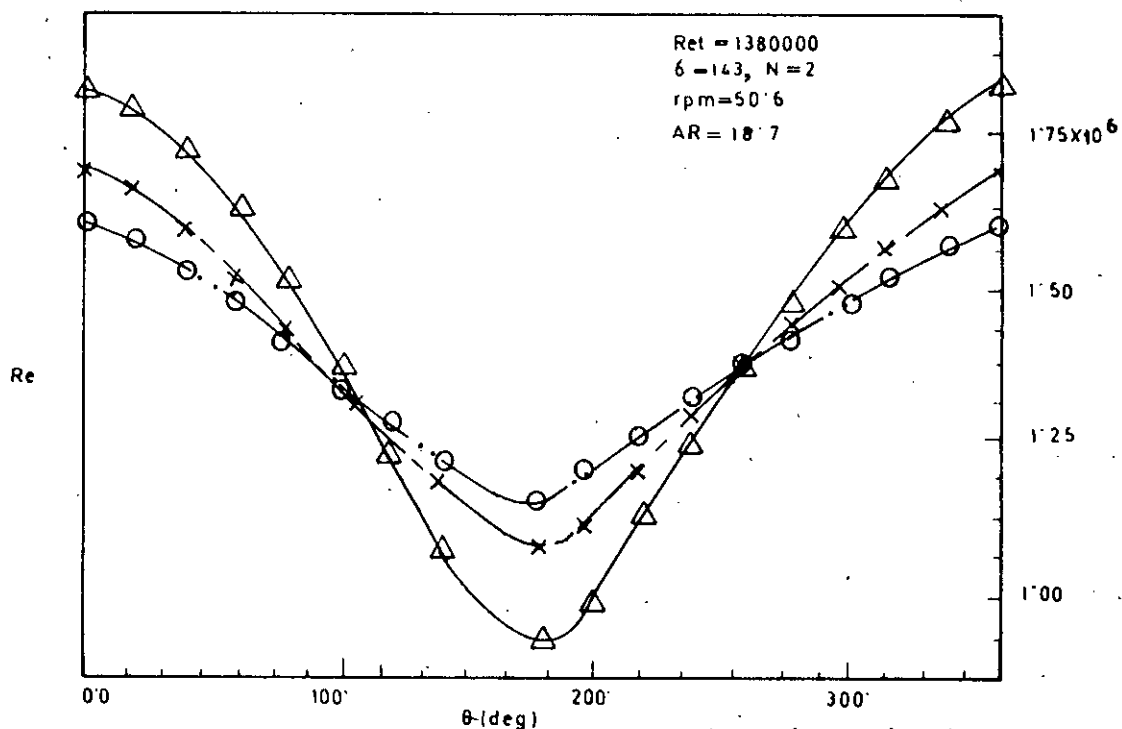


Figure 4.21: Comparisons of local Reynolds number with azimuth at different tip speed ratios (calculated by cascade theory).

Symmetric (NACA:0015) : ————
 Cambered (NACA:1415) : Δ x \circ
 λ : 3.00 4.00 6.00

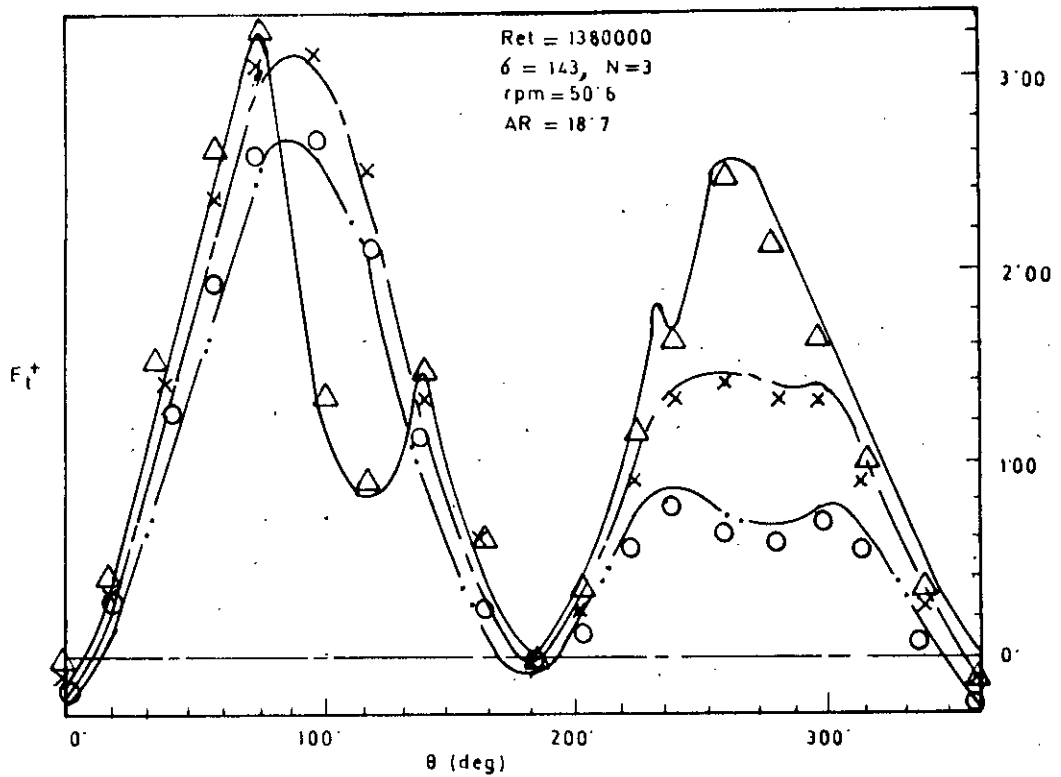


Figure 4.22: Comparisons of local non-dimensional tangential force with azimuth at different tip speed ratios (calculated by cascade theory).

Symmetric (NACA: 0015) : ————
 Cambered (NACA: 1415) : Δ x ○
 λ : 3.00 4.00 6.00

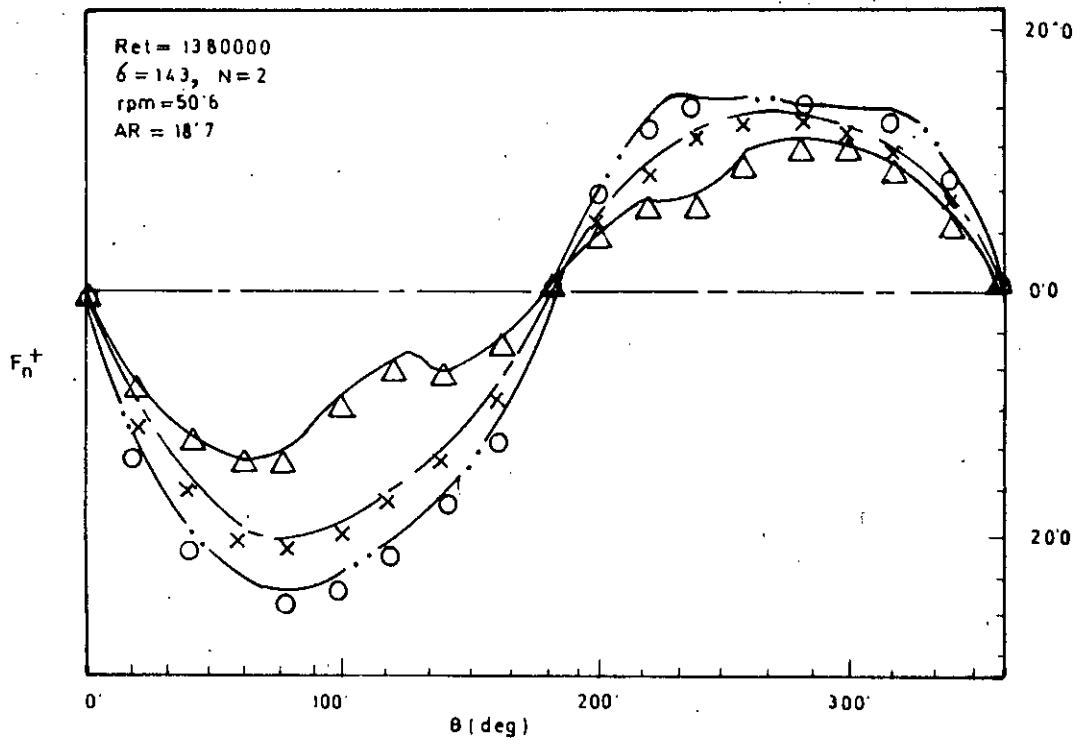


Figure 4.23: Comparisons of local non-dimensional normal forces with azimuth at different tip speed ratios (calculated by cascade theory).

Symmetric (NACA: 0015) : ————
 Cambered (NACA: 1415) : Δ x ○
 λ : 3.00 4.00 6.00

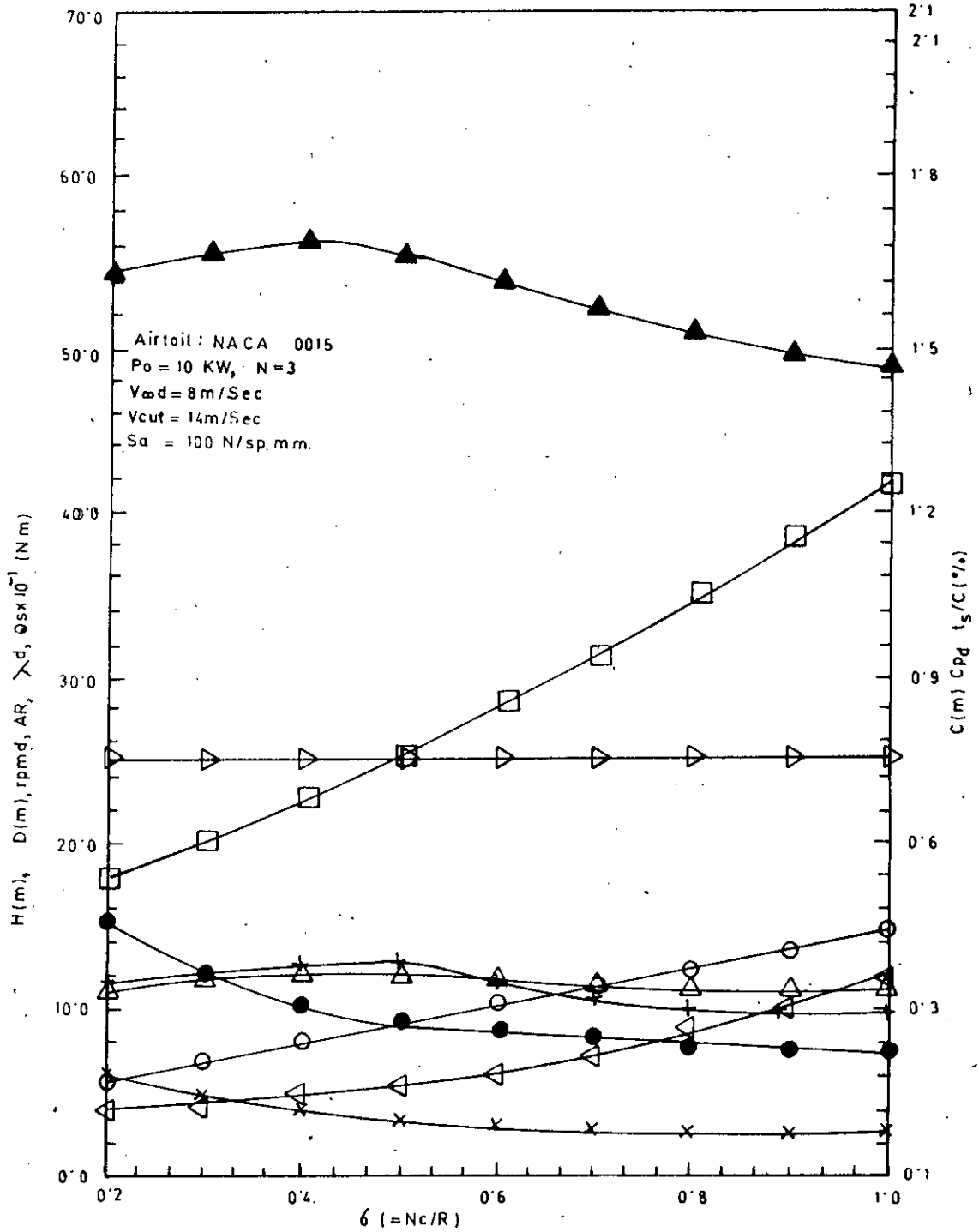


Figure 5.1: Design configurations of variable speed turbines at various solidities (calculated by cascade theory)

Symbol	:	○	●	□	△	▲	+	x	▷	◁
Parameter	:	H	D	C	AR	rpm _d	C _{pd}	λ_d	t _s /CZ	Q _s

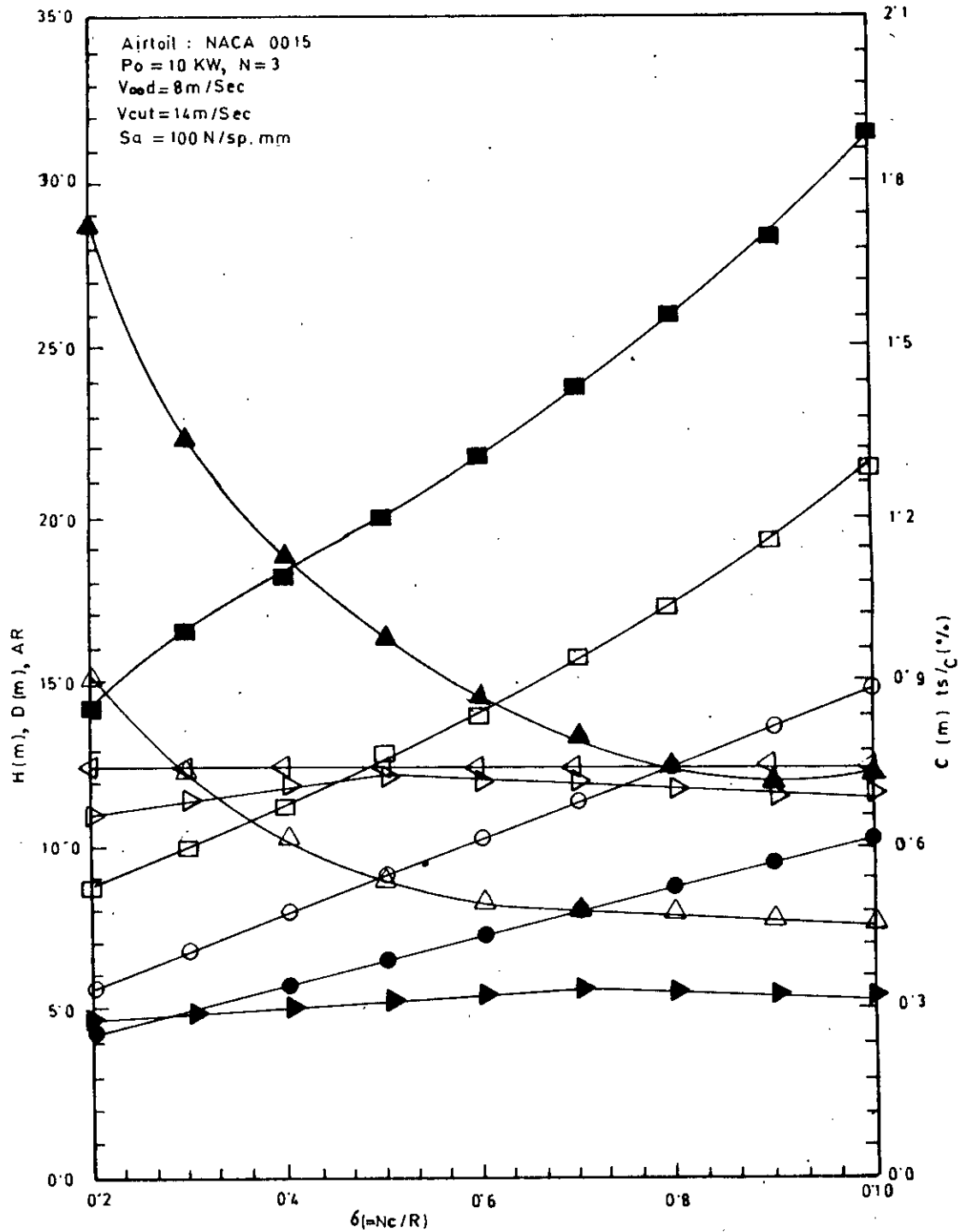


Figure 5.2: Comparisons of design configurations of variable speed turbines at various solidities (calculated by cascade theory).

Symbol	(Overhanged support)	:	○	△	□	▷	◁
	(Simple support)(Ref. [25]):	:	●	▲	■	▶	◀
Parameter	:	:	H	D	C	AR	t _s /CZ

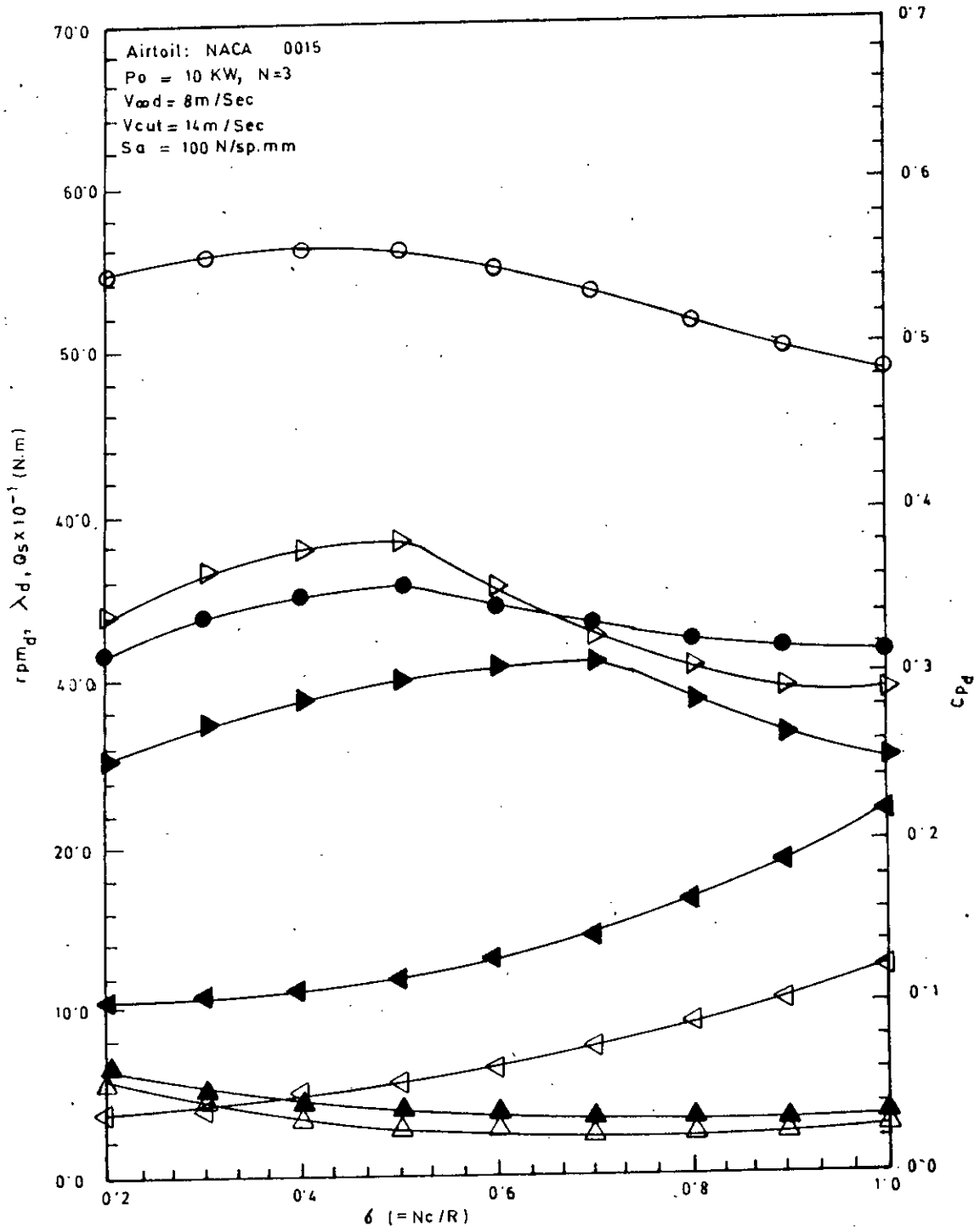


Figure 5.3: Comparisons of design configurations of variable speed turbines at various solidities (calculated by cascade theory)

Symbol (Overhanged support) : ◁ ▷ △ ▽
 Symbol (Simple support) (Ref. [25]) : ● ► ▲ ◄
 Parameter : rpm_d Cp_d λ_d Q_s

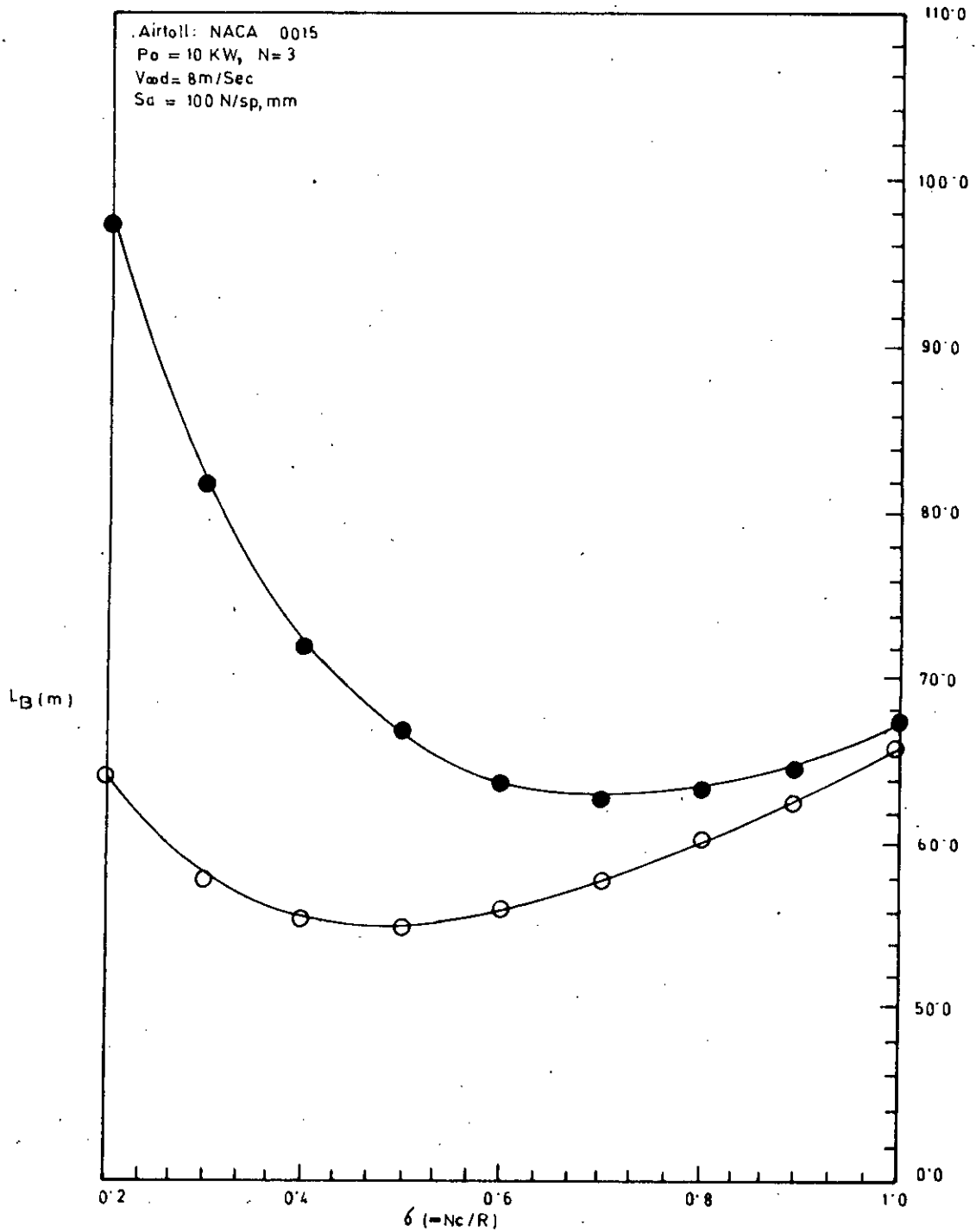


Figure 5.4: Comparisons of total blade length (L_B) at various solidities (calculated by cascade theory).

Symbol	○	●	
Blade support	Overhanged	Simple (Ref. [25])	

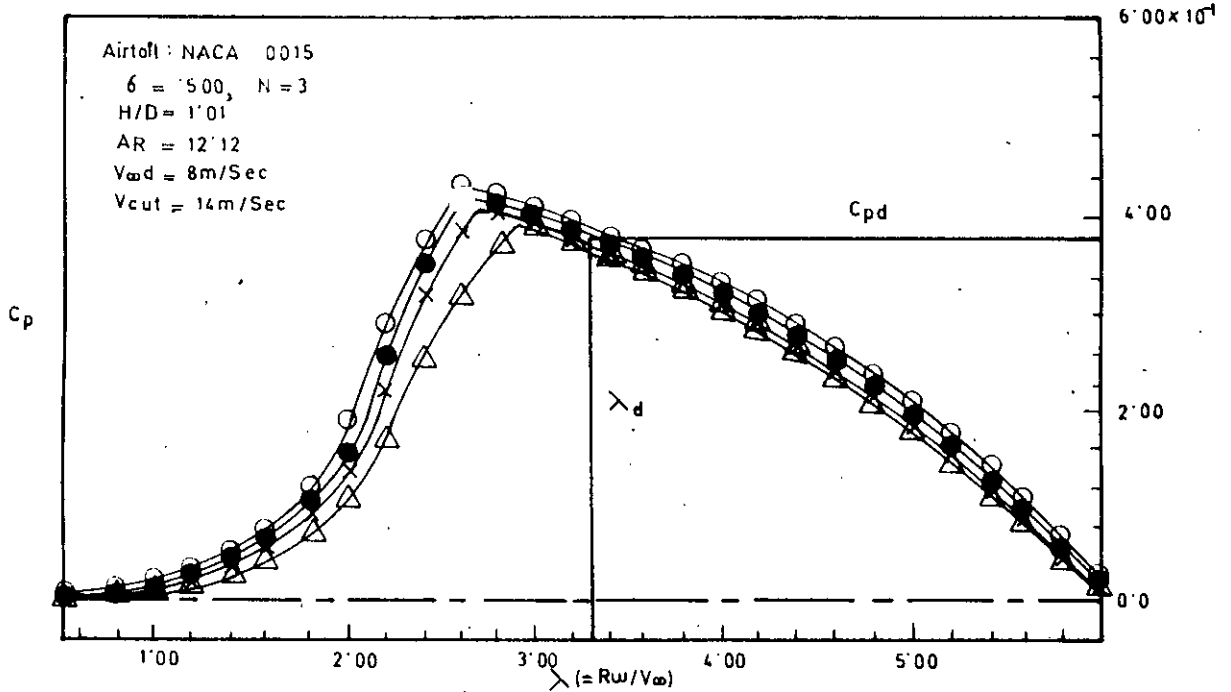


Figure 5.5: Variations of overall power coefficients with tip speed ratios at different wind speeds (calculated by cascade theory).

Symbol	:	Δ	X	\bullet	O
V_{∞} (m/sec)	:	4	8	12	14

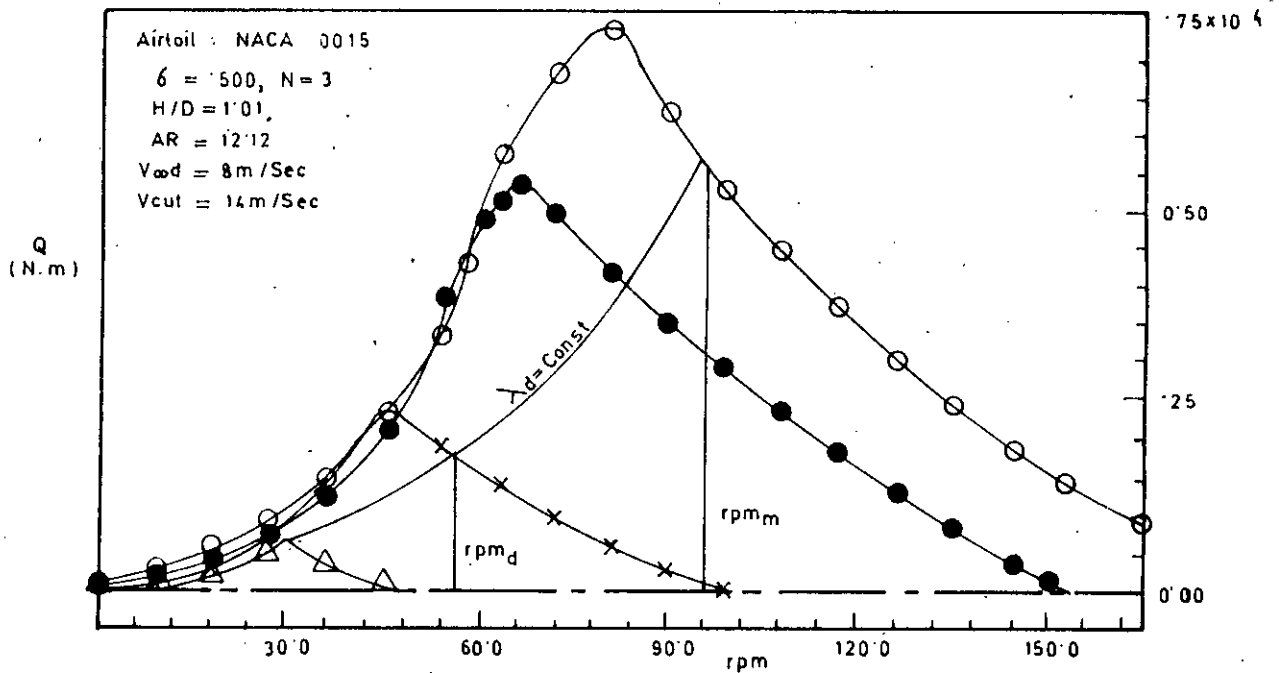


Figure 5.6: Variations of overall torques with rpm at various wind speeds (calculated by cascade theory).

Symbol	:	Δ	X	\bullet	O
V_{∞} (m/sec)	:	4	8	12	14

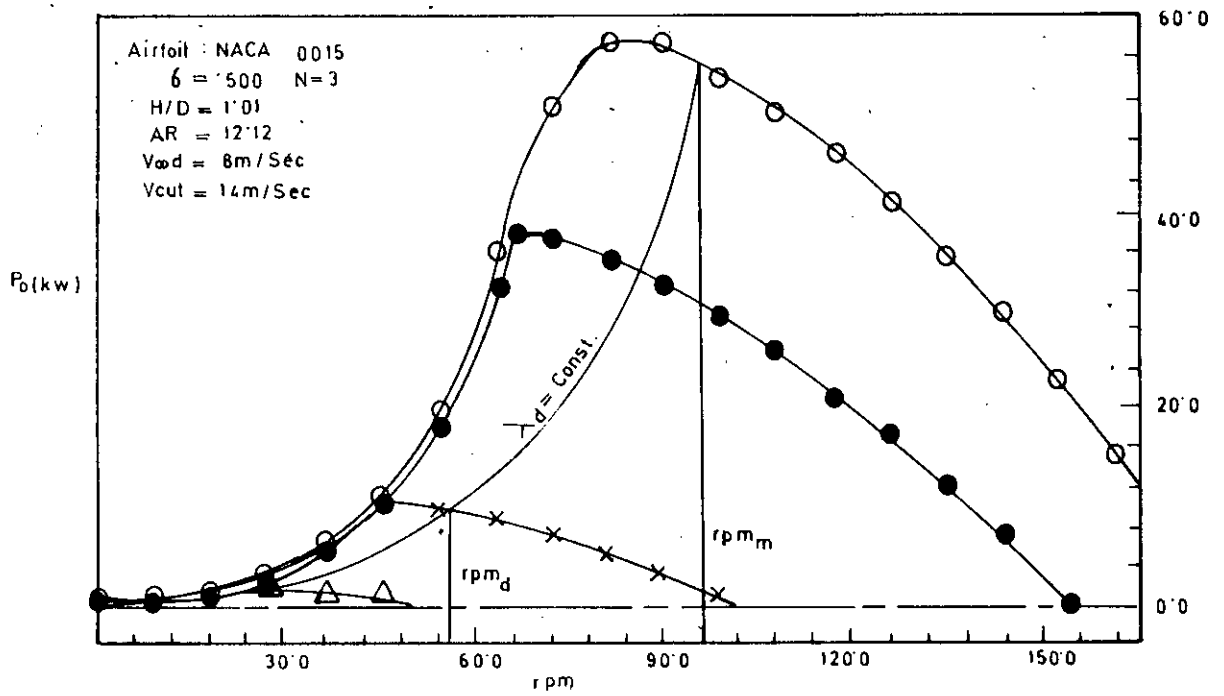


Figure 5.7: Variations of overall power with rpm at various wind speeds (calculated by cascade theory).

Symbol	:	Δ	X	\bullet	0
V_{∞} (m/sec)	:	4	8	12	14

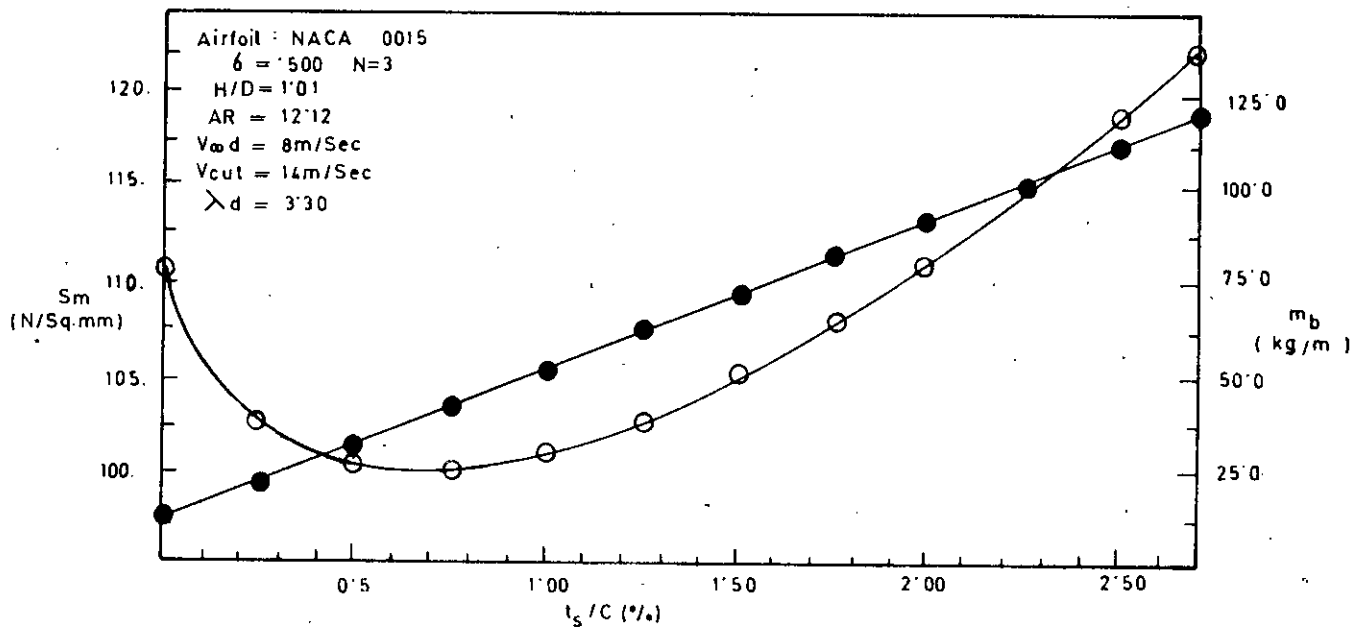


Figure 5.8: Variations of blade mass and maximum blade stress with blade skin thickness (calculated by cascade theory).

Symbol	:	0	\bullet
Parameter	:	S_m	m_b

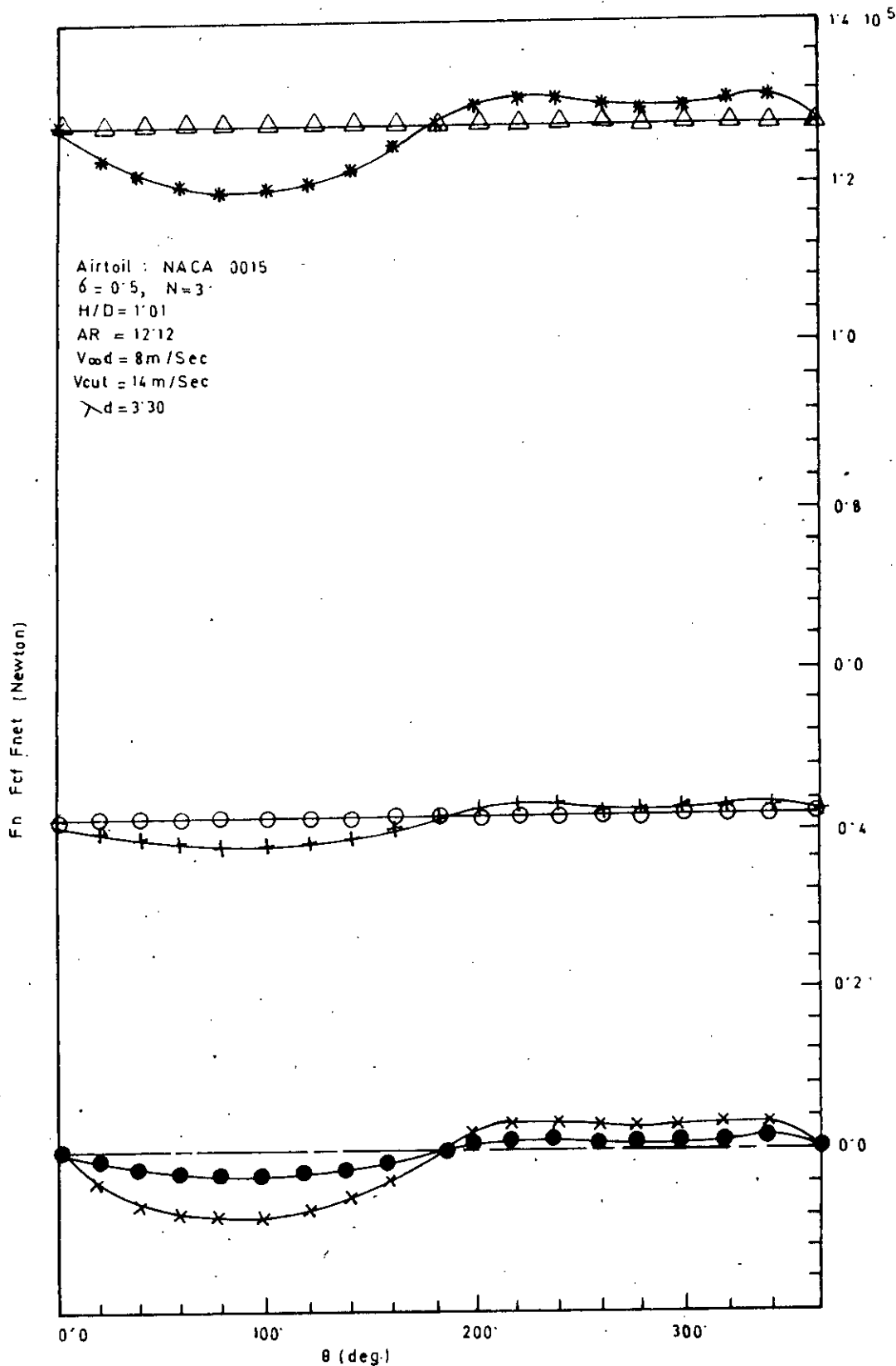


Figure 5.9 : Variations of normal, centrifugal and net normal forces with azimuth angle (calculated by cascade theory).

Symbol	:	●	○	+	X	△	*
Parameter	:	F_n	F_{cf}	F_{net}	F_n	F_{cf}	F_{net}
V_{∞} (m/sec)	:	8.0 (design)			14.0 (cutout)		

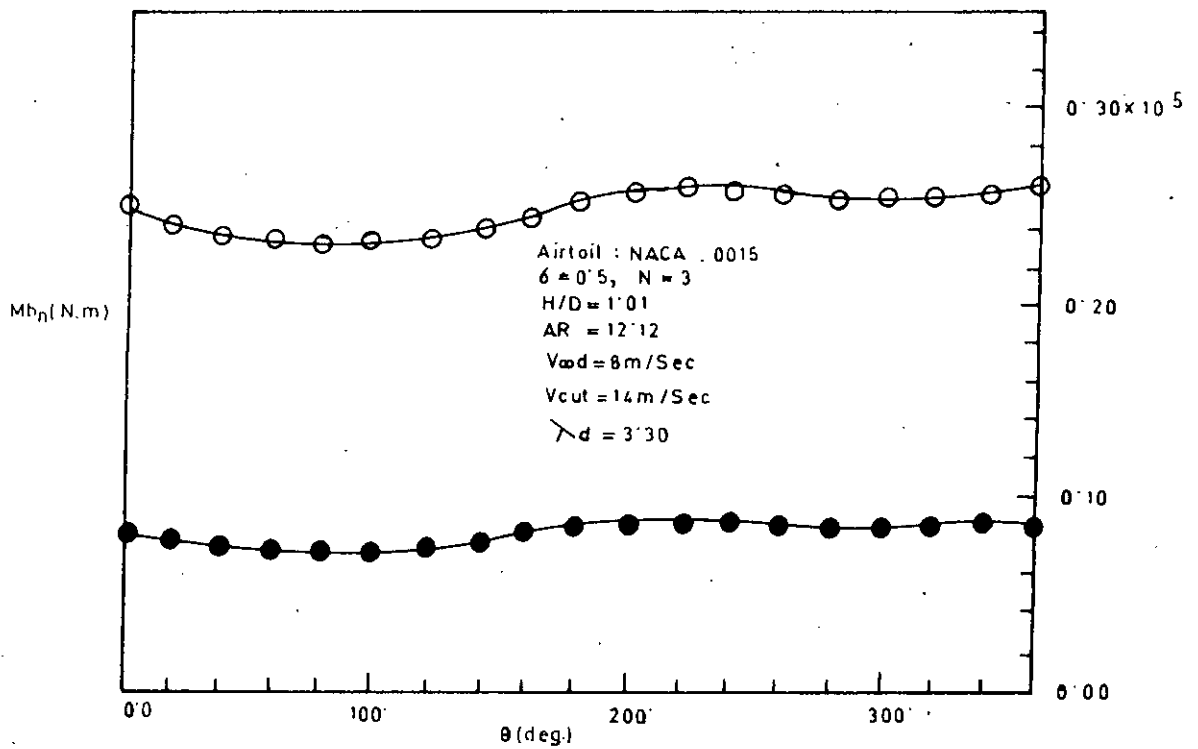


Figure 5.10: Variations of bending moments due to normal forces with azimuth angle (calculated by cascade theory).

Symbol	:	●	○
V_{∞} (m/sec)	:	8.0 (design)	14.0 (cutout)

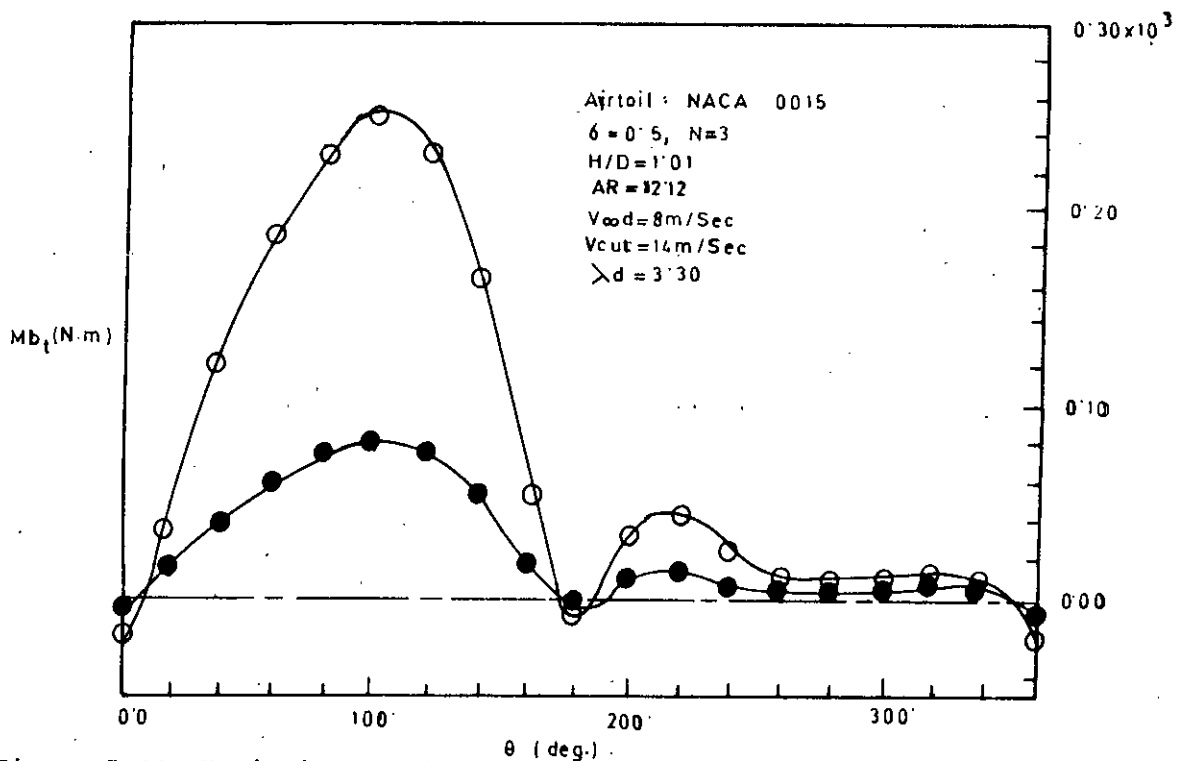


Figure 5.11: Variations of bending moments due to tangential forces with azimuth angle (calculated by cascade theory).

Symbol	:	●	○
V_{∞} (m/sec)	:	8.0 (design)	14.0 (cutout)

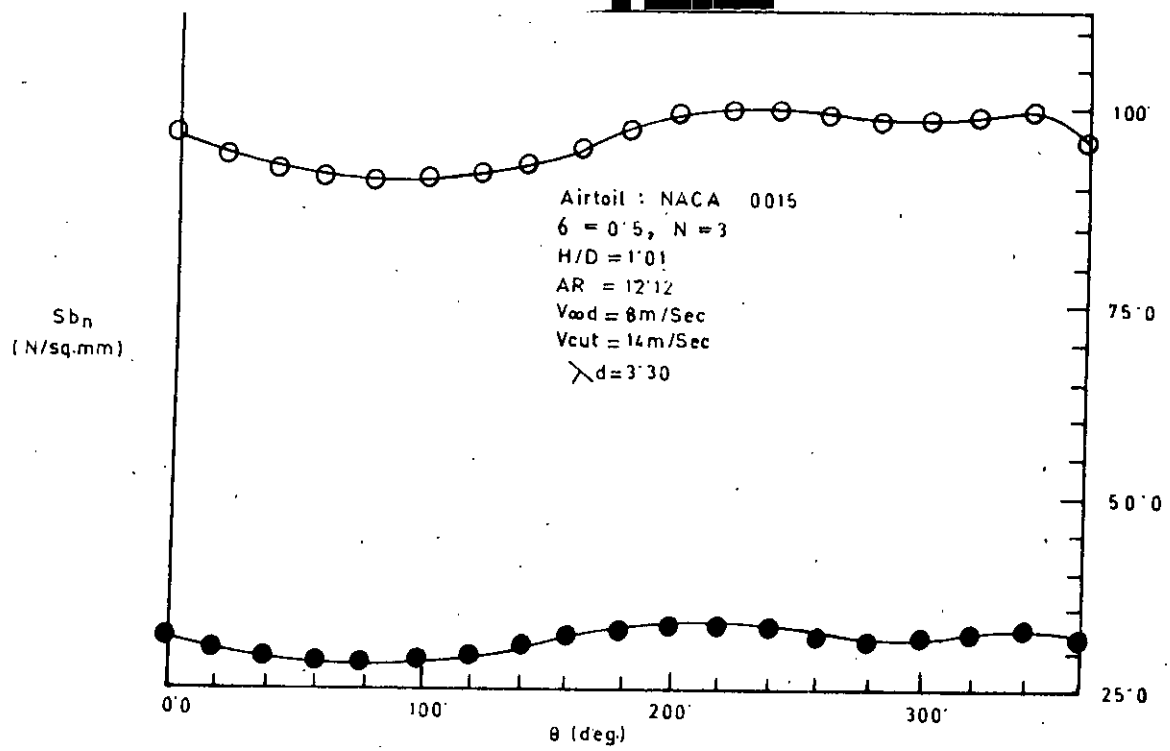


Figure 5.12 : Variations of bending stresses due to net normal forces with azimuth angle (calculated by cascade theory).

Symbol : ● 0
 V_{∞} (m/sec) : 8.0 (design) 14.0 (cutout)

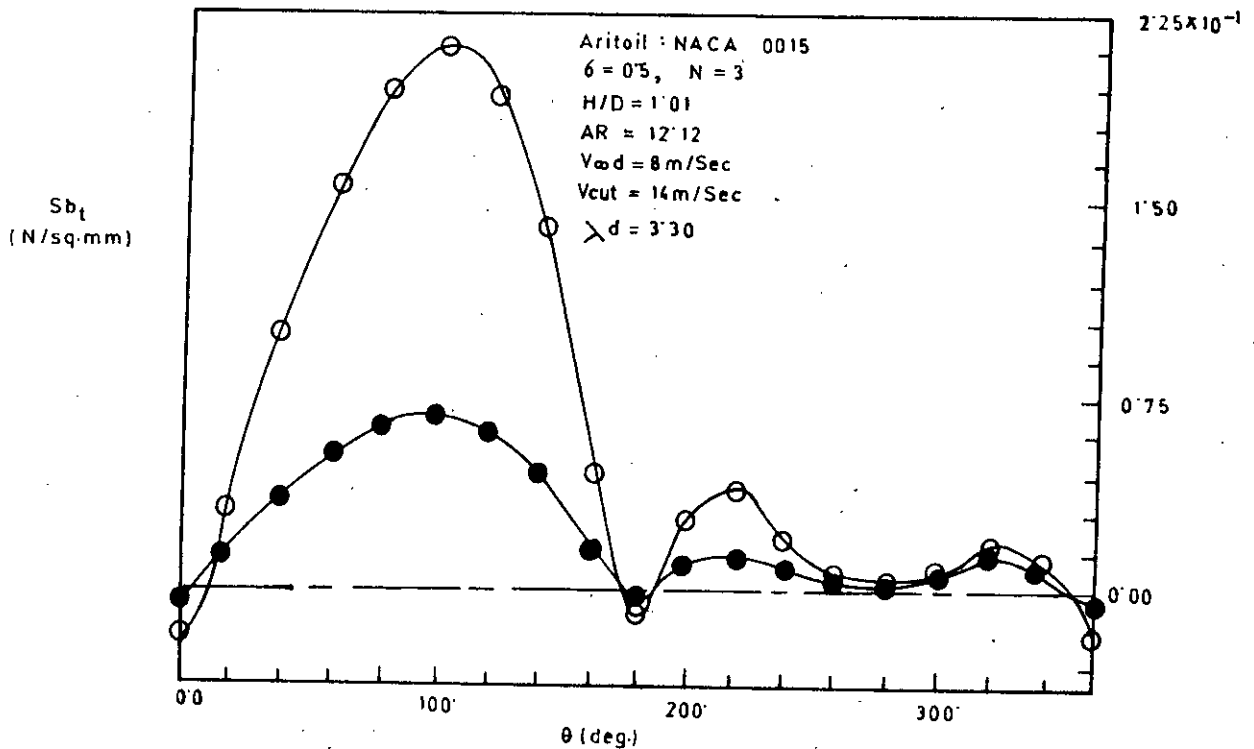


Figure 5.13: Variations of bending stresses due to tangential forces with azimuth angle (calculated by cascade theory).

Symbol : ● 0
 V_{∞} (m/sec) : 8.0 (design) 14.0 (cutout)

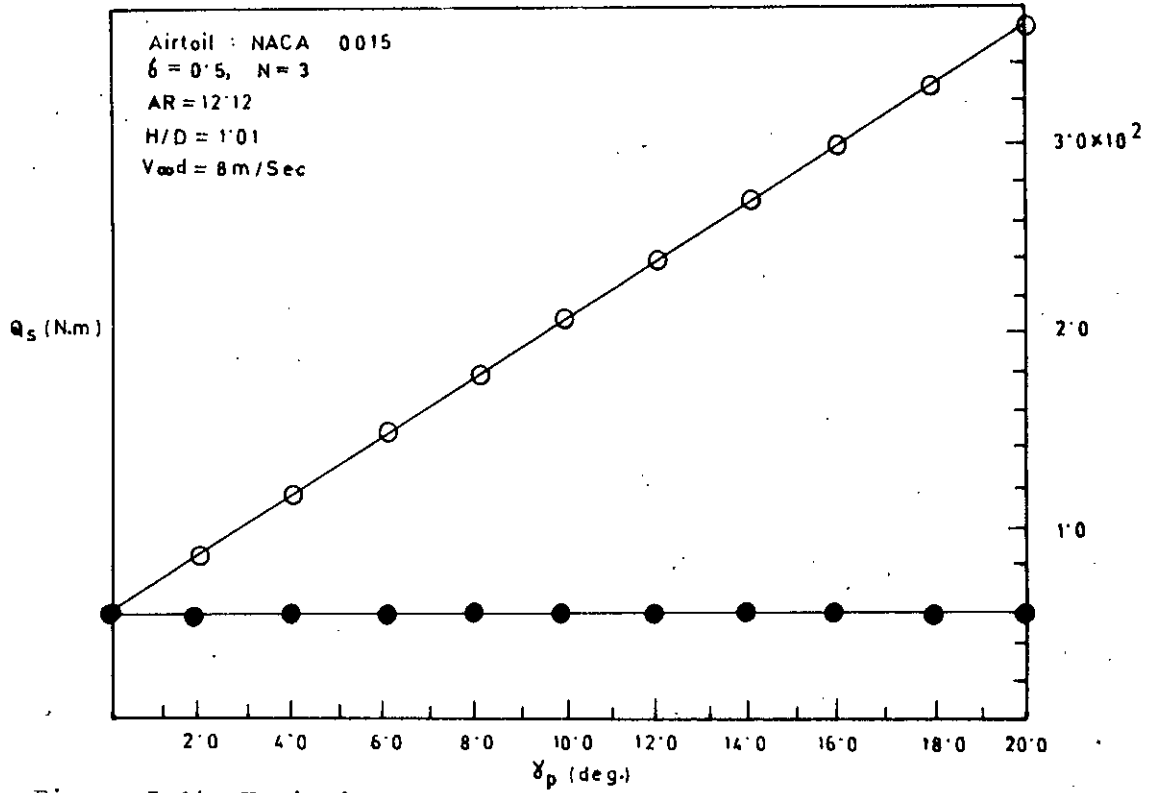


Figure 5.14: Variations of starting torques with blade pitching

Symbol : \circ \bullet
 Parameter : Variable ($\gamma_p \sin \theta$) fixed

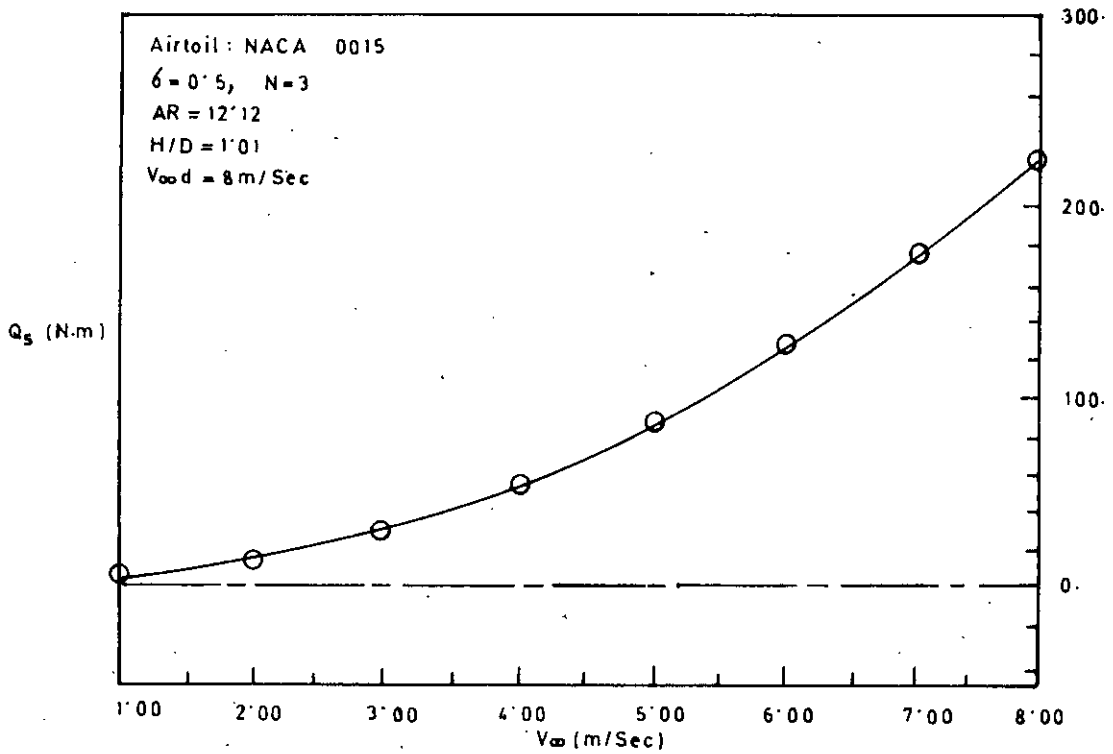


Figure 5.15 : Variation of starting torque with wind speed.

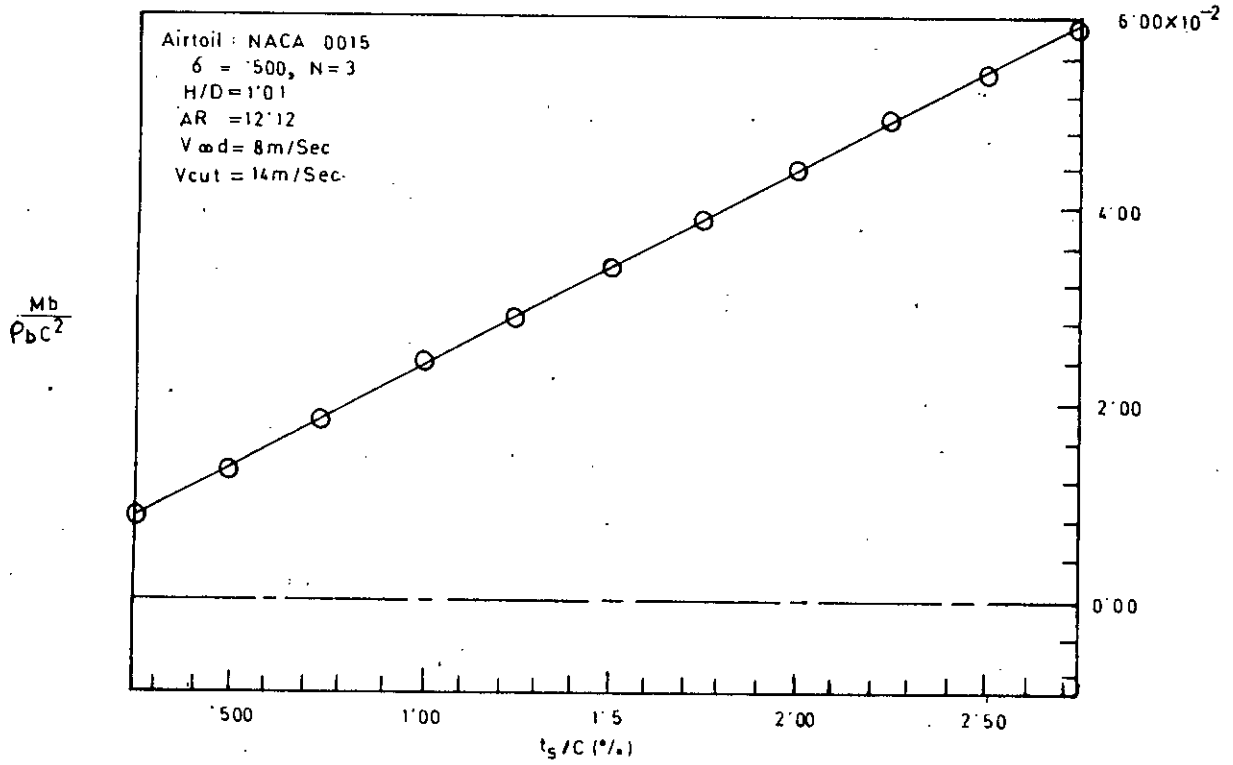


Figure 5.16 : Variation of blade mass with blade skin thickness (calculated by cascade theory) (Ref. [25])

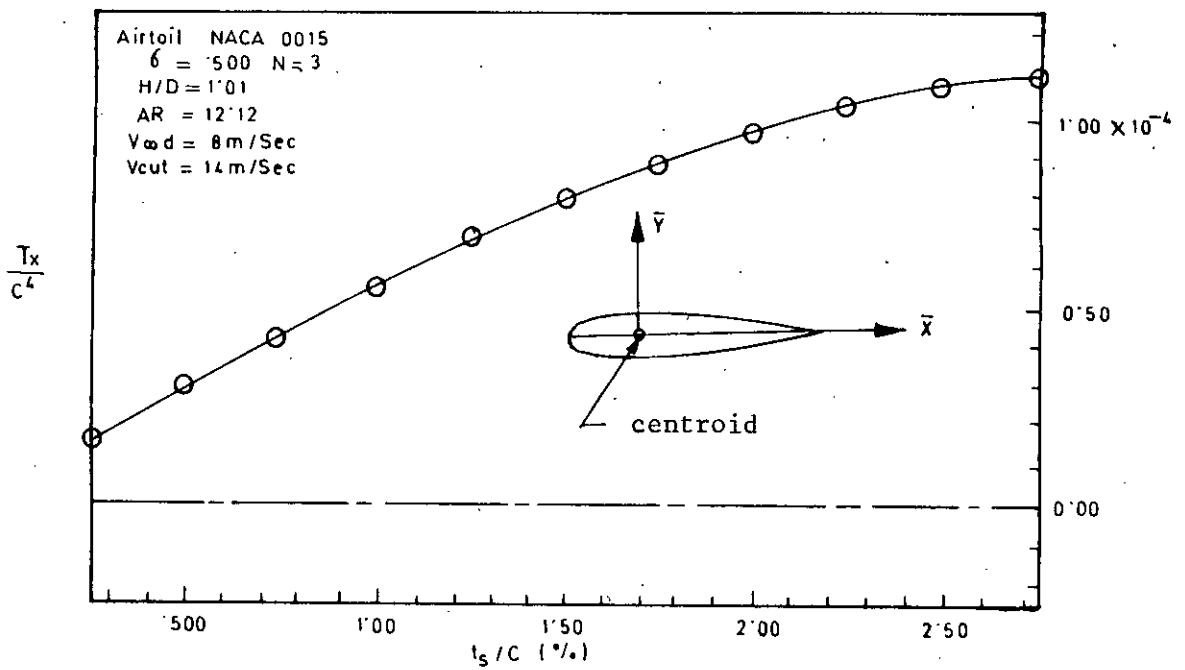


Figure 5.17: Variation of centroidal area moment of inertia about \bar{x} -axis with blade skin thickness (calculated by cascade theory). (Ref. [25])

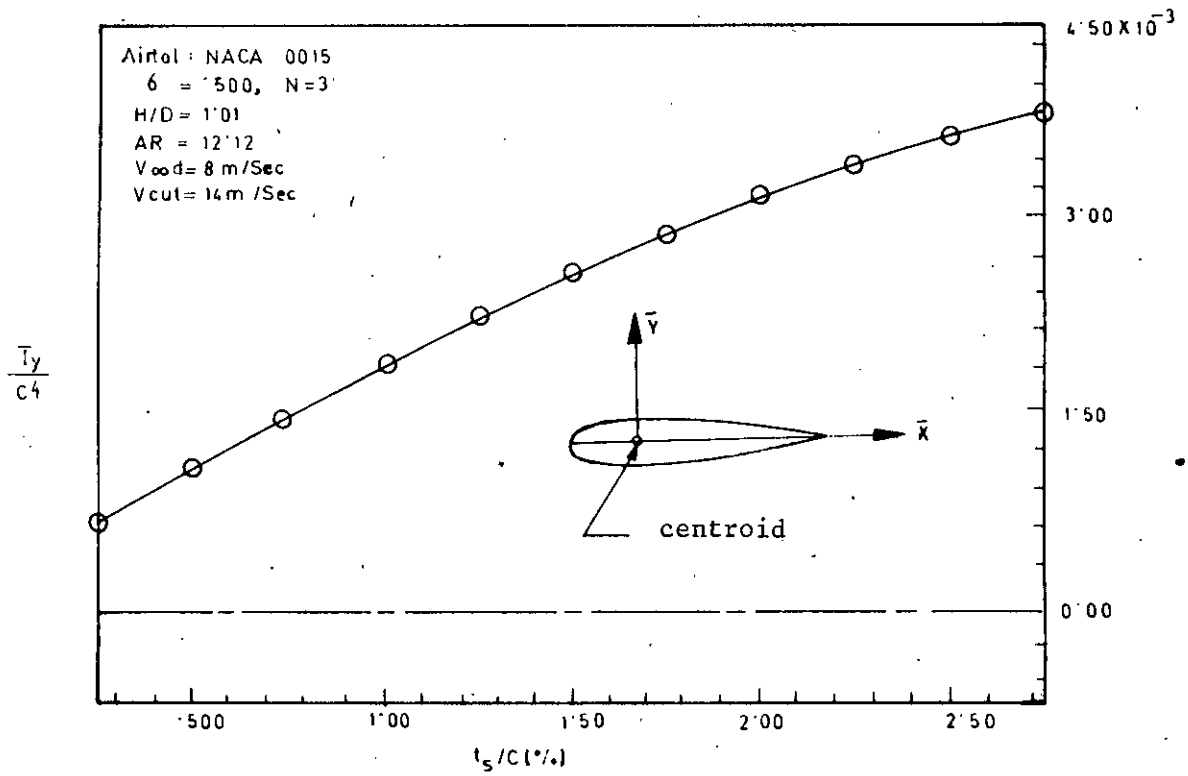


Figure 5.18: Variation of centroidal area moment of inertia about \bar{y} -axis with blade skin thickness (calculated by cascade theory) (Ref. [25])

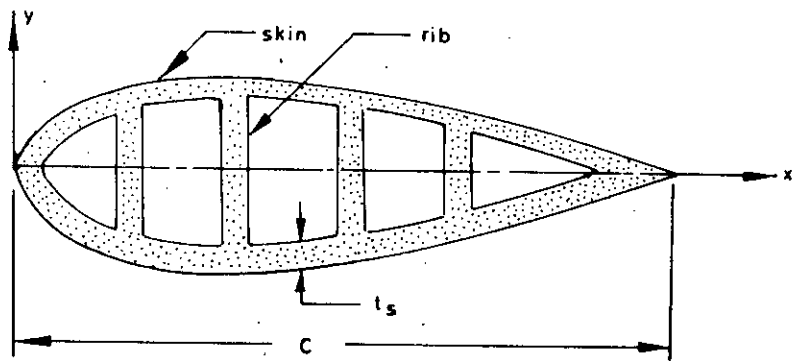


Figure B.1 : Blade airfoil cross-section.

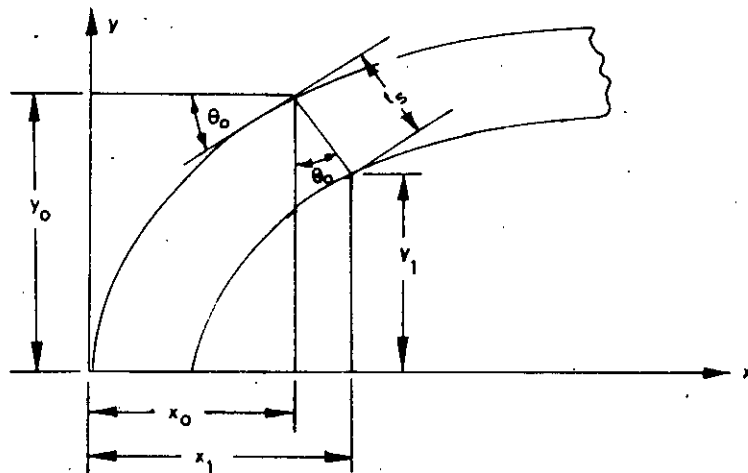


Figure B.2: Geometry of inner and outer faces of blade airfoil.

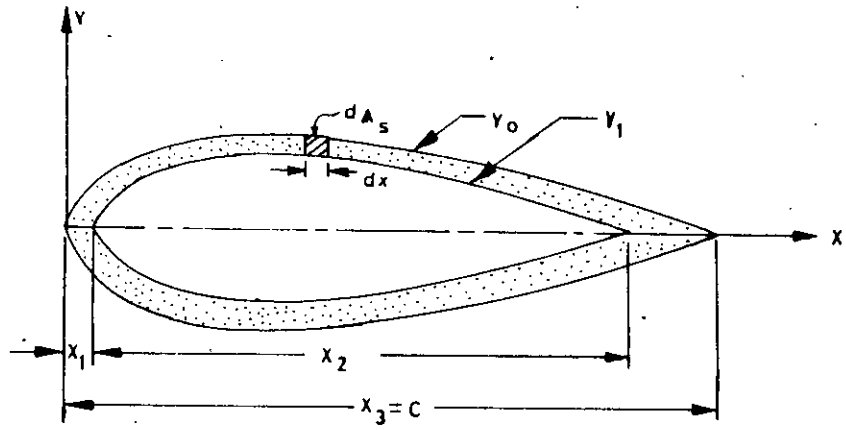


Figure B.3: Geometry on blade airfoil cross-section to find skin area.

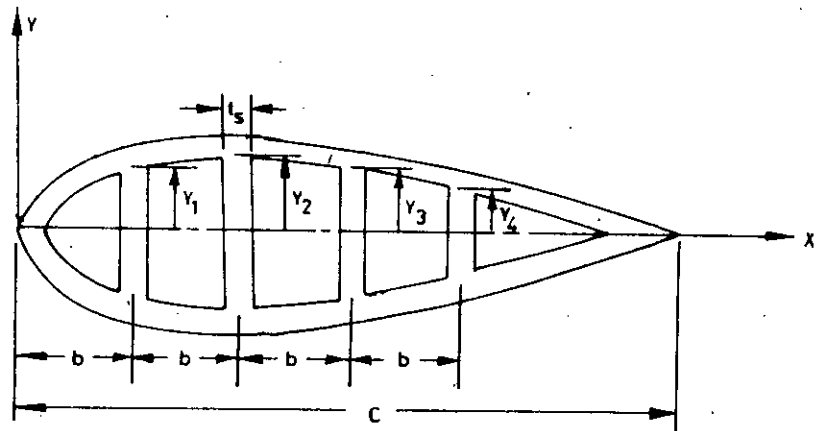


Figure B.4 : Geometry to obtain rib area.

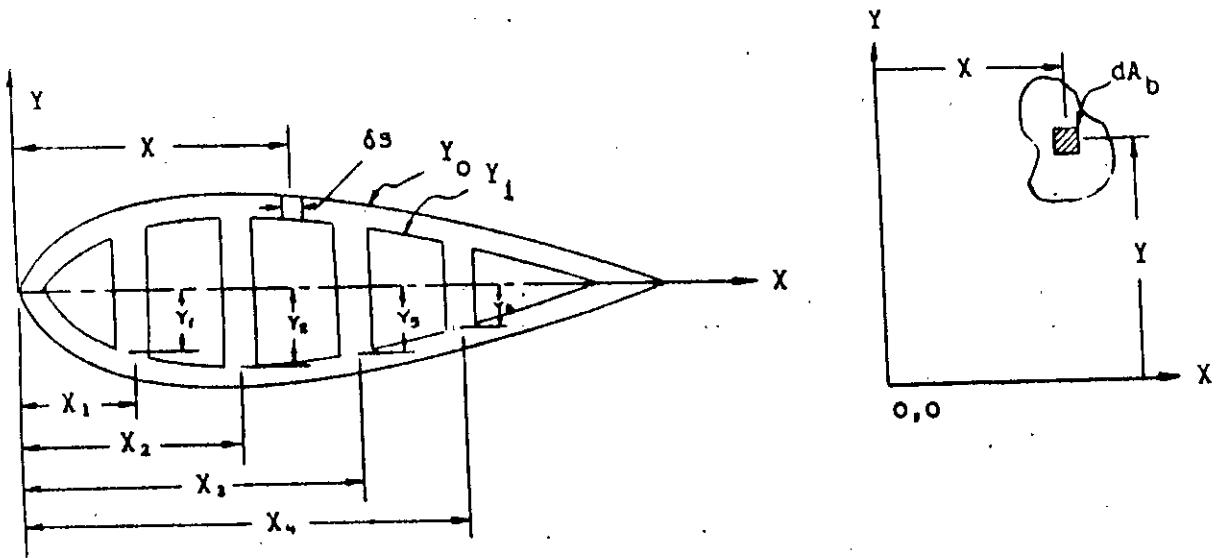
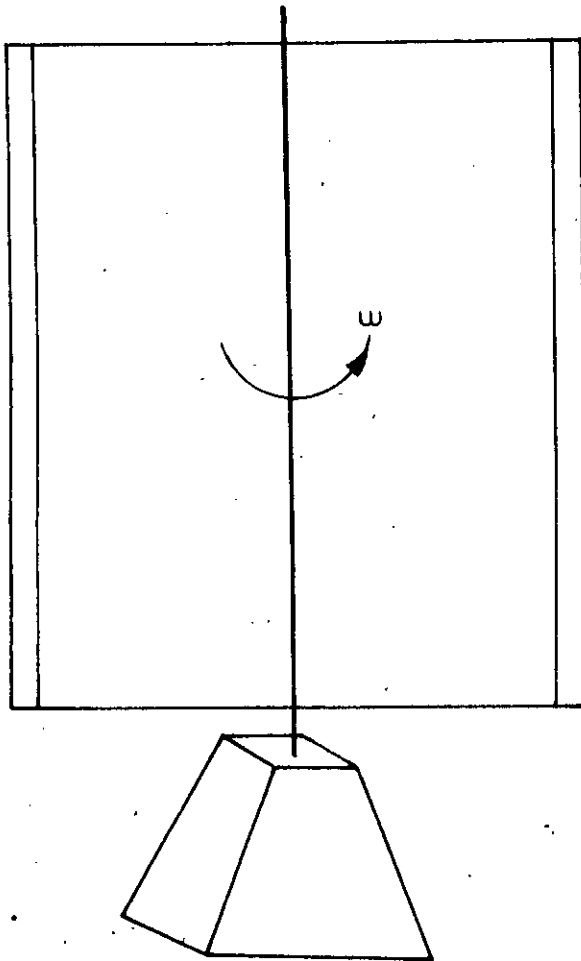
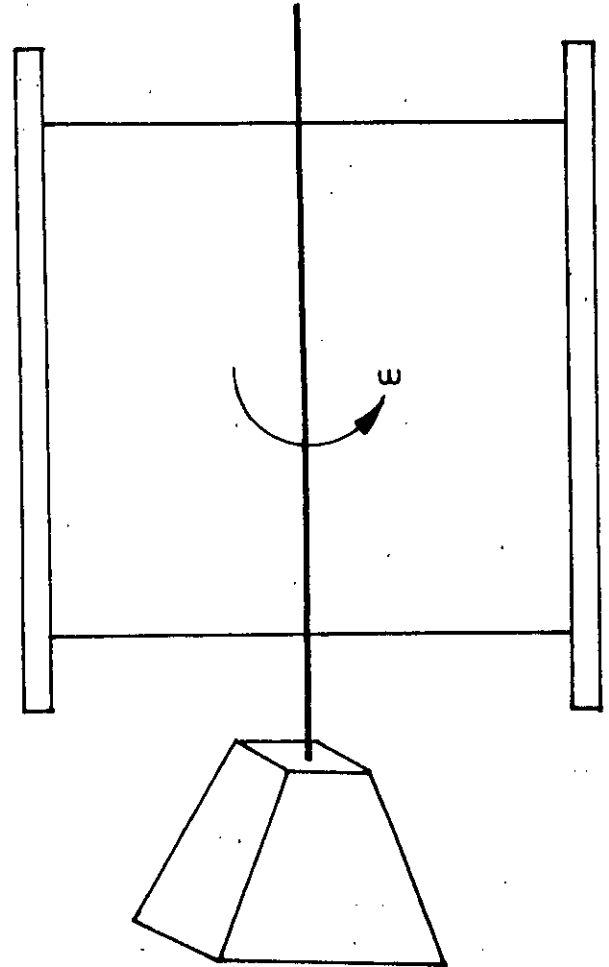


Figure B.5 : Geometry to determine centroid and moment of inertia.



a) Simple support blade



b) Overhanged support blade

Figure C.1: Schematic Diagram of vertical - axis straight-bladed Darrieus turbine.

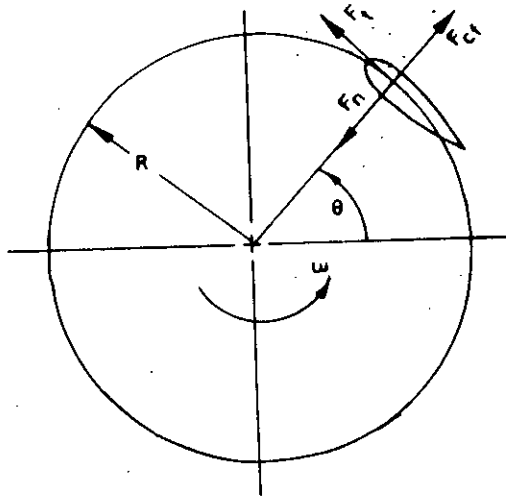


Figure C.2: Horizontal section of a straight-bladed wind turbine showing forces on the turbine blade.

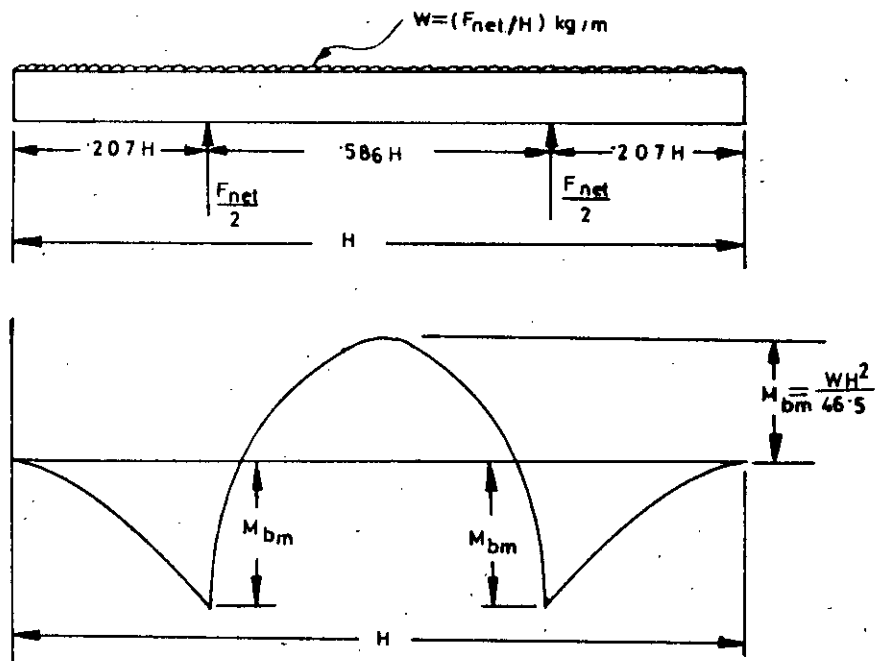


Figure C.3: Bending moment diagram of an overhanged supported beam.

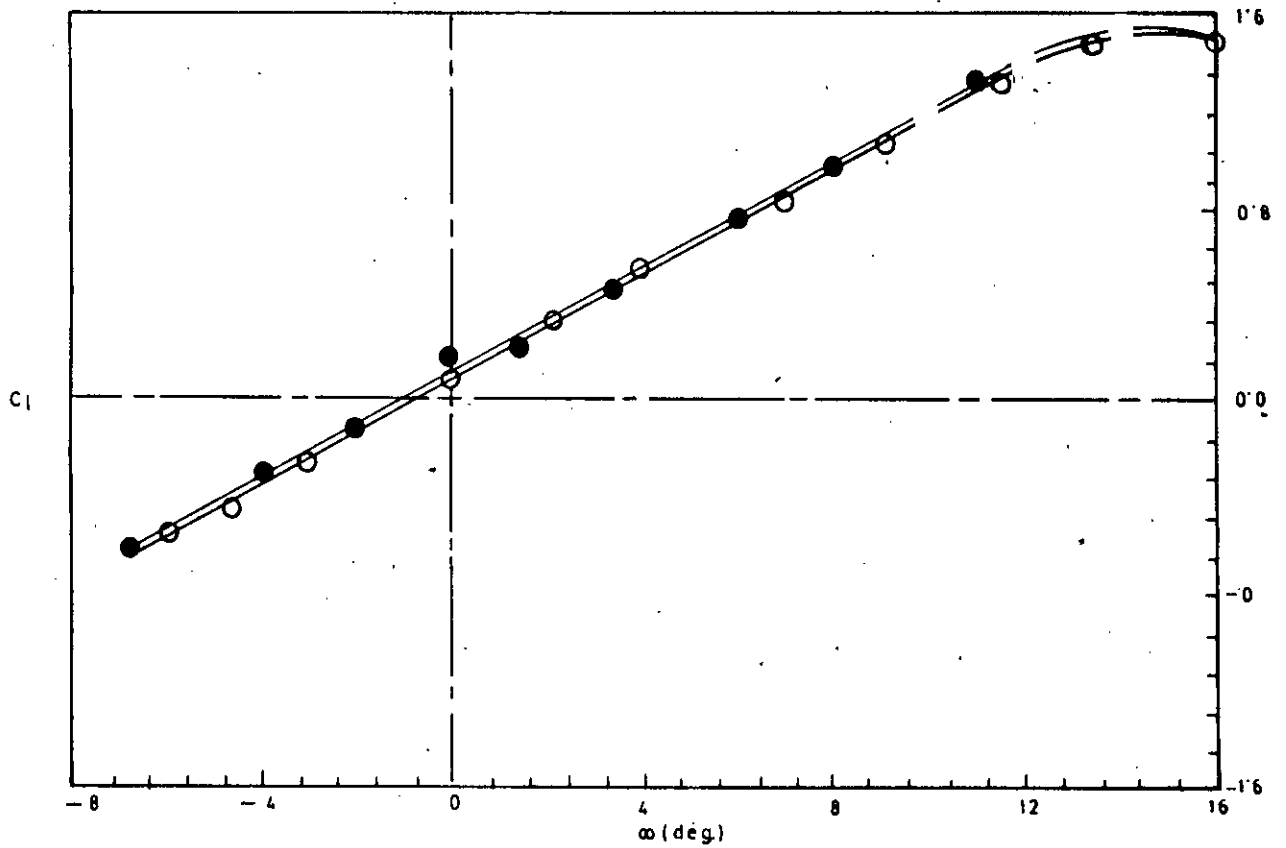


Figure D.1: Variation of lift coefficient with angle of attack at a fixed Reynolds number of 3000000 for the airfoil NACA 1412.

Symbol : \circ (obtained from NACA 0012 after modification)
 ● (experimental values of NACA 1412)

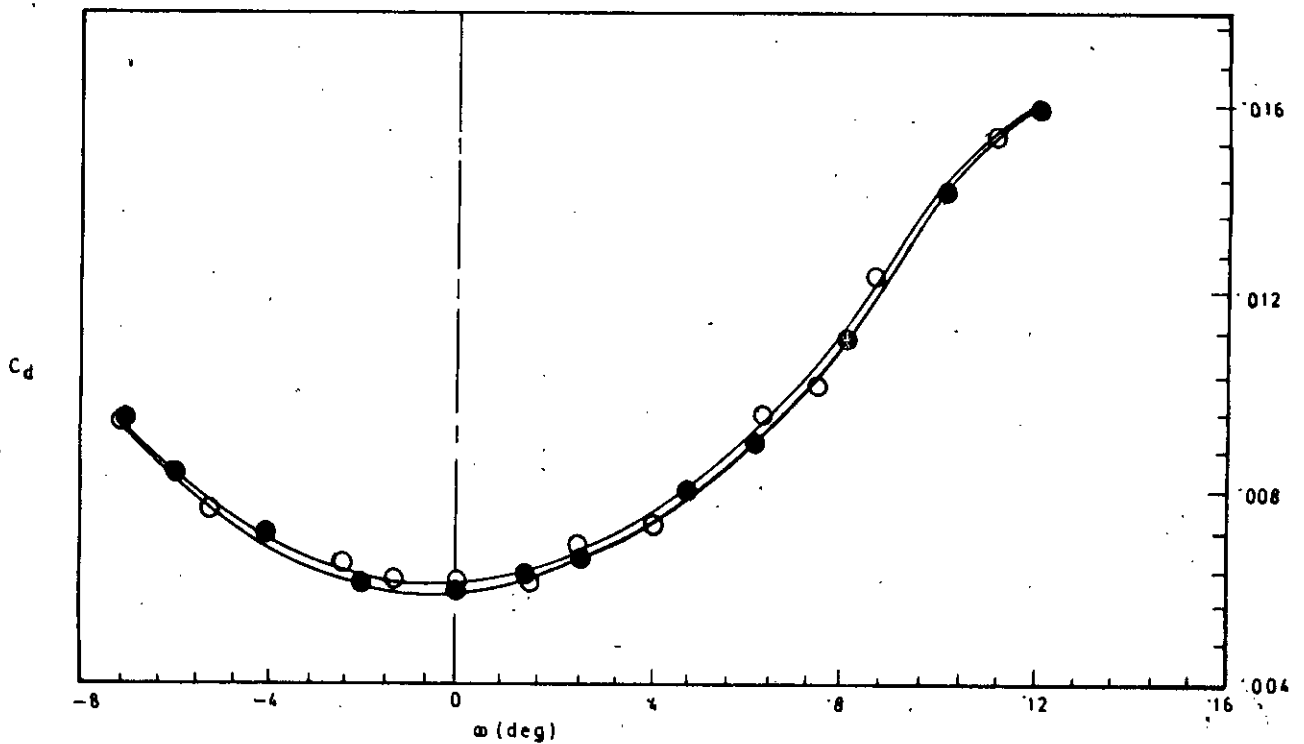


Figure D.2: Variation of drag coefficient with angle of attack at a fixed Reynolds number of 3000000 for the airfoil NACA 1412.

Symbol : \circ (obtained from NACA 0012 after modification)
 ● (experimental values of NACA 1412)

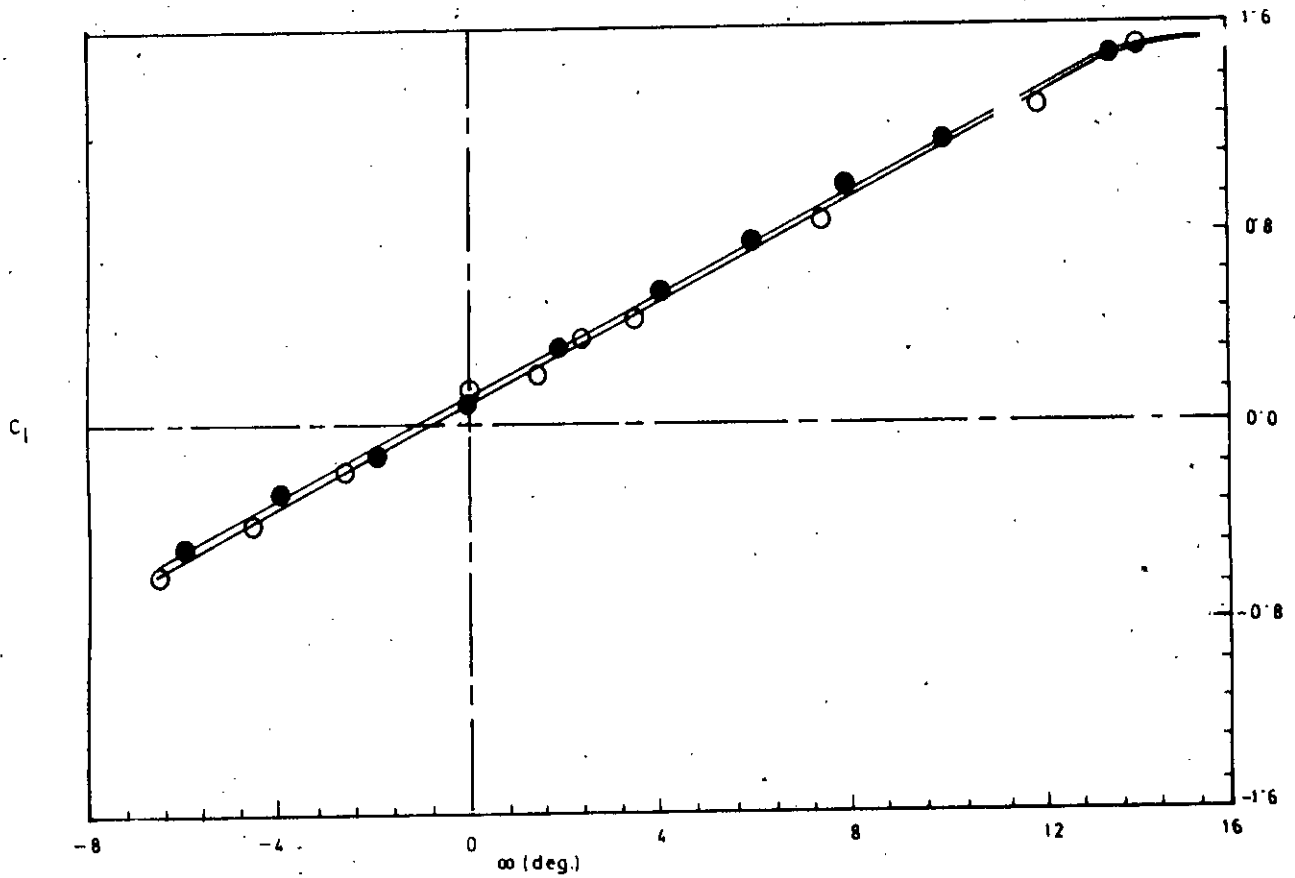


Figure D.3: Variation of lift coefficient with angle of attack at a fixed Reynolds number of 3000000 for the airfoil NACA 1415.

Symbol : ○ (obtained from NACA 0015 after modification)
 ● (experimental values of NACA 1415)

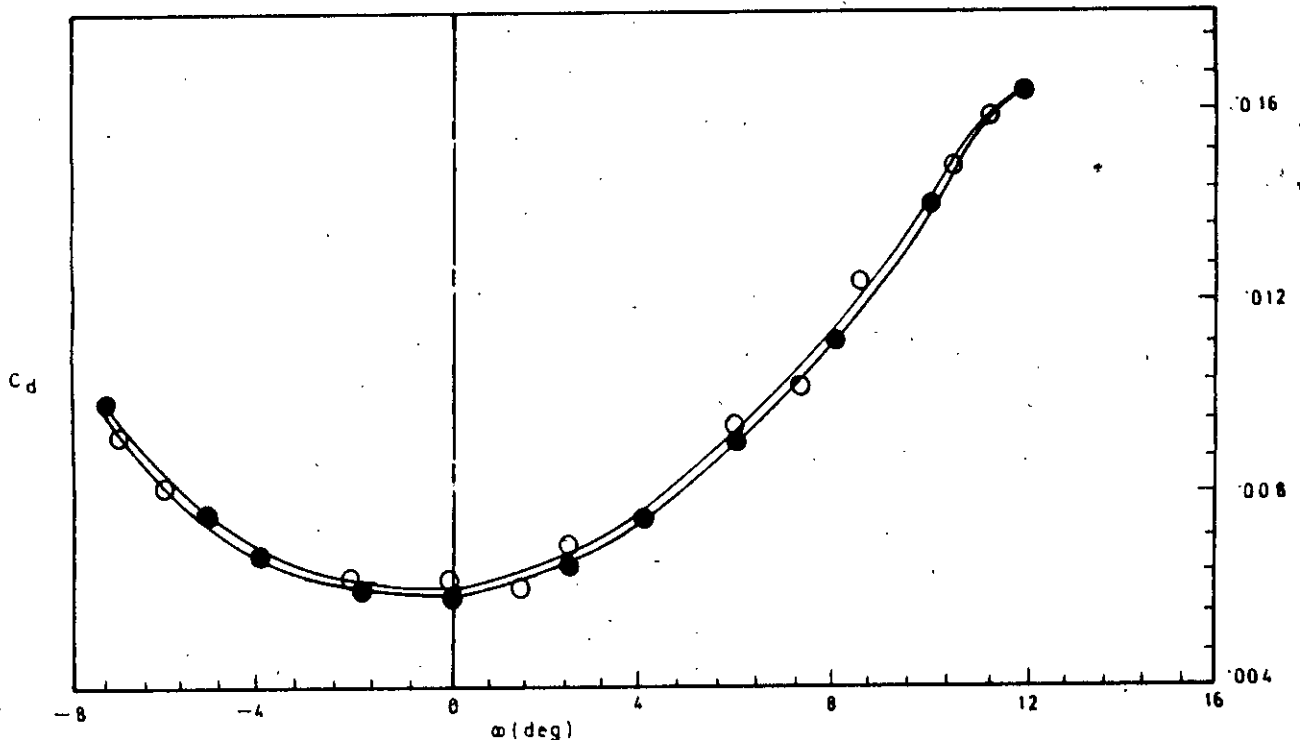


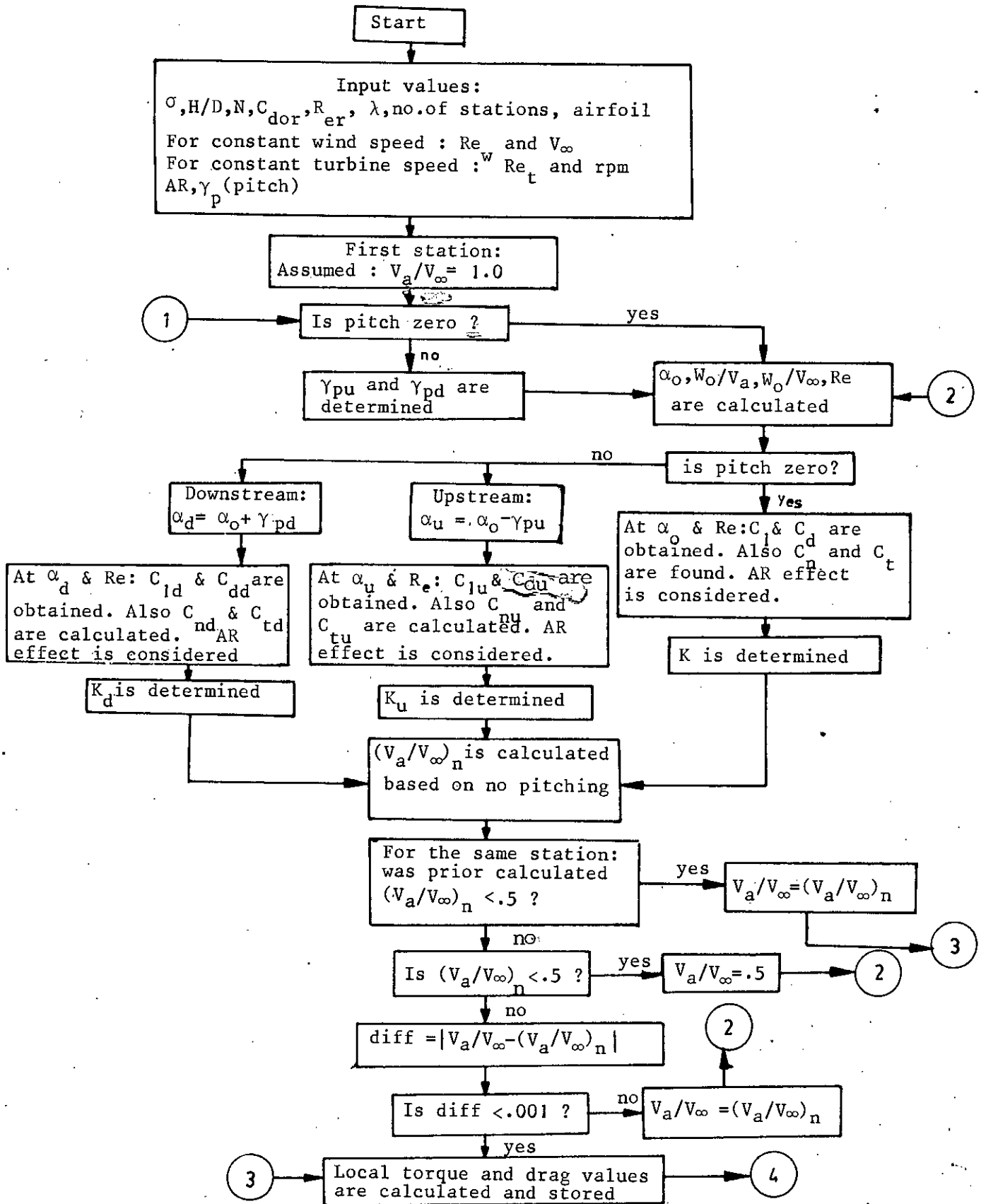
Figure D.4 : Variation of drag coefficient with angle of attack at a fixed Reynolds number of 3000000 for the airfoil NACA 1415.

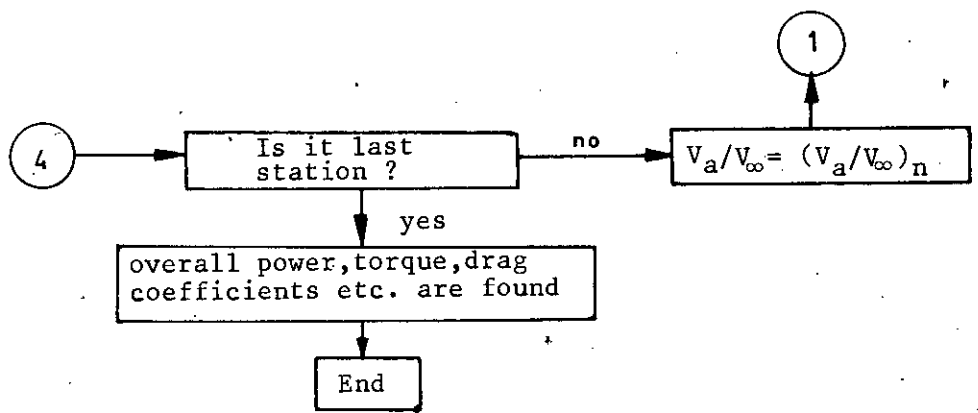
Symbol : ○ (obtained from NACA 0015 after modification)
 ● (experimental values of NACA 1415)

APPENDICES

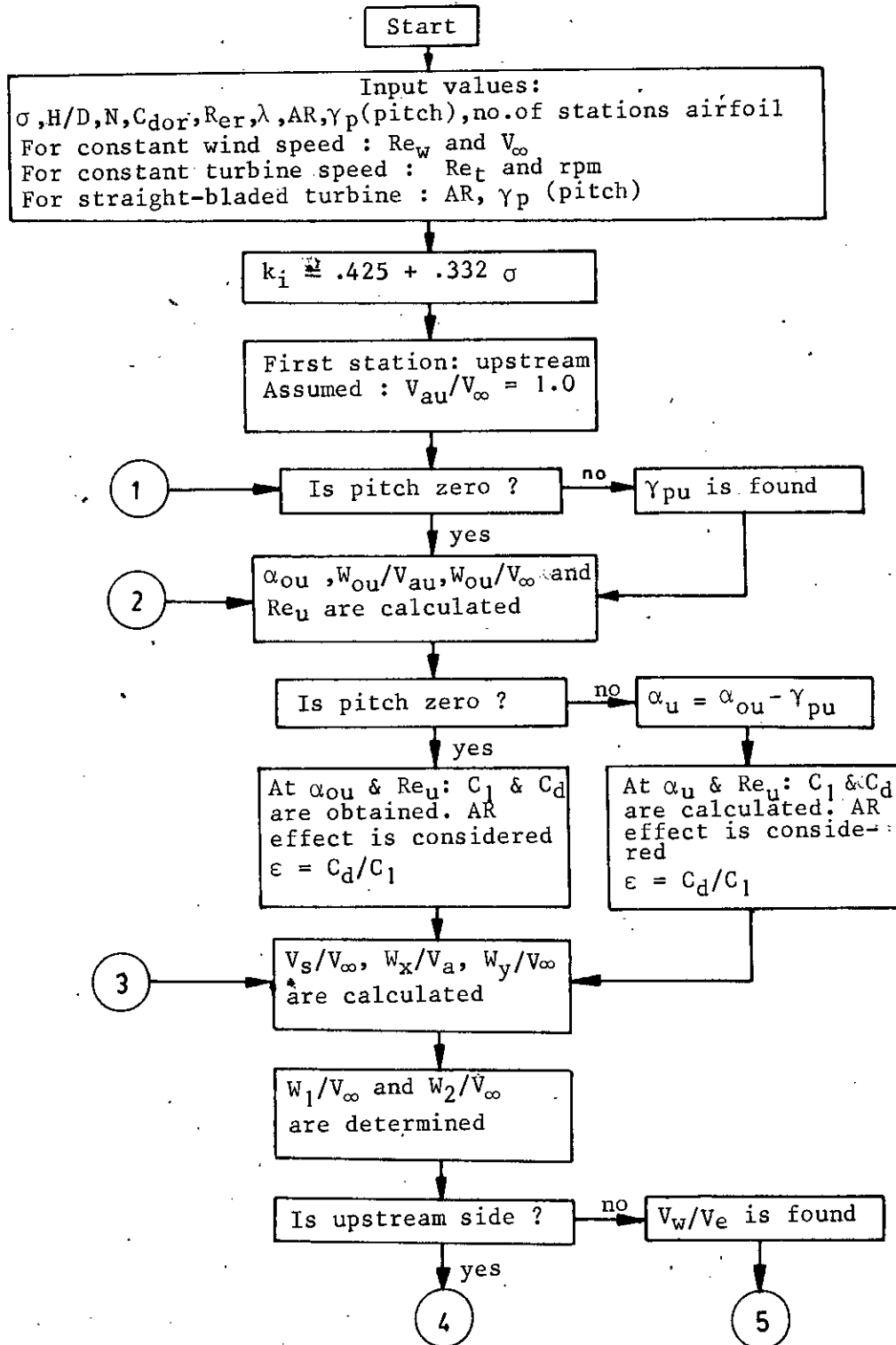
Appendix-A: Flow Diagram of Computational Methods

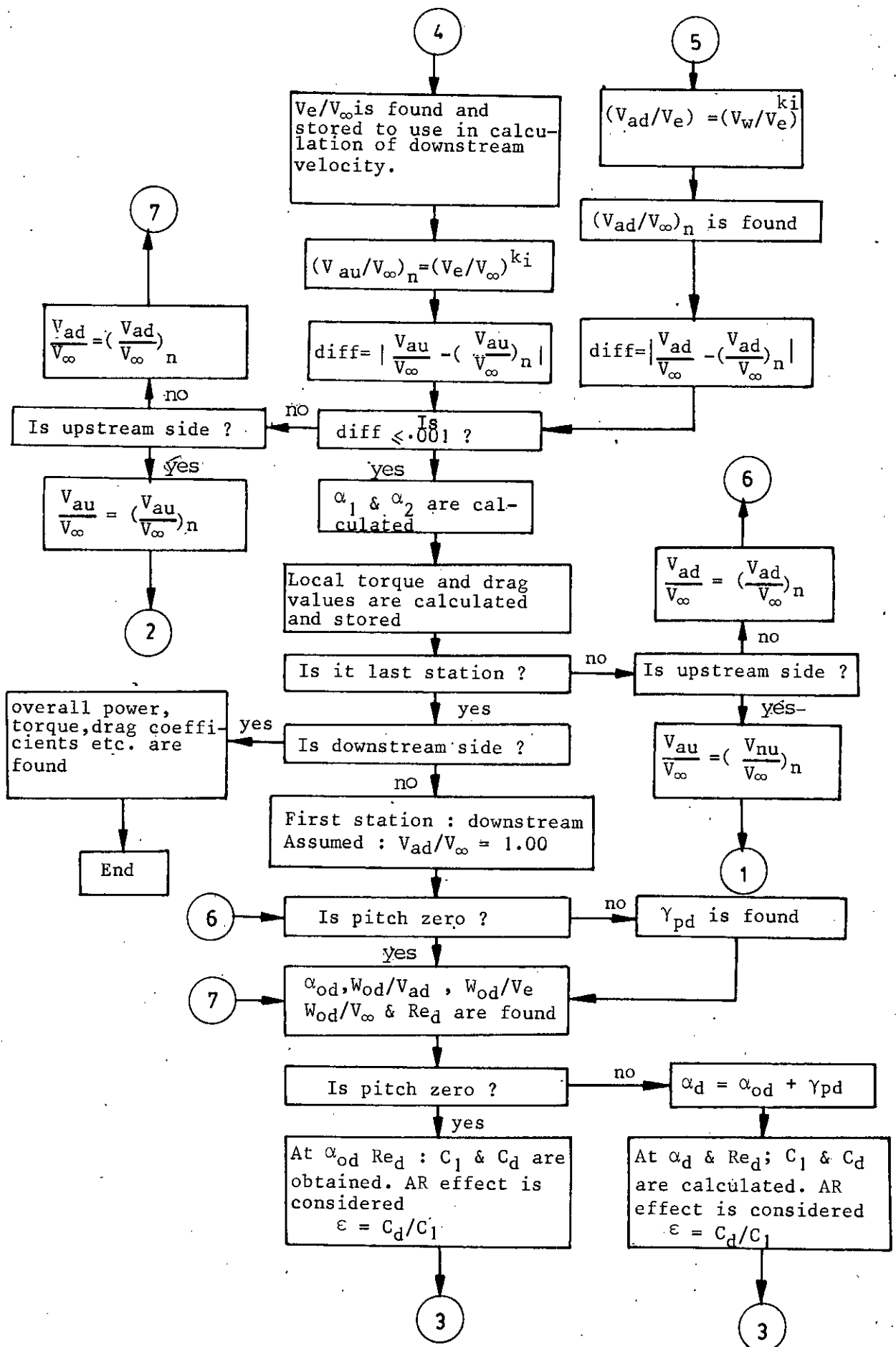
Flow Diagram of Computational Method by Multiple Streamtube Theory



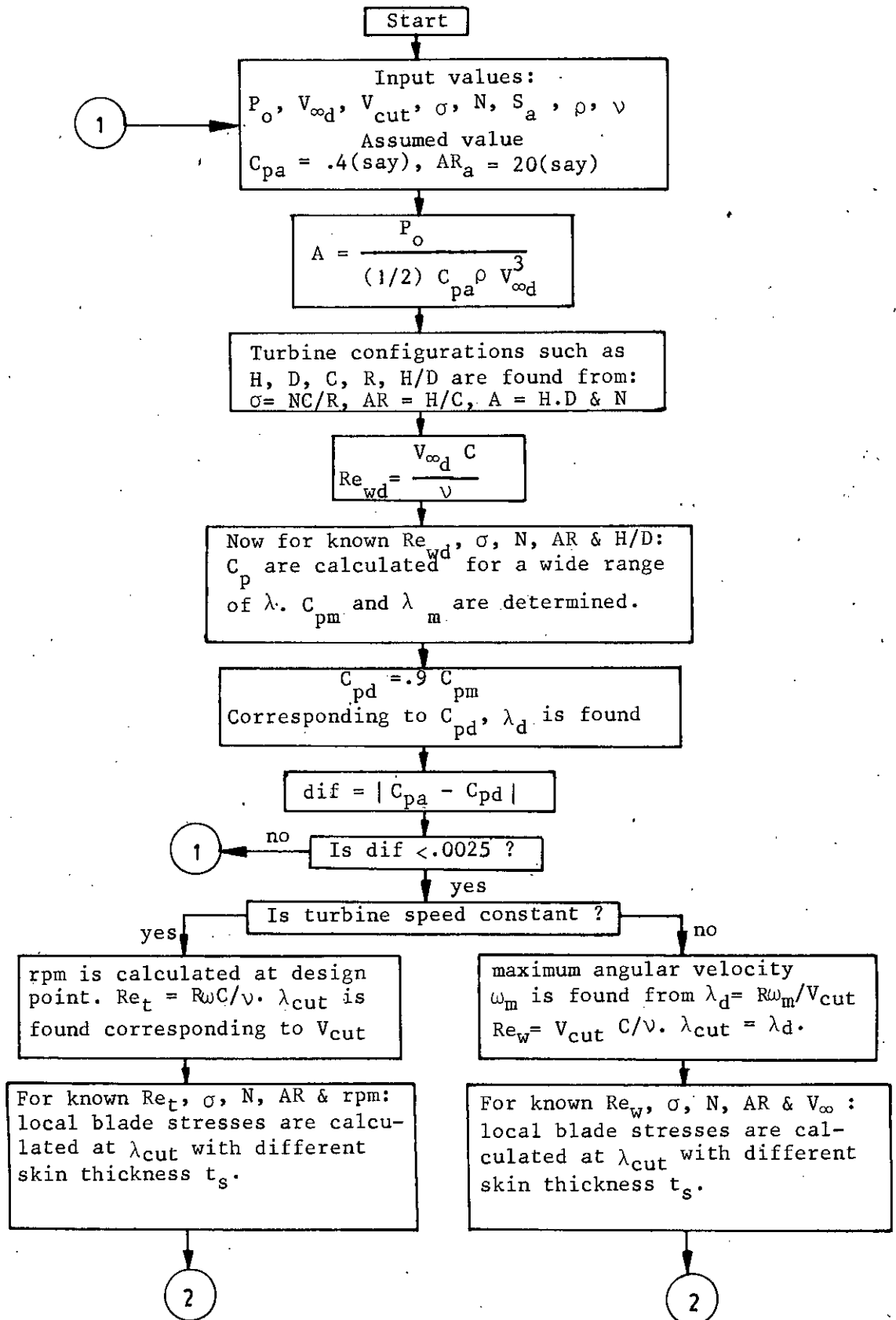


Flow Diagram of Computational Method by Cascade Theory



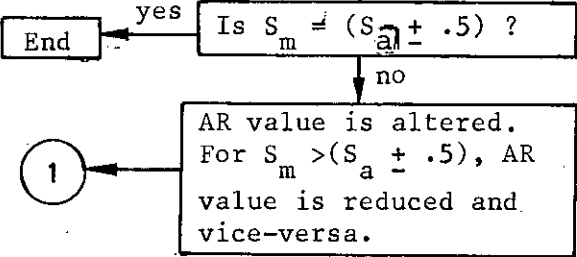


Flow Diagram of Design Procedure of Straight-Bladed Turbines



2

From stress vs. azimuth distribution corresponding to value of λ_{cut} ; maximum stress S_m is found. This value is obtained at every skin thickness t_s (from .50% to 2.5% t_s/C , with step of .25%). The lowest value of S_m in (S_m vs. t_s) distribution is the required blade stress and the corresponding value of t_s is the best thickness.



APPENDIX - B : DERIVATION OF MOMENT OF INERTIA OF BLADE
AIRFOIL SECTION

Figure B.1 represents the blade airfoil cross-section which is used in the present design analysis.

The thickness distribution for NACA four-digit sections is given by the following equation (B.1),

$$\pm y = \frac{t_c}{.2} (.2969 x^{\frac{1}{2}} - .1260 x - .3516 x^2 + .2843 x^3 - .1015 x^4) \quad (B.1)$$

where x, y are in percent of chord. t_c is in fraction of chord. So for blade airfoil NACA 0012, $t_c = .12$ and for blade airfoil NACA 0015, $t_c = .15$.

Equation of Inner Face of Blade Airfoil Skin

Differentiating equation (B.1) and subscripting x and y by o to indicate the outer faces of blade skin, one obtains,

$$\frac{dy_o}{dx_o} = \frac{t_c}{.2} (.14845/x_o^{\frac{1}{2}} - .1260 - .7032 x_o + .8529 x_o^2 - .4060 x_o^3) \quad (B.2)$$

Referring to the figure B.2, the co-ordinates (x'_i, y'_i) on the inner face of the blade skin are,

$$x_i = x_o + t_s \sin \theta_o, \quad y_i = y_o - t_s \cos \theta_o \quad (B.3)$$

where t_s is the skin thickness of the blade airfoil. θ_o may be expressed as,

$$\theta_o = \tan^{-1} (dy_o/dx_o) \quad (B.4)$$

Subscripts o and i are respectively used to distinguish the co-ordinates between the outer and the inner faces.

x_i, y_i are percent of chord. Now the new co-ordinates

(X_i, Y_i) are chosen in such a way that $X_i = x_i C$ and $Y_i = y_i C$.

In this analysis, the equation of the inner face of the blade skin is obtained in polynomial form from the sets of co-ordinates

(X_i, Y_i) by the method of curve fit which is given by,

$$Y_i = b_o + b_1 X_i + b_2 X_i^2 + b_3 X_i^3 + b_4 X_i^4 \quad (B.5)$$

where b_o, b_1, b_2, b_3 and b_4 are the constants.

Area of Blade Skin

The elemental blade skin area,

$$dA_s = 2 (Y_o - Y_i) dx \quad (B.6)$$

which may be written as,

$$A_s = 2 \int Y_o dx - 2 \int Y_i dx = 2 (A_o - A_i) \quad (B.7)$$

$$\text{where, } A_o = \int Y_o dx = C^2 \int y_o dx \quad (B.8)$$

Now subscripting x, y of the equation (B.1) by o to indicate the outer face of blade skin and substituting in the equation

(B.8), one may find,

$$A_o = 5C^2 t_c \int_0^1 (.2969 x_o^{1/2} - .1260 x_o - .3516 x_o^2 + .2843 x_o^3 - .1015 x_o^4) dx_o$$

(B.9)

which may be reduced to,

$$A_o = .34255 t_c C^2 \quad (B.10)$$

A_i may be expressed as,

$$A_i = \int Y_i dx \quad (B.11)$$

Now introducing the value of Y_i from the equation (B.5) and integrating between the limits X_1 and X_2 (figure B.3), one obtains,

$$A_i = b_o (X_2 - X_1) + \frac{b_1}{2} (X_2^2 - X_1^2) + \frac{b_2}{3} (X_2^3 - X_1^3) + \frac{b_3}{4} (X_2^4 - X_1^4) + \frac{b_4}{5} (X_2^5 - X_1^5)$$

(B.12)

Inserting the values of A_o (B.10) and A_i (B.12) in the equation (B.7), the blade skin area can be determined.

Area of Blade Rib

The ribs are assumed to be equally interspaced and the spacing b is considered to be $C/6$ (figure B.4).

$$\text{Area of rib, } A_r = 2 t_s (Y_1 + Y_2 + Y_3 + Y_4) \quad (B.13)$$

The total blade sectional area A_b is,

$$A_b = (A_s + A_r) \quad (B.14)$$

Mass of the blade per unit length,

$$m_b = \rho_b A_b \quad (B.15)$$

where ρ_b is the density of the blade material.

Centroid of Blade Cross-Section

For the electric body the neutral axis passes through the centroid of the blade cross-section.

The centroids are defined by,

$$\bar{X} = \frac{\int X dA_b}{A_b} \quad \text{and} \quad \bar{Y} = \frac{\int Y dA_b}{A_b} \quad (\text{B.16})$$

Numerically one may obtain,

$$\int X dA_b = 2 \delta_s \sum X (Y_o - Y_i) + 2 t_s (X_1 Y_1 + X_2 Y_2 + X_3 Y_3 + X_4 Y_4) \quad (\text{B.17})$$

where δ_s is the thickness of each strip considered in the numerical computation. For symmetric blade \bar{Y} is zero and \bar{X} is one the chord.

Area Moment of Inertia

Area moment of inertia about X-axis is defined as,

$$I_X = \int Y^2 dA_b \quad (\text{B.18})$$

while area moment of inertia about Y-axis is defined as,

$$I_Y = \int X^2 dA_b \quad (\text{B.19})$$

Moment of inertia of blade section area is found by numerical integration method. Moment of inertia about X-axis may be obtained from,

$$I_X = (I_{sX} + I_{rX}) \quad (\text{B.20})$$

where I_{sX} and I_{rX} are respectively the moments of inertia of blade skin and ribs about the X-axis. Referring to the figure B.5, I_{sX} and I_{rX} may be obtained as follows,

$$I_{sX} = 2 \Sigma \left[\delta_s \frac{(Y_o - Y_i)^3}{12} + \delta_s (Y_o - Y_i) \frac{(Y_o + Y_i)^2}{4} \right] \quad (B.21)$$

$$I_{rX} = 2 \frac{t_s}{3} (Y_1^3 + Y_2^3 + Y_3^3 + Y_4^3) \quad (B.22)$$

Now putting the values of I_{sX} (B.21) and I_{rX} (B.22) in the equation (B.20), the moment of inertia about X-axis can be determined. The moment of inertia about Y-axis can be obtained as,

$$I_Y = (I_{sY} + I_{rY}) \quad (B.23)$$

where I_{sY} and I_{rY} are the moments of inertia of the blade skin and ribs respectively about the Y-axis, which may be obtained from,

$$I_{sY} = 2 \Sigma \left[(Y_o - Y_i) \delta_s^3 / 12 + \delta_s (Y_o - Y_i) X^2 \right] \quad (B.24)$$

$$I_{rY} = 2 (Y_1 + Y_2 + Y_3 + Y_4) \frac{t_s^3}{12} + 2 t_s (Y_1 X_1^2 + Y_2 X_2^2 + Y_3 X_3^2 + Y_4 X_4^2) \quad (B.25)$$

Now the centroidal moments of inertia about X-axis and Y-axis respectively obtained from,

$$\bar{I}_X = I_X \text{ and } \bar{I}_Y = I_Y - A_b \bar{X}^2 \quad (B.26)$$

APPENDIX - C : DERIVATION OF BENDING MOMENT AND BENDING STRESS

Derivation techniques of bending moment and bending stress are given in this appendix. These are done for no blade pitching condition.

Figure C.2 shows the forces developed on the turbine blade. F_n and F_t are respectively the normal and the tangential forces (aero-dynamic). F_n and F_t can be obtained from the equations (3.14) and (3.15) respectively. F_{cf} is the centrifugal force. The centrifugal force may be expressed as,

$$F_{cf} = m_b \omega^2 R \quad (C.1)$$

where m_b is the blade mass per unit blade length. ω is the angular velocity and R is the radius of the turbine. The directions of the forces as shown in the figure C.2, are considered to be positive in this analysis. The net normal force on the turbine blade (in the radially outward direction) can be obtained as,

$$F_{net} = F_{cf} - F_n \quad (C.2)$$

In the present analysis, the blades are considered to be supported like that of a overhanged support beam.

In the figure C.3, the bending moment diagram of a overhanged supported beam is shown. The forces on the turbine blade are distributed all over the blade length which is also seen from the figure C.3. The expression of the maximum bending moment can be obtained as,

$$M_{bm} = \frac{w \cdot H^2}{46.5} \quad (C.3)$$

where w is the load per unit length of the blade. Introducing the value of $w = F_{net}/H$ in the equation (C.3), one obtains,

$$M_{bm} = \frac{F_{net} \cdot H}{46.5} \quad (C.4)$$

where H is the height of the turbine and hence the length of the turbine blade. The maximum bending stress can be found as,

$$S_{bm} = \frac{M_{bm} (t_c \cdot C/2)}{I_X} \quad (C.5)$$

where t_c is the maximum blade thickness as a fraction of chord and C is the chord of the blade airfoil. I_X is the area moment of inertia about the chord of the blade airfoil. From the equations (C.4) and (C.5), the expression of the maximum bending stress can be written as,

$$S_{bm} = \frac{F_{net} \cdot H \cdot C \cdot t_c}{93 \cdot I_X} \quad (C.6)$$

The effect of tangential force on the blade stress is not encountered in this analysis, because this force is negligible in comparison to the net normal force.

APPENDIX - D : AIRFOIL CHARACTERISTICS

The airfoil characteristics for the cambered blade profile are not available for the wider range of Reynolds number and the angles of attack. For the performance analysis of a Darrieus turbine with blades of cambered cross-section the airfoil characteristics for wider range of Reynolds number and angles of attack are necessary. Hence to fulfill this requirement a technique is used to modify the lift-drag characteristics of a symmetric airfoil to be applicable for the cambered airfoil. The modified lift-drag characteristics are compared with the existing experimental values of lift-drag for the cambered airfoil which are available at few Reynolds number only. The comparative figures shows excellent correlation. So this idea is extended to find the lift-drag values for the cambered airfoil at wider range of Reynolds number and angles of attack. It is expected that this idea, to consider lift-drag characteristics for a cambered airfoil, would be very reasonable and make error within 1-2%. Ofcourse for higher camberness effect the idea would give higher error.

To modify the lift-drag characteristics the thin airfoil theory is applied. The procedure of choosing the lift-drag characteristics is given below in short.

$$\alpha_{\text{mod}} = \alpha + \alpha_{\text{cor}} \quad (\text{D.1})$$

where α is the calculated angle of attack which may be obtained from equation (3.13),

α_{cor} is the corrected angle of attack due to camberness effect and α_{mod} is the modified angle of attack value.

Lift-drag characteristics of a cambered airfoil for angle of attack α is taken corresponding to α_{mod} from the lift-drag characteristics of a symmetric-blade profile. α_{cor} in equation (D.1) may be obtained from,

$$\alpha_{cor} = \tan^{-1} \left(\frac{f}{C} \right) \quad (D.2)$$

where C is the blade chord and f is the maximum camber of the blade.

APPENDIX - E : EFFECT OF ASPECT RATIO

For the performance prediction of a straight-bladed Darrieus wind turbine, the effect of finite aspect ratio on the airfoil characteristics are necessary. Since the finite wing and the finite blade of a straight-bladed wind turbine are of similar pattern, so wing theory may be applied for the finite aspect ratio effects on the airfoil characteristics before using them for the performance prediction of a straight-bladed wind turbine.

For the wing of finite span, there occurs always downwash and power required to induce downwash is expressed in terms of induced drag. The downwash velocity is created by the presence of tip vortices. The total drag coefficient of a finite wing is given by,

$$C_d = C_{do} + C_{di} \quad (E.1)$$

where C_{do} is the section drag coefficient for infinite aspect ratio while C_{di} is the induced drag coefficient, C_{di} is expressed as,

$$C_{di} = \frac{C_l^2}{2 \pi AR} \quad (E.2)$$

where AR indicates the aspect ratio of the turbine blade.

Introducing the value of C_{di} in the equation (E.1),

$$C_d = C_{do} + \frac{C_l^2}{2 \pi AR} \quad (E.3)$$

The angle of attack corrected for finite aspect ratio effect is obtained as,

$$\alpha = \alpha_o + \alpha_i \quad (E.4)$$

where α_o indicate the angle of attack for infinite wing and α_i is the induced angle. The expression of induced angle α_i is,

$$\alpha_i = \frac{C_l}{2 \pi AR} \quad (E.5)$$

substituting equation (E.5) in the equation (E.4)

$$\alpha = \alpha_o + \frac{C_l}{2 \pi AR} \quad (E.6)$$

The above two equations (E.3) and (E.6) are developed on the assumptions of uniform distribution of downwash and they are explicitly valid only for wings possessing an elliptic lift distribution. However other cases are dealt with considering appropriate correction factors. Letting T is the correction factor for the induced angle and δ is the correction factor for the induced drag, the expressions of C_d and α become,

$$C_d = C_{do} + \frac{C_l^2}{2 \pi AR} (1 + \delta) \quad (E.7)$$

$$\alpha = \alpha_o + \frac{C_l}{2 \pi AR} (1 + T) \quad (E.8)$$

For a rectangular wing there are two limiting cases. When the chord is large compared with the span, aspect ratio AR approaches zero. In this case Betz finds an elliptical distribution of loading. As the aspect ratio increases to infinite the loading approaches rectangular distribution. The values of T and δ are taken from the reference [27] and [34].